

Pleural effusions are abnormal accumulations of fluid within the [pleural space](#). They may result from a variety of pathological processes which overwhelm the pleura's ability to reabsorb fluid.

Terminology

"Pleural effusion" is commonly used as a catch-all term to describe any abnormal accumulation of fluid in the pleural cavity. The lack of specificity is mainly due to the limitations of the imaging modality. Given that most effusions are detected by x-ray, which generally cannot distinguish between fluid types, the fluid in question maybe simple (transudative) fluid, blood, pus, chylous fluid, etc.

If simple fluid, then the term **hydrothorax** may be employed, although this is rarely used (other than in combination terms e.g. [hydropneumothorax](#)).

If additional corroborative evidence is available, certain (mostly non-transudative) effusions are preferentially designated using more specific terminology. This is important because these effusions may be managed distinctly. These are discussed separately:

- [bilothorax](#)
- [chylothorax](#)
- [chlothorax](#)
- [empyema \(pyothorax\)](#)
- [glicinothorax](#)
- [hemothorax](#)
- [infusothorax \(chemothorax\)](#)
- [oleothorax](#)
- [pseudochylothorax](#)
- [urinothorax \(urothorax\)](#)

Epidemiology

As the accumulation of fluid in the pleural space occurs in a broad range of disparate clinical scenarios, no single demographic is affected; rather the epidemiology will match that of the underlying condition. However, it is probably safe to say that as [congestive cardiac failure](#) and malignancy are some of the most common causes, older patients would be over-represented.

Clinical presentation

A small amount of fluid is completely asymptomatic. In fact, depending on the respiratory reserve of the patient, even large amounts of fluid can accumulate within the pleural space before any symptoms are recognized.

Eventually as the volume of fluid increases, with resulting [passive \(relaxation\) atelectasis](#) of the adjacent lung, the patient will experience reduced exercise tolerance and breathlessness.

Pathology

Physiologically, the pleural cavities normally contain approximately 15 mL of serous pleural fluid⁶. Any process which results in more fluid forming than can be absorbed will produce a pleural effusion.

Transudates vs exudates

There are many causes of pleural effusion that are broadly split into transudates and exudates. This categorization relies upon the biochemical analysis of aspirated pleural fluid⁵:

- transudate
 - protein concentration
 - <30 g/L absolute
 - total protein fluid:serum ratio <0.5
 - lactate dehydrogenase (LDH)
 - <20 IU/L
 - LDH fluid:serum ratio <0.6
 - specific gravity <1.016
- exudate
 - protein concentration
 - >30 g/L
 - total protein fluid:serum ratio >0.5
 - lactic acid dehydrogenase (LDH)
 - >20 IU/L
 - LDH fluid:serum ratio >0.6
 - specific gravity >1.016

Transudate

It occurs when there is an increase in hydrostatic pressure or a decrease of capillary oncotic pressure.
Examples:

- cardiac failure
- nephrotic syndrome
- cirrhosis
- cirrhosis: hepatic hydrothorax³
- Dressler syndrome
- trauma
- asbestos exposure
- yellow nail syndrome

- [urinothorax](#)
- [post coronary artery bypass grafting](#): small unilateral left-sided pleural effusion can be common¹¹
- certain medications:
 - dasatinib⁷

Exudate

It occurs due to the increase in permeability of the microcirculation or alteration in the pleural space drainage to lymph nodes. Examples:

- [bronchial carcinoma](#)
- secondary (metastatic) malignancy
- [pulmonary embolism](#) and [infarction](#) - [pleural effusions in pulmonary embolism](#)
- [pneumonia](#)
- [tuberculosis](#)
- [mesothelioma](#)
- [rheumatoid arthritis](#)
- [systemic lupus erythematosus \(SLE\)](#)
- [lymphoma](#)
- [yellow nail syndrome](#)

Differential white cell count

Differential white cell count of the pleural aspirate is also important, resulting in pleural effusions with mainly [granulocytes](#), [eosinophils](#) or [lymphocytes](#)¹⁴.

Polymorphonuclear pleural effusion

Most pleural effusions with large numbers of polymorphs are acute¹⁴:

- [parapneumonic effusion](#): visible [consolidation](#) on chest radiograph
- [pulmonary embolism \(PE\)](#)
- [tuberculosis](#)
- [asbestos associated benign pleural disease](#)

Eosinophilic pleural effusion

Finding of an eosinophilic pleural effusion (>10% eosinophils) has no real clinical utility. They are usually found in the context of gas or blood in the pleural cavity and do not exclude a malignant cause.

Lymphocytic pleural effusion

Most lymphocytic pleural effusions are due to¹⁴:

- malignancy
- tuberculosis (maybe predominantly granulocytic)

less commonly:

- [sarcoidosis](#): pleural effusions are rare in sarcoidosis
- [rheumatoid lung disease](#)
- [chylothorax](#)

Radiographic features

Plain radiograph

Chest radiographs are the most commonly used examination to assess for the presence of pleural effusion; however, it should be noted that on a routine erect chest x-ray as much as 250-600 mL of fluid is required before it becomes evident⁶. A lateral decubitus projection is most sensitive, able to identify even a small amount of fluid. At the other extreme, [supine projections](#) can mask large quantities of fluid.

Chest radiograph (lateral decubitus)

A [lateral decubitus](#) film (obtained with the patient lying on their side, effusion side down, with a cross table shoot through technique) can visualize small amounts of fluid layering against the dependent parietal pleura.

Chest radiograph (erect)

Both PA and AP erect films are insensitive to small amounts of fluid. Features include:

- [blunting of the costophrenic angle](#)
- blunting of the cardiophrenic angle
- fluid within the horizontal or oblique fissures
- eventually, a meniscus will be seen, on frontal films seen laterally and gently sloping medially
(note: if a [hydropneumothorax](#) is present, no such meniscus will be visible)
- with large volume effusions, mediastinal shift occurs away from the effusion (note: if coexistent collapse dominates then mediastinal shift may occur towards the effusion)

Lateral films are able to identify a smaller amount of fluid as the costophrenic angles are deepest posteriorly.

A [subpulmonic effusion](#) (a.k.a. infrapulmonary effusion) may be seen when there is previously established pulmonary disease, but can also be encountered in normal lungs. It can be difficult to identify on frontal radiographs. They are more common on the right, and usually unilateral. The following features are helpful⁶:

- right: peak of the hemidiaphragm is shifted laterally
- left: increased distance between lower lobe air and [gastric bubble](#)

A lateral decubitus film is again ideal.

Chest radiograph (supine)

Large amounts of fluid can be present on [supine films](#) with minimal imaging changes, as the fluid is dependent and collects posteriorly. There is no meniscus, and only a veil-like increased density of the hemithorax may be visible. It is therefore especially difficult to identify similar sized bilateral effusions as the density of the lungs will be similar.

Ultrasound

Ultrasound allows the detection of small amounts of pleural locular fluid, with positive identification of amounts as small as 3-5 mL, that cannot be identified by radiographs, which is only capable of detecting volumes above 50 mL of liquid. Contrary to the radiological method, ultrasound allows easy differentiation of loculated pleural fluid and thickened pleura. Moreover, it is effective in guiding [thoracentesis](#) (thoracocentesis), even in small fluid collections ⁴.

When viewed in a coronal plane, with the ultrasound transducer at the mid to posterior axillary line, the space above the hemidiaphragm is typically occupied by an artifactual reflection of hepatic (or splenic) architecture, with inspiratory obscuration of the (projected location of) the posterior costophrenic sulcus as the lung descends. The spine is also obscured as it extends into the thorax. One may observe how, with the collection of fluid superior to the hemidiaphragm ¹³:

- the space above the hemidiaphragm does not [mirror](#) the echogenicity of the liver
- the [thoracic spine sign](#) appears due to the excellent acoustic medium (fluid) interposed where air once was
 - may be observed as a linear column of hyperechoic scallops with posterior acoustic shadowing extending beyond the diaphragm
- the defining sonographic features of effusion are the quad sign and sinusoid sign
 - the [quad sign](#) refers to the usual boundaries defining a pleural effusion
 - two anechoic posterior rib shadows are the horizontal boundaries
 - the parietal pleura and the visceral pleura are the remaining two surfaces, the latter being indistinguishable from the parenchyma it invests, usually referred to as the "lung line"
 - an inspiratory decrease in the depth of the effusion, classically demonstrated in M-mode, is the [sinusoid sign](#), a manifestation of intrinsically liquid dynamics (may be absent if extremely viscous)
 - if underlying lung is submerged in pleural effusion, when demonstrated in B-mode, the respiratory dynamics are reminiscent of a jellyfish, hence the [jellyfish sign](#), a subtype of the [sinusoid sign](#)

Homogeneously anechoic effusions may be either transudates or exudates, but any degree of heterogeneity is pathognomonic of a complex effusion (non-transudative). Exudative effusions often demonstrate punctate, hyperechoic foci floating within the effusion, referred to as the [plankton sign](#). Septations may be seen in the pleural fluid, and may indicate underlying infection but can be seen in chylothorax or hemothorax ⁸. The appearance of the "[hematocrit sign](#)" may be observed in hemothorax, with a surface layer of anechoic fluid sitting atop a settled, fine echogenic sediment.

Ultrasound can be used in the assessment of pleural effusion volume. Refer to the article "[pleural effusion volume \(ultrasound\)](#)" for more information

CT

CT scanning is excellent at detecting small amounts of fluid and is also often able to identify the underlying intrathoracic causes (e.g. [malignant pleural deposits](#) or [primary lung neoplasms](#)) as well as subdiaphragmatic diseases (e.g. [subdiaphragmatic abscess](#)).

CT is not able to differentiate between a transudative or exudative pleural effusion with similar fluid densities and non-differentiating rates of loculation and pleural thickening^{9,10}. However, CT can help distinguish between pleural effusion and [pleural empyema](#) (see [pleural effusion vs pleural empyema](#)).

Precise volume of the effusion can be calculated using proper volumetry, however in clinical practice this labor intensive but accurate quantification is rarely needed. Various formulas has been thus proposed which allow estimation of the effusion volume using simple caliper measurements.

Effusion volume can be estimated using the following formula, where b = the maximum depth of the effusion measured in the axial plane in centimeters¹⁶:

$$\text{Volume (mL)} = 0.365 \times b^3 - 4.529 \times b^2 + 159.723 \times b - 88.377$$

In routine practice the above calculation is rarely needed (online calculators are available for this purpose¹⁷), as with a slight rounding maximum effusion depths of 2, 4, 6, 8, and 10 cm represent volumes of approximately 200, 500, 800, 1100, and 1400 mL of pleural effusion respectively.

Treatment and prognosis

The treatment of pleural effusions is usually targeted to the underlying condition (e.g. congestive cardiac failure or malignancy). Symptomatic patients with large effusions may be treated by therapeutic aspiration ([thoracentesis](#)).

When effusions are very large, this can safely be done 'blind' although increasingly ultrasound is used to at least mark an appropriate site. Ultrasound-guided aspiration is reliable and fast and enables loculated effusions to be drained. A catheter can be left in situ, although care must be taken to ensure that it is connected either to an underwater drain or to a sealed system such that air cannot enter the pleural cavity.

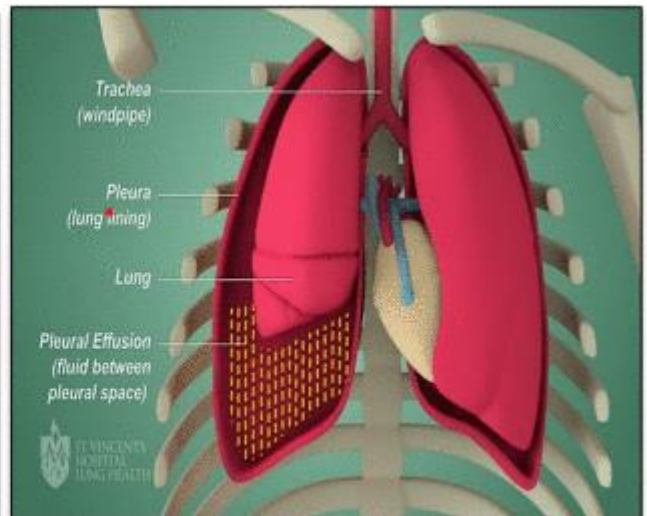
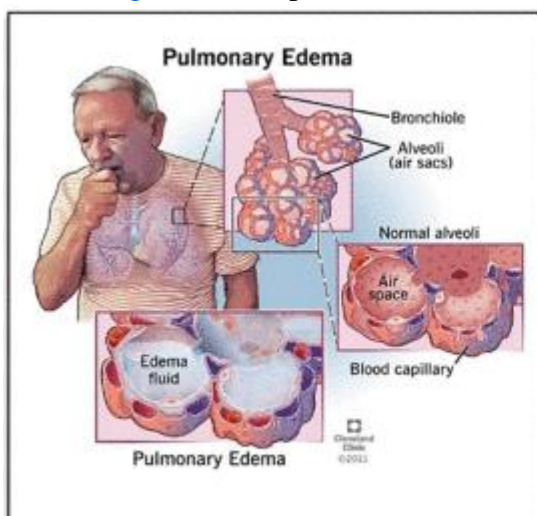
If effusions reaccumulate despite repeated aspirations and systemic therapy (where appropriate), a tunneled semipermanent pleural drain or [video-assisted thoracic surgery \(VATS\)](#) pleurodesis can be considered.

Differential diagnosis

Imaging differential considerations include:

- [elevated hemidiaphragm](#), e.g. [hepatomegaly](#), [phrenic nerve palsy](#)
- collapse or consolidation
- pleural thickening, e.g. old [tuberculosis](#) or [empyema](#)
- [inferior pulmonary ligament](#)
- poor radiographic technique

- [extrapleural lipomatosis](#) - differential diagnosis on CT
- This paper presents a novel multiclass system designed to detect pleural effusion and pulmonary edema on chest X-ray images, addressing the critical need for early detection in healthcare. A new comprehensive dataset was formed by combining 28,309 samples from the ChestX-ray14, PadChest, and CheXpert databases, with 10,287, 6022, and 12,000 samples representing Pleural Effusion, Pulmonary Edema, and Normal cases, respectively. Consequently, the preprocessing step involves applying the Contrast Limited Adaptive Histogram Equalization (CLAHE) method to boost the local contrast of the X-ray samples, then resizing the images to 380×380 dimensions, followed by using the data augmentation technique. The classification task employs a deep learning model based on the EfficientNet-V1-B4 architecture and is trained using the AdamW optimizer. The proposed multiclass system achieved an accuracy (ACC) of 98.3%, recall of 98.3%, precision of 98.7%, and F1-score of 98.7%. Moreover, the robustness of the model was revealed by the Receiver Operating Characteristic (ROC) analysis, which demonstrated an Area Under the Curve (AUC) of 1.00 for edema and normal cases and 0.99 for effusion. The experimental results demonstrate the superiority of the proposed multi-class system, which has the potential to assist clinicians in timely and accurate diagnosis, leading to improved patient outcomes. Notably, ablation-CAM visualization at the last convolutional layer portrayed further enhanced diagnostic capabilities with heat maps on X-ray images, which will aid clinicians in interpreting and localizing abnormalities more effectively.
- 1. Introduction
- Detecting pulmonary edema and pleural effusion using chest X-rays is crucial for the diagnosis of diseases [1,2]. Pulmonary edema occurs due to fluid buildup in the lungs' alveoli [3]. Conversely, pleural effusion is a disorder indicated by the abnormal fluid buildup in the membranes surrounding the lungs [4]. [Fig. 1a](#) depicts pulmonary edema [5] and [Fig. 1b](#) shows pleural effusion [6].



- (a)
- [Download: Download high-res image \(634KB\)](#)
- [Download: Download full-size image](#)

- Figure 1. (a) Pulmonary edema (Reprinted from reference [5]); (b) Pleural effusion (Reprinted from reference [6])
- In this context, it is crucial to classify whether the fluid is located inside the lung tissue and air sacs (pulmonary edema) or within the pleural space (pleural effusion) [7,8]. Therefore, diagnostic imaging techniques, such as X-rays, are paramount in identifying the presence and extent of these medical conditions, enabling healthcare practitioners to make timely and precise diagnoses [9]. Overall, the complexity in detecting pulmonary edema and pleural effusion underscores the need for a multidisciplinary approach involving clinicians, radiologists, and other specialists to ensure accurate diagnosis and appropriate management.
- Additionally, the distinction between pulmonary edema and pleural effusion using chest X-rays will lead to identification the underlying causes of fluid accumulation in the chest. It will also help medical professionals suggest the appropriate management of these disorders and an appropriate treatment approach. For instance, detection of pulmonary edema might indicate congestive heart failure or pneumonia, necessitating specific therapeutic interventions [10]. Conversely, the detection of pleural effusion would require different treatment strategies involving drainage through thoracentesis and chest tube [11].
- Likewise, accurately classifying the location of the fluid helps in determining the precise underlying causes, ensuring that patients receive the most effective and tailored care to improve their overall health outcomes [8,12].
- Deep learning techniques have demonstrated remarkable advancements in the domain of medical image analysis, particularly in disease detection and diagnosis [13–15]. Deep Convolutional Neural Networks (CNNs) have proven exceptional capabilities in extracting intricate features from complex images, making them an ideal candidate for the detection of pulmonary edema and pleural effusion [16–18].
- EfficientNet is a family of CNNs that excel at achieving high accuracy and is computationally efficient [19]. EfficientNet was developed to scale the depth, width, and resolution of the model using a compound coefficient to optimize performance [20]. This approach has led to state-of-the-art results on the task of image classification for various applications while minimizing computational demands [21]. In particular, the EfficientNet-V1-B4 architecture is known for its exceptional efficiency in terms of the model size and computational resources. It achieves superior performance with fewer parameters compared to traditional architectures, making it well-suited for resource-constrained environments commonly encountered in medical settings. This efficiency translates to faster inference times and reduced computational costs, facilitating the real-time or near-real-time analysis of medical images for timely diagnosis and intervention. Coupled with the AdamW optimizer, which integrates the advantages of the Adam optimizer with weight decay techniques, detection algorithms can achieve superior convergence rates and model generalization. AdamW is an extension of the Adam optimizer commonly used for training neural networks [22]. It directly incorporates weight decay into its formulation improving generalization by preventing excessive weight growth. This modification helps control model complexity and enhances training stability.
- Accordingly, by introducing EfficientNet-V1-B4 Architecture and AdamW in medical imaging analysis, healthcare professionals can expect improved diagnostic

accuracy, faster processing times, and enhanced decision-making capabilities, ultimately leading to better patient outcomes and more effective treatment plans.

- The contributions of this study are as follows:
- A multi-class medical diagnosis system was developed to describe the accumulation of fluid in the lungs from perspective of image processing. Thus, the system categorizes three patterns using chest X-ray images including pleural effusion, pulmonary edema, and normal cases.
- The utilization of the EfficientNet-V1-B4 architecture associated with the AdamW optimizer in the context of pulmonary edema and pleural effusion detection from chest X-ray images represents a novel application and exploration of deep learning models for medical image analysis.
- The localization of pleural effusion and pulmonary edema diseases is accomplished by utilizing the ablation-CAM technique and is graphically presented using heatmap data visualization.
- By automating this classification process, medical professionals can save valuable time by achieving early diagnosis while ensuring more accurate diagnoses. The remainder of this paper is organized as follows. The related work is presented in [Section 2](#). [Section 3](#) describes the research methodology. The empirical results are analyzed and discussed in [Section 4](#). The conclusions of this research and future work are presented in [Section 5](#).
- 2. Related Work
- Fluid accumulation in the lungs is a life-threatening medical emergency that requires timely diagnosis and intervention and is known as pulmonary edema. Traditional methods for detecting pulmonary edema in medical imaging have limitations, leading to the demand for more accurate and efficient approaches. The promising results of artificial intelligence in various medical fields, including the detection of pulmonary edema, have encouraged the development of advanced methodologies. One major challenge hindering the advancement of CNNs in medical image analysis is the necessity of constructing ground-truth data based on specialists' opinions.
- Deep CNNs have been applied in research [[23–27](#)] to classify different types of radiographs, such as X-rays, CT scans, and ultrasounds. CNNs are used to diagnose various diseases, such as pulmonary edema, pulmonary effusion, pneumonia, COVID-19, and pneumothorax. Despite demonstrating promise for radiographic interpretation, these early studies generally lacked the level of specificity and granularity required for practical diagnostic utility.
- Based on the expansion of using Artificial Intelligence (AI) in detecting diseases, Wang et al. [[28](#)] compared several deep learning techniques for diagnosing pulmonary edema and estimating the severity of the case, and the dataset used was MIMIC-CXR for images and reports [[29](#)]. According to previous studies [[30,31](#)], there are approximately 77% accuracy among radiologists and 59% accuracy among ED physicians. Edema severity was classified in 3058 cases as mild, 1414 moderate cases, and severe in 296 cases.
- 2.1. Related Studies on CNN-Based Detection of Pulmonary Edema
- Serte et al. [[18](#)] studied pulmonary edema disease as a result of heart failure depending on chest radiographs. Researchers constructed a dataset of 27,748 front-chest radiographs over nearly six years. The collected images were in the range of

1.4–4.7 k in height and width with 80% training set, 10% validation, and a test group of 10%. Training was carried out in two stages (pipelines) to train a branched CNN based on ResNet152v2 architecture. The goal is to cooperatively predict B-type Natriuretic Peptide (BNP) or BNPP (BNP precursor) cases. With a preset learning rate of 1e-5 and a patch size of 16, Adam's optimizer was used to train all CNNs. The region of attention was determined using a heatmap. Another factor that is considered is the blur sensitivity. Consequently, the trained models attained an AUC of 0.801 for the detection of pulmonary edema.

- In [32], a 2.5D CNN model was developed to detect multiple diseases, such as: atelectasis, pneumonia, edema, and nodules. The study investigated 5000 CT images that contained 156 edema cases, 225 pneumonia cases, and other cases. The research split the image set for each disease into training, validation, and test sets. The model achieved accuracies of 0.963, 0.818, 0.878, and 0.784, for edema, atelectasis, pneumonia, and nodule, respectively. Moreover, AUC of 0.940, 0.891, 0.869, and 0.784 were obtained for categorizing edema, atelectasis, pneumonia, and nodule diseases, respectively.
- In [33], a 2.5D CNN model was developed to detect multiple diseases, that are: atelectasis, pneumonia, edema, and nodules. The study investigated 5000 CT images that contained 156 edema cases, 225 pneumonia cases, and other cases. The research split the image set for each disease into training, validation, and test sets. As a result, the model achieved an accuracy of 0.963, 0.818, 0.878, and 0.784, for edema, atelectasis, pneumonia, and nodule, respectively. Moreover, The AUC of 0.940, 0.891, 0.869, and 0.784 were attained for categorizing edema, atelectasis, pneumonia, and nodule diseases, respectively. As shown in [Table 1](#), a summary of previous studies on the detection of pulmonary edema using CNN models from chest X-ray images is provided.
- Table 1. Summary of previous studies on the detection of pulmonary edema using CNN models from chest X-ray images

• Study	• Architecture	• Performance
• Serte et al. [18]	• ResNet152v2-CNN	• AUC = 0.801
• Hayat [32]	• DesneNet-CNN	• AUC = 0.714
• Geng et al. [33]	• 2.5D-CNN	<ul style="list-style-type: none"> • ACC = 0.963 • AUC = 0.940

- 2.2. Related Studies on CNN-Based Detection of Pleural Effusion
- Previous studies in the domain of pleural effusion detection have explored various approaches and architectures to improve the accuracy and efficiency of diagnostic systems. With the aim of automating Lung Ultrasound (LUS) image evaluation for pleural effusion detection, Hammon et al. [30] employed a deep-learning model that was constructed based on the Regularized Spatial Transformer Network (Reg-STN) architecture to perform binary classification of pleural effusion in clinical LUS imaging. The dataset, obtained from the Royal Melbourne Hospital, consisted of 623

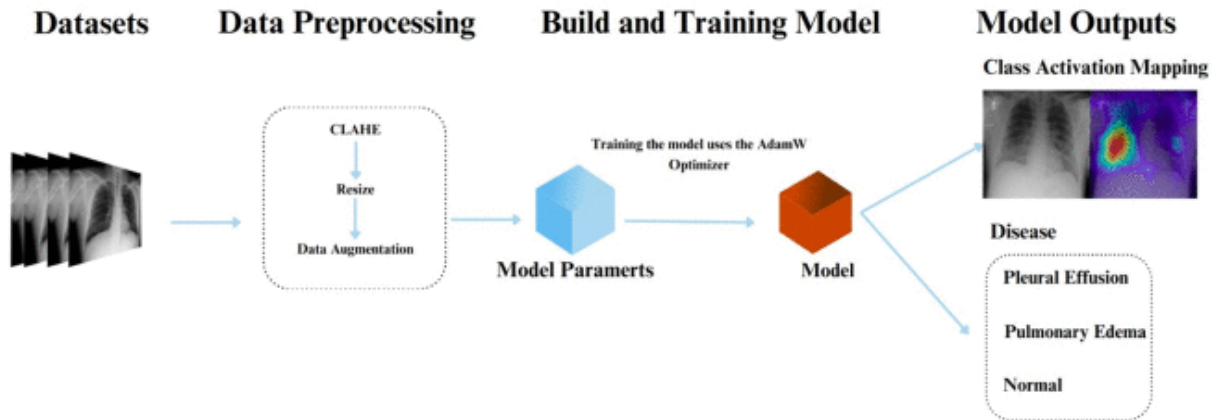
videos containing 99,209 2D LUS images obtained from examinations of 70 patients using a phased array transducer. This model was trained using weakly supervised and supervised methodologies utilizing a video-based labeling approach, resulting in an accuracy of 91.1%, and a frame-based labeling approach, resulting in an accuracy of 92.4%. Notably, the reference was proficient clinicians who assessed the interpretation of images.

- Researchers in [34] applied a deep learning model based on the ResNet18 architecture to the chest radiography images. The model was applied to identify pleural effusion arising from three types of respiratory disorders, namely tuberculosis, COVID-19, and pneumonia. Hence, the developed system can detect these three diseases once they occur at an early stage before evolving into pleural effusion. Three experiments were conducted for binary classification. Consequently, the performance in terms of accuracy for early detection of pleural effusion disease from tuberculosis, COVID-19, and pneumonia was 99%, 100%, and 75%, respectively. In contrast, a multiclass experiment was applied, which included the following categories: tuberculosis, COVID-19, pleural effusion, bacterial pneumonia, and viral pneumonia. Thus, the best result was obtained for bacterial pneumonia detection, with an accuracy of 83% and an AUC of 81%. Furthermore, the multiclass system detected pleural effusion with an accuracy of 82% and AUC of 77%.
- In a study by Bar et al. [35], the identification of various pathologies, such as right pleural effusion, from chest radiographs was investigated. Their analysis utilized a CNN trained on non-medical data, achieving an AUC of 0.95. Lakhani et al. [36] explored deep-learning approaches for tuberculosis detection on chest radiographs containing pleural effusion, miliary patterns, and cavitation, and achieved an impressive AUC of 0.99. As shown in [Table 2](#), a summary of previous studies on the detection of pleural effusion using CNN models from chest X-ray images is provided.
- [Table 2](#). Summary of previous studies on the detection of pleural effusion using CNN models from chest X-ray images

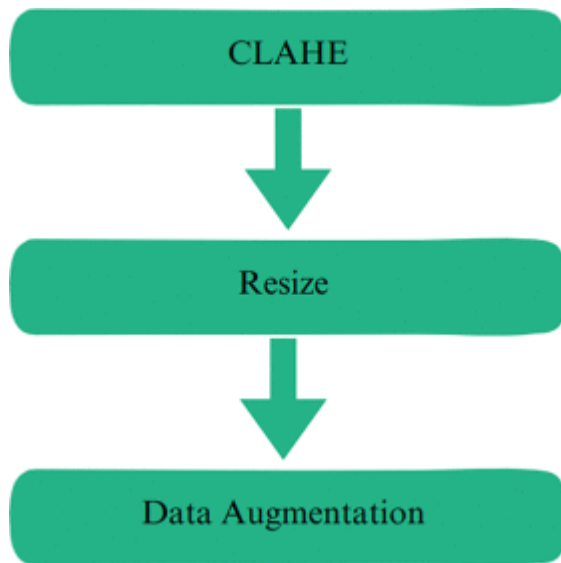
• Study	• Architecture	• Performance
• Serte et al. [34]	• ResNet18-CNN	• ACC = 0.82
		• AUC = 0.77
• Bar et al. [35]	• CNN + classical features	• AUC = 0.95
• Lakhani et al. [36]	• DCNNs (AlexNet and GoogLeNet)	• AUC = 0.99

- 3. Material and Methodology
- As essential as it is in practice, this study developed an AI system to detect fluid buildup in the lungs by categorizing three patterns using chest X-ray images including pleural effusion disease, pulmonary edema disease, and normal cases as illustrated in [Fig. 2](#). The proposed computer vision-based medical classification system encompassed various stages including Data Preprocessing, Build and Training Model (learning), and Model Output (testing). [Fig. 2](#) illustrates the research methodology. From this perspective, chest X-ray images will pass through a preprocessing stage

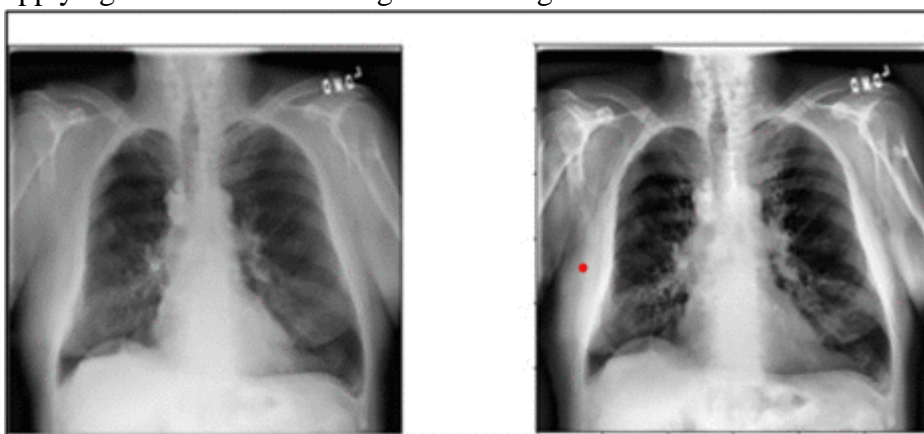
before being fed into the training model. Furthermore, the output of the system includes class activation mapping and the category to which each test image belongs.



- [Download: Download high-res image \(157KB\)](#)
- [Download: Download full-size image](#)
- Figure 2. The research methodology
- 3.1. Datasets
- With the aim of conducting a classification task to reveal the presence or absence of pleural effusion and pulmonary edema disorders in the lungs using X-ray images, a new dataset of 28,309 samples was formed by combining several public datasets, including ChestX-ray14 [37], PadChest [38], and CheXpert [39]. The new dataset under consideration was distributed among three classes as follows: approximately 10,287 samples depicting pleural effusion, about 6022 samples representing pulmonary edema, and 12,000 samples exhibiting normal cases.
- 3.2. Data Preprocessing
- During this stage, a stratified split of the medical image dataset was conducted, with 85% allocated to the training set and 15% to the test set. Thus, the training and test sets are independent. This stratification was aimed at maintaining a consistent distribution of classes across both the training and test sets. Particularly, pixel normalization was excluded from the preprocessing steps, as empirical evidence suggests its unnecessary approach in certain medical image classification tasks [40].
- To achieve the computer vision classification goal, the image data should be handled properly before reaching the input layer of the model. For the application at hand, a dedicated pipeline was employed on the image data by conducting three sequential steps, as illustrated in Fig. 3. First, enhancing the contrast of the chest X-ray images was enhanced using the CLAHE approach. Second, all images were resized to 380×380 pixels. Lastly, multiple data augmentation techniques were employed.



- [Download: Download high-res image \(41KB\)](#)
- [Download: Download full-size image](#)
- Figure 3. Preprocessing steps
- 3.2.1. CLAHE Technique
- The CLAHE technique has been used in various image processing applications because of its capability to enhance image contrast by partitioning the image into small blocks and equalizing the histogram of each block. This method also mitigates contrast amplification within each block, thus minimizing noise amplification [41]. It serves to improve image contrast, facilitates better visibility and interpretation, and is adept at enhancing image details [42]. [Fig. 4a](#) shows the original X-ray image selected from the data under consideration. Conversely, [Fig. 4b](#) illustrates the enhanced X-ray image after employing the CLAHE technique, which demonstrates the contrast improvement compared to the original X-ray image proving the effectiveness of applying CLAHE in rendering certain lung details more discriminant.



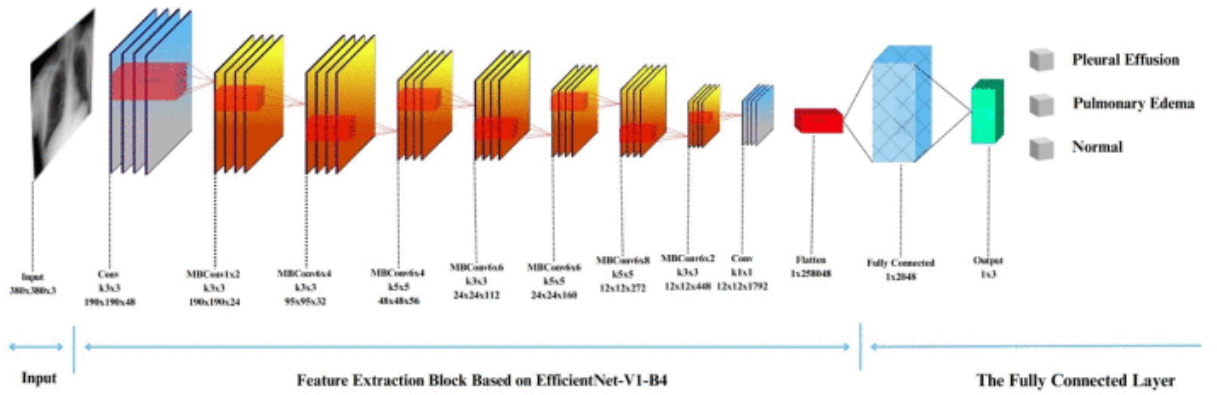
- [Download: Download high-res image \(195KB\)](#)
- [Download: Download full-size image](#)
- Figure 4. (a) The original X-ray image; (b) The enhanced X-ray image after employing CLAHE
- 3.2.2. Resize

- Determining the image size for training CNN is important when considering the trade-offs between accuracy, speed, and memory requirements [43]. Larger image sizes typically exhibit better accuracy, but they also require more computation and memory [44]. Additionally, the benefits of using larger images tend to diminish as the size increases [45].
- CNNs frequently downsample the dimensions of an input image, resulting in an irregular final size [46]. To avoid this, it is advisable to employ a square image size during the training phase [47]. In our approach, we resized all images to 380×380 pixels, maintaining the original aspect ratio and implementing zero-padding as needed.
- 3.2.3. Data Augmentation
- To improve the performance of the deep learning model and promote its capacity for generalization, a data-augmentation approach was employed. Data augmentation involves integrating subtly modified versions of current data or generating synthetic data based on existing samples, thereby expanding the effective dataset size. For this purpose, a total of six augmentation methods were adopted, including: CutMix [48], MixUp [49], CenterCrop, RandomChannelShift [50], RandomGaussianBlur [51], and Random Brightness [50] transformations during the training process, aiming to improve the robustness of the model.
- 3.3. Build and Training Model
- Attaining superior performance for image categorization necessitates not only creating a superb architecture but also selecting an appropriate optimizer that can significantly minimize the loss function. Thus, this study presents a deep learning model that was constructed based on the EfficientNet-V1-B4 architecture along with the AdamW optimizer that was utilized for training this model.
- 3.3.1. EfficientNet-V1-B4 Architecture
- The EfficientNet-V1 architecture was introduced by Tan and Le in 2019 [20] in which a novel compound scaling approach was proposed. In this view, the EfficientNet-V1 model uses R to uniformly scale all the dimensions of the network including the width, depth, and resolution. Thus, the scaling method of the model is mathematically described as follows [20]:

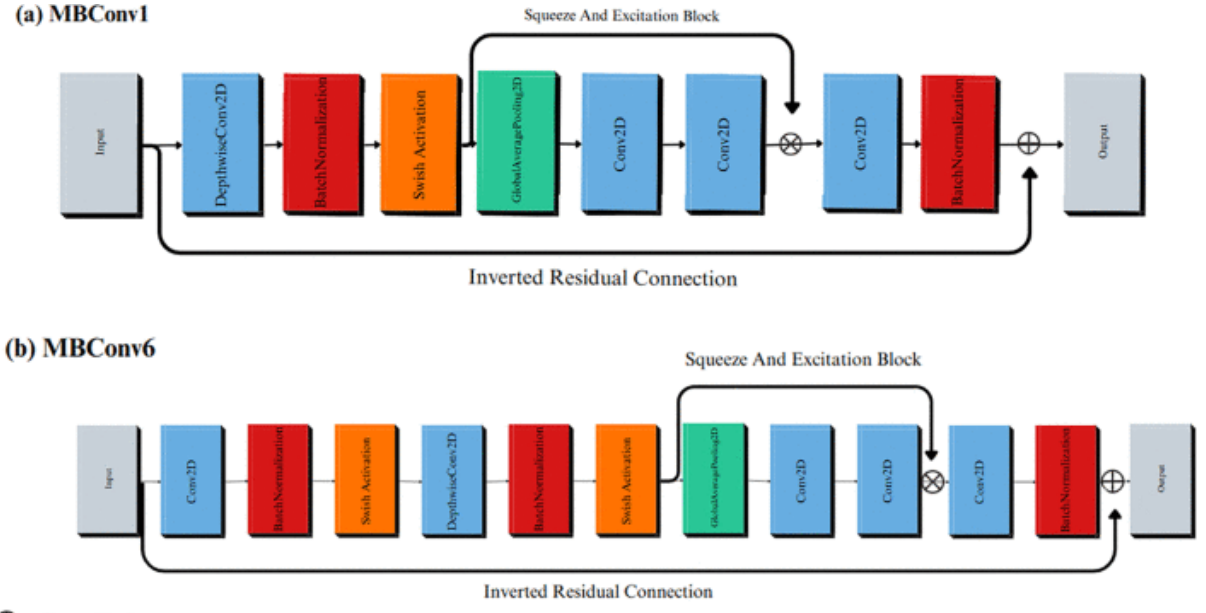
$$\text{depth} = \alpha R, \quad (1) \quad \text{width} = \beta R, \quad \text{and resolution} = \gamma R \text{ s.t. } \alpha, \beta, \gamma \geq 1, \quad \alpha \beta \gamma^2 \approx 2.$$

where the coefficients α, β, γ are constant, and they are specified by a small grid search, whereas the value of (R) is determined by the user depending on the available resources to scale the model. As illustrated in Eq. (1), the Floating-Point Operations (FLOPs) of the ordinary convolution operation are typically proportional to $\alpha \beta \gamma^2$. Considering the restriction of $\alpha \beta \gamma^2 \approx 2$, such that for each change in the value of R, the overall FLOPs roughly increase by $2R$.
- Therefore, it can be straightforward to increase the dimensions of the network by (R) if there is a need to use $2R$ times more computational resources. Hence, utilizing the abovementioned compound scaling strategy has an intuitive implication if there is a larger input image that requires additional layers in the network to expand its receptive area and additional channels to obtain more fine-grained patterns. Hence, scaling the network dimensions leads to a systematic increase in the performance of the model.

- Furthermore, there are eight variations of EfficientNet-V1, referred to as EfficientNet-V1-B0 through EfficientNet-V1-B7. This study employs EfficientNet-V1-B4. Fig. 5 depicts the details of the EfficientNet-V1-B4 architecture considered in this study. The architecture of EfficientNet-V1-B4 is segmented into seven blocks, called Mobile Inverted Bottleneck Convolution (MBConv), which are the elementary building blocks of EfficientNet-V1-B4, followed by a fully connected layer. For a particular stage(s) within this architecture, the block appears as MBConv $X \times L$, where the notation $X = 1$ and $X = 6$ indicate the block type signify the standard Swish activation function, and (L^s) denotes the number of layers. The kernel size associated with the MBConv X block also appears under the block type.

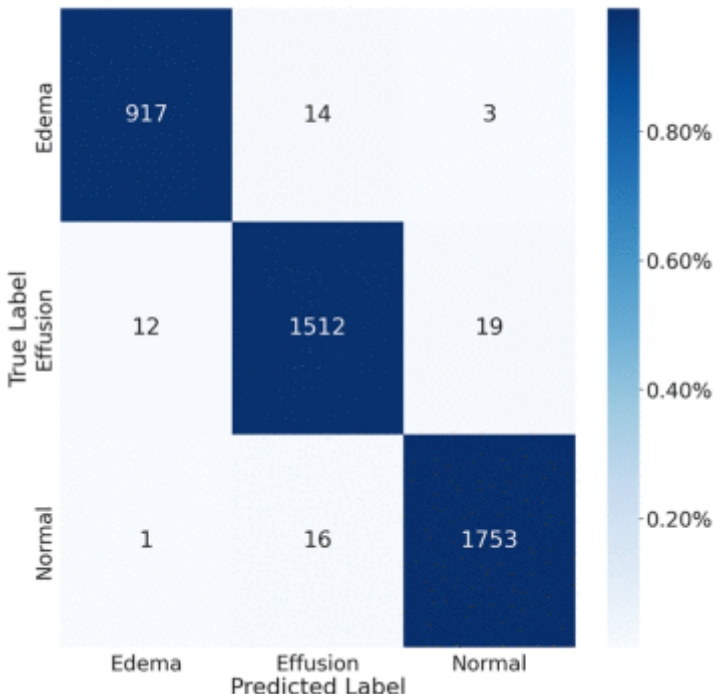


- [Download: Download high-res image \(237KB\)](#)
- [Download: Download full-size image](#)
- Figure 5. The EfficientNet-V1-B4 architecture
- Lastly, the input resolution ($H^s \times W^s$), and the number of output channels (C^s), is depicted as $(H^s \times W^s \times C^s)$, respectively. For example, in the second stage of the architecture where ($S = 2$), the $\text{MBConv}1 \times 2$ notation indicates that the $\text{MBConv}1$ block is repeated twice ($L=2$), the kernel size is ($k3 \times 3$), and the notation ($190 \times 190 \times 24$) implies the input resolution which is (190×190), and the number of channels is (24).
- In this study, the optimal performance was pursued by fine-tuning the pre-trained weights of EfficientNet-V1-B4 using Noisy Student data. Subsequently, a fully connected layer with three neurons was used to represent the class scores (i.e., the output layer).
- Furthermore, the MBConvX blocks utilize the Swish activation function and squeeze-and-excitation (SE) optimization which enables the efficient extraction of high-quality features, and minimize computational complexity while maximizing accuracy. Additionally, MBConv's lightweight design extracts informative features from early stages, while SE dynamically refines them, resulting in sharper detections and improved accuracy compared to traditional Convolutional Neural Networks. Fig. 6a illustrates MBConv1, while Fig. 6b presents MBConv6, both representing distinct design points in the EfficientNet-V1-B4 architecture. MBConv1 emphasizes early feature extraction with minimal computational cost, making it particularly well-suited for the initial stages of the network. By contrast, MBConv6 concentrates on advanced feature refinement, achieving heightened accuracy although with a modest increase in complexity. The deliberate utilization of MBConvX variants in this manner enables EfficientNet-V1-B4 to achieve a balance between efficiency and accuracy.



- [Download: Download high-res image \(262KB\)](#)
- [Download: Download full-size image](#)
- Figure 6. The MBConv blocks in the EfficientNet-V1-B4 architecture. (a) MBConv1; (b) MBConv6
- 3.3.2. AdamW Optimizer
- An AdamW optimizer was used to train the model. The AdamW optimizer is an extension of the Adam optimizer with the addition of a weight decay regularization approach [22]. Furthermore, weight decay serves as a method to mitigate overfitting by imposing penalties on substantial weights.
- Accordingly, the Adam optimizer exhibited comparatively reduced efficiency in weight regularization when compared to alternative optimizers, such as SGD with momentum. However, AdamW disentangles the weight decay from the adaptive estimation of the first and second moments of the gradients. This decoupling empowers AdamW to enhance the weight regularization more efficiently without compromising the speed of convergence.
- 4. Model Outputs
- In this section, the experimental settings, and results for the dataset under consideration are illustrated. The performance of the classification model was evaluated based on complexity and different metrics including accuracy (A), precision (P), recall (R), and F1-score. Finally, Ablation-based Class Activation Mapping (Ablation CAM) was employed to provide meaningful and interpretable explanations of the results.
- 4.1. Experiments Setting
- In this study, TPU 3-8 was utilized to train the network. Subsequently, the training and testing phases occurred within the same environment, employing the Keras deep learning framework and Python 3.8 as the programming language. Network training involved the utilization of the hyperparameters outlined in [Table 3](#).
- Table 3. Hyperparameters

• Parameter	• Value
• Input size	• $380 \times 380 \times 3$
• Batch size	• 256
• Learning rate	• 1e-4
• Optimizer	• AdamW
• Epochs	• 70
• Loss function	• Categorical crossentropy
<ul style="list-style-type: none"> • 4.2. Computational Complexity • The computational complexity of a CNN is an important consideration for its practical deployment and can be analyzed along two dimensions which are spatial and temporal [52]. The spatial complexity (SC) indicates the storage requirements (i.e., disk space) of a trained CNN model, including both its parameters and intermediate feature maps. The temporal complexity (TC) reflects the computational cost, commonly measured in floating-point operations per second (FLOPS), required for the CNN to make predictions. For the proposed CNN model evaluated in this study, we obtained SC of 243 MB and TC of 4.51 GigaFLOPS. These values can be used to assess the resource requirements and inference speed of a model in real-world applications. 	
<ul style="list-style-type: none"> • 4.3. Classification Performance Evaluation • The performance evaluation of the proposed model on the test set relies on the utilization of a confusion matrix. The accurate determination of this matrix requires knowledge of the true values associated with the validation data. As illustrated in Fig. 7, the confusion matrix was implemented to evaluate the performance of the model. In this view, multiple measures were computed including P, R, A, and F-1, utilizing the predetermined methods described in previous research [53]. The formulations for these evaluation measures are detailed in Eqs. (2) through (5). 	

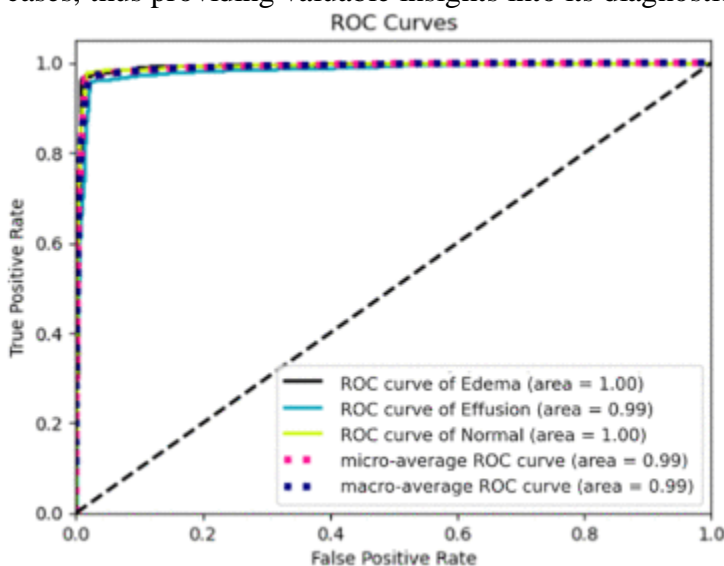


- [Download: Download high-res image \(149KB\)](#)
- [Download: Download full-size image](#)
- Figure 7. The confusion matrix for chest X-ray images
- $(2)P = \frac{TP}{TP+FP}$ (3) $R = \frac{TP}{TP+FN}$ (4) $A = \frac{TP+TN}{TP+TN+FP+FN}$ (5) $F1 = 2 \cdot PR + R$
- Specifically, the TP represents True Positives, denoting correctly identified positive instances. TN represents True Negatives, signifying correctly identified negative instances. FP represents False Positives, indicating instances incorrectly identified as positives. FN represents False Negatives, representing instances incorrectly identified as negatives.
- The results of the calculation of the aforementioned matrices are presented in [Table 4](#), which shows that the developed system classifies pleural effusion, pulmonary edema, and normal patterns with a high classification rate compared with previous studies as shown in [Tables 1](#) and [2](#). According to this viewpoint, the average achieved accuracy was approximately 0.983, the average accomplished precision was approximately 0.987, the attained average recall value was roughly 0.983, and the average F-1 was score approximately 0.987. These findings confirm that the classification system is precise and robust in identifying pleural effusion and pulmonary edema disorders using X-ray images.
- Table 4. The classification report of our proposed approach to X-ray images

• Classes	• Precision	• Recall	• F1-score	• Accuracy
• Edema	• 0.99	• 0.98	• 0.98	• 0.98
• Effusion	• 0.98	• 0.98	• 0.99	• 0.98
• Normal	• 0.99	• 0.99	• 0.99	• 0.99

• Classes	• Precision	• Recall	• F1-score	• Accuracy
• Average	• 0.987	• 0.983	• 0.987	• 0.983

- Finally, we confirmed a comprehensive evaluation of the model's performance across various sensitivity and specificity thresholds. The ROC curve tool was used specifically to analyze three medical classes: pulmonary edema, pleural effusion, and normal cases using the dataset of X-ray images under consideration in this study, as represented in [Fig. 8](#). The results revealed that the AUC was 1.00 for pulmonary edema and normal cases. Additionally, the AUC was 0.99 for pleural effusion disease. These ROC evaluations confirmed the robustness of the developed categorization system that differentiated between pulmonary edema, pleural effusion, and normal cases, thus providing valuable insights into its diagnostic capabilities.



- [Download: Download high-res image \(84KB\)](#)
- [Download: Download full-size image](#)
- Figure 8. ROC curves for pulmonary edema, pleural effusion, and normal cases using chest X-rays
- This work proves the effectiveness of the proposed neural network architecture combined with the AdamW optimizer for the detection of Pulmonary Edema and Pleural Effusion diseases. The results were compared with well-known classification architectures such as VGG19, DenseNet121, InceptionV3, EfficientNet, and ResNet101. Hence, the average accuracy of these architecture models was assessed using various training-based optimizers including SGD, Adagrad, RMSprop, Adam, Radam, and AdamW. [Table 5](#) compares the aforementioned optimizers and architectures. As a result, the proposed model achieved the highest average accuracy of 0.983 when employing the AdamW optimizer across EfficientNet-V1-B4 compared to the others utilizing the same datasets applied in this study.
- Table 5. Comparison of various optimizers applied to renowned architectures in terms of average accuracy on the datasets used in this study

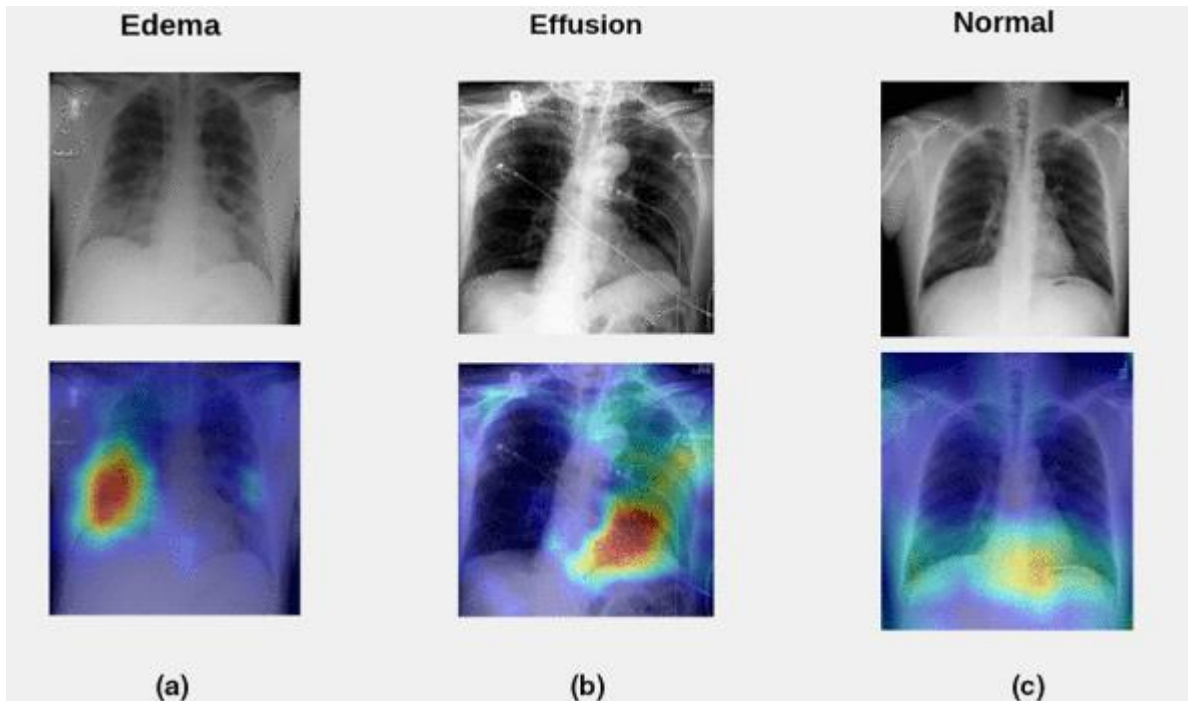
• Model	• SGD	• Adagrad	• RMSprop	• Adam	• Radam	• AdamW
• VGG19	• 0.820	• 0.814	• 0.81	• 0.822	• 0.825	• 0.83
• DenseNet121	• 0.850	• 0.832	• 0.844	• 0.858	• 0.861	• 0.864
• InceptionV3	• 0.832	• 0.834	• 0.830	• 0.845	• 0.847	• 0.85
• ResNet101	• 0.871	• 0.870	• 0.871	• 0.879	• 0.883	• 0.881
• EfficientNetV1-B0	• 0.922	• 0.924	• 0.92	• 0.948	• 0.95	• 0.951
• EfficientNetV1-B1	• 0.923	• 0.927	• 0.921	• 0.945	• 0.951	• 0.957
• EfficientNetV1-B2	• 0.934	• 0.935	• 0.933	• 0.955	• 0.966	• 0.968
• EfficientNetV1-B3	• 0.947	• 0.949	• 0.949	• 0.959	• 0.968	• 0.97

• Model	• S G D	• Ad agr ad	• RM Spr op	• A d a m	• R ad a m	• Ad am W
	5 1			6 7		
• EfficientNetV1-B4	• 0 .9 6 1	• 0.9 53	• 0.95 9	• 0. 9 7 5	• 0. 97 9	• 0.9 83
• EfficientNetV1-B5	• 0 .9 6 1	• 0.9 51	• 0.96	• 0. 9 7	• 0. 97 3	• 0.9 81
• EfficientNetV1-B6	• 0 .9 6 1	• 0.9 52	• 0.96 2	• 0. 9 7 2	• 0. 97 5	• 0.9 78
• EfficientNetV1-B7	• 0 .9 6 2	• 0.9 55	• 0.96 4	• 0. 9 7 1	• 0. 97 6	• 0.9 79
• EfficientNetV1-L2	• 0 .9 6 2	• 0.9 57	• 0.96 4	• 0. 9 7 4	• 0. 97 6	• 0.9 80
• EfficientNetV2-B0	• 0 .9 2 8	• 0.9 23	• 0.92	• 0. 9 4 1	• 0. 94 7	• 0.9 48
• EfficientNetV2-B1	• 0 .9 3	• 0.9 25	• 0.92 2	• 0. 9 4 3	• 0. 95 0	• 0.9 50

• Model	• SGD	• Adagrad	• RMSprop	• Adadelta	• Radam	• AdamW
• EfficientNetV2-B2	• 0.935	• 0.928	• 0.925	• 0.948	• 0.953	• 0.955
• EfficientNetV2-B3	• 0.943	• 0.938	• 0.935	• 0.952	• 0.956	• 0.956
• EfficientNetV2T	• 0.953	• 0.955	• 0.946	• 0.957	• 0.958	• 0.961
• EfficientNetV2_GC	• 0.957	• 0.963	• 0.958	• 0.976	• 0.978	• 0.972
• EfficientNetV2S	• 0.956	• 0.957	• 0.951	• 0.976	• 0.978	• 0.979
• EfficientNetV2M	• 0.963	• 0.966	• 0.956	• 0.979	• 0.979	• 0.981
• EfficientNetV2L	• 0.969	• 0.966	• 0.96	• 0.976	• 0.974	• 0.979
• EfficientNetV2XL	• 0.979	• 0.964	• 0.96	• 0.978	• 0.980	• 0.978

• Model	• S G D	• Ad agr ad	• RM Spr op	• A d a m	• R ad a m	• Ad am W
	6					
	8					

- 4.4. Localization Using Ablation-CAM
- In the context of medical image classification using deep learning, it is imperative to enhance the interpretability and significance of the results. Ablation-CAM emerged as a gradient-free methodology designed to provide visual explanations for models based on deep CNNs [54]. This technique operates by selectively ablating (removing) individual units within feature maps and measuring the subsequent drop in the activation score for the target class. The significance of each feature map unit was then quantified as the proportion of decrease in the activation score.
- To generate the ablation-CAM map, feature map units are weighted based on their calculated importance and superimposed onto the original image. The outcome is a coarse localization map that accentuates the pivotal regions in the image, thereby influencing the model's concept predictions.
- Notably, ablation-CAM exhibits superiority over the state-of-the-art Grad-CAM technique across diverse image classification tasks [55]. Because ablation-CAM is more resilient to local irregularities and saturations within the neural network, it is considered an effective and robust approach to visual interpretation. To utilize this functionality, ablation-CAM was applied after the prediction of the class label by the developed classification system. Further, we visualized the effect of employing the ablation-CAM technique on X-ray test images. [Fig. 9a](#) shows the heatmap for a test image from the pulmonary edema class; [Fig. 9b](#) depicts the heatmap for a test image from the pleural effusion class; and [Fig. 9c](#) exhibits the heatmap for a test image from the normal cases class.



- [Download: Download high-res image \(395KB\)](#)
- [Download: Download full-size image](#)
- Figure 9. Visualization of the effect of employing the ablation-CAM technique on X-ray test images. (a) The heatmap for a test image from the pulmonary edema class; (b) The heatmap for a test image from the pleural effusion class; (c) The heatmap for a test image from the normal cases class
- Based on radiographic differences, a normal chest X-ray ([Fig. 9c](#)) shows clear lungs at which there is no buildup in the person's lungs and a physician can define the borders of the vessels very well because they appear sharp and demarcated. Moreover, the vessels in the upper lung were relatively smaller than the vessels in the lower lungs of a person with a healthy lung. Besides, the pleural cavity typically contains approximately 15 ml of pleural fluid.
- In contrast, increased hydrostatic pressure leads to pulmonary vascular congestion and cephalization of the pulmonary vasculature. This case is not yet edema because the fluid is still in the pulmonary vessels. Consequently, once the fluid leaves the pulmonary vessels and enters the interstitial space, the patient will develop interstitial pulmonary edema (actual edema). Subsequently, the fluid spills into the alveolar space in which the patient will get alveolar pulmonary edema (airspace edema). The appearance of edema was heterogeneous with interstitial and airspace edema. Hence, if a patient develops pulmonary edema, there may be two signs. First, the upper lungs are much more indistinct which means that the edema fluid has moved from the vessels to the interstitial space, and the vessels seem to be more enlarged and not well-defined. The other sign is, that the patient has interlobular septal thickening, which is manifested by Kerley B lines, which are typically less than 1 cm in length at the lung periphery and represent fluid in the interstitial space ([Fig. 9a](#)).
- On the contrary, pleural effusion is excess fluid that accumulates between two layers of the plural including the parietal pleura and visceral pleura. Because the lungs are always in motion, there must be some fluid between the two layers of the pleura to

protect them from injury by friction. Furthermore, pleural effusion is the result of any process that causes more fluid to develop than it can be absorbed (>15 ml in the pleural cavity). Typically, the area that is the first to present plural effusion is the right and left costophrenic angle. This is because the fluid is heavier than the lung and it must fall towards gravity. In the normal case ([Fig. 9c](#)), the appearance of both costophrenic angles was clear and sharp. In contrast, left-sided pleural effusion is present in [Fig. 9b](#), because the left costophrenic angle is blunt and is not visible due to the high fluid level.

- Lastly, based on the abovementioned analysis of X-rays for normal cases, pulmonary edema disease, and pleural effusion disease, it is obvious that employing the ablation-CAM technique on X-ray test images provides meaningful insight into the chest X-rays of the target medical application.
- 5. Conclusion
- There is a growing need to promote the advancement of medical image classification systems that demonstrate superior performance in diagnosing diseases within the field of pathology. Therefore, this study incorporated a deep learning model based on the EfficientNet-V1-B4 architecture with the training-based AdamW optimization method. Consequently, the developed system operated on chest X-ray, which required passing through a preprocessing stage before being fed into the training model. The preprocessing stage involves enhancing the contrast of the chest X-ray images using the CLAHE approach, resizing images to 380×380 resolution, and applying the data augmentation process.
- To carry out the classification task, a new dataset of 28,309 samples was formed by combining several publicly available datasets. This dataset comprised three patterns: pleural effusion, pulmonary edema, and normal cases. Further, the dataset was divided into 85% samples for training the model and 15% samples for testing the model. The results show that the developed system achieved a classification rate of approximately 0.983. In addition, the achieved AUC was 1.00 for pulmonary edema and normal cases, and the obtained AUC for pleural effusion disease was approximately 0.99. Additionally, the categorization system utilizes ablation-CAM which provides meaningful insight into the chest X-rays of the target medical application.
- In summary, early and accurate detection of pulmonary conditions such as edema and effusion can significantly influence patient outcomes. This study has the potential to revolutionize the detection of pulmonary edema and pleural effusion, leading to improvements in patient care, healthcare efficiency, and accessibility of advanced diagnostic tools. In line with this, the study may contribute to reducing the workload of radiologists and healthcare providers. Automating the initial screening and diagnosis process can allow specialists to focus on more complex cases and patient care, thereby enhancing the overall healthcare efficiency.
- Future work should focus on further validating the suitability of the model under consideration in this research to identify other diagnoses using larger and more diverse datasets. Further research can be conducted using the EfficientNet-V2 model and examining its performance on smaller X-ray image sizes to reduce memory usage for the image classification problem under investigation.
- 1. Introduction

- Detecting pulmonary edema and pleural effusion using chest X-rays is crucial for the diagnosis of diseases [1,2]. Pulmonary edema occurs due to fluid buildup in the lungs' alveoli [3]. Conversely, pleural effusion is a disorder indicated by the abnormal fluid buildup in the membranes surrounding the lungs [4]. Fig. 1a depicts pulmonary edema [5] and Fig. 1b shows pleural effusion [6].
-
- Download: Download high-res image (634KB)
- Download: Download full-size image
- Figure 1. (a) Pulmonary edema (Reprinted from reference [5]); (b) Pleural effusion (Reprinted from reference [6])
- In this context, it is crucial to classify whether the fluid is located inside the lung tissue and air sacs (pulmonary edema) or within the pleural space (pleural effusion) [7,8]. Therefore, diagnostic imaging techniques, such as X-rays, are paramount in identifying the presence and extent of these medical conditions, enabling healthcare practitioners to make timely and precise diagnoses [9]. Overall, the complexity in detecting pulmonary edema and pleural effusion underscores the need for a multidisciplinary approach involving clinicians, radiologists, and other specialists to ensure accurate diagnosis and appropriate management.
- Additionally, the distinction between pulmonary edema and pleural effusion using chest X-rays will lead to identification the underlying causes of fluid accumulation in the chest. It will also help medical professionals suggest the appropriate management of these disorders and an appropriate treatment approach. For instance, detection of pulmonary edema might indicate congestive heart failure or pneumonia, necessitating specific therapeutic interventions [10]. Conversely, the detection of pleural effusion would require different treatment strategies involving drainage through thoracentesis and chest tube [11].
- Likewise, accurately classifying the location of the fluid helps in determining the precise underlying causes, ensuring that patients receive the most effective and tailored care to improve their overall health outcomes [8,12].
- Deep learning techniques have demonstrated remarkable advancements in the domain of medical image analysis, particularly in disease detection and diagnosis [13–15]. Deep Convolutional Neural Networks (CNNs) have proven exceptional capabilities in extracting intricate features from complex images, making them an ideal candidate for the detection of pulmonary edema and pleural effusion [16–18].
- EfficientNet is a family of CNNs that excel at achieving high accuracy and is computationally efficient [19]. EfficientNet was developed to scale the depth, width, and resolution of the model using a compound coefficient to optimize performance [20]. This approach has led to state-of-the-art results on the task of image classification for various applications while minimizing computational demands [21]. In particular, the EfficientNet-V1-B4 architecture is known for its exceptional efficiency in terms of the model size and computational resources. It achieves superior performance with fewer parameters compared to traditional architectures, making it well-suited for resource-constrained environments commonly encountered in medical settings. This efficiency translates to faster inference times and reduced computational costs, facilitating the real-time or near-real-time analysis of medical images for timely diagnosis and intervention. Coupled with the AdamW optimizer, which integrates the advantages of the Adam optimizer with weight decay techniques, detection algorithms can achieve superior convergence rates and model generalization. AdamW is an extension of the Adam optimizer commonly used for training neural networks [22]. It directly incorporates weight decay into its formulation improving generalization by preventing

excessive weight growth. This modification helps control model complexity and enhances training stability.

- Accordingly, by introducing EfficientNet-V1-B4 Architecture and AdamW in medical imaging analysis, healthcare professionals can expect improved diagnostic accuracy, faster processing times, and enhanced decision-making capabilities, ultimately leading to better patient outcomes and more effective treatment plans.
- The contributions of this study are as follows:
- A multi-class medical diagnosis system was developed to describe the accumulation of fluid in the lungs from perspective of image processing. Thus, the system categorizes three patterns using chest X-ray images including pleural effusion, pulmonary edema, and normal cases.
- The utilization of the EfficientNet-V1-B4 architecture associated with the AdamW optimizer in the context of pulmonary edema and pleural effusion detection from chest X-ray images represents a novel application and exploration of deep learning models for medical image analysis.
- The localization of pleural effusion and pulmonary edema diseases is accomplished by utilizing the ablation-CAM technique and is graphically presented using heatmap data visualization.
- By automating this classification process, medical professionals can save valuable time by achieving early diagnosis while ensuring more accurate diagnoses. The remainder of this paper is organized as follows. The related work is presented in Section 2. Section 3 describes the research methodology. The empirical results are analyzed and discussed in Section 4. The conclusions of this research and future work are presented in Section 5.
- 2. Related Work
- Fluid accumulation in the lungs is a life-threatening medical emergency that requires timely diagnosis and intervention and is known as pulmonary edema. Traditional methods for detecting pulmonary edema in medical imaging have limitations, leading to the demand for more accurate and efficient approaches. The promising results of artificial intelligence in various medical fields, including the detection of pulmonary edema, have encouraged the development of advanced methodologies. One major challenge hindering the advancement of CNNs in medical image analysis is the necessity of constructing ground-truth data based on specialists' opinions.
- Deep CNNs have been applied in research [23–27] to classify different types of radiographs, such as X-rays, CT scans, and ultrasounds. CNNs are used to diagnose various diseases, such as pulmonary edema, pulmonary effusion, pneumonia, COVID-19, and pneumothorax. Despite demonstrating promise for radiographic interpretation, these early studies generally lacked the level of specificity and granularity required for practical diagnostic utility.
- Based on the expansion of using Artificial Intelligence (AI) in detecting diseases, Wang et al. [28] compared several deep learning techniques for diagnosing pulmonary edema and estimating the severity of the case, and the dataset used was MIMIC-CXR for images and reports [29]. According to previous studies [30,31], there are approximately 77% accuracy among radiologists and 59% accuracy among ED physicians. Edema severity was classified in 3058 cases as mild, 1414 moderate cases, and severe in 296 cases.
- 2.1. Related Studies on CNN-Based Detection of Pulmonary Edema
- Serte et al. [18] studied pulmonary edema disease as a result of heart failure depending on chest radiographs. Researchers constructed a dataset of 27,748 front-chest radiographs over nearly six years. The collected images were in the range of 1.4–4.7 k in height and width with 80% training set, 10% validation, and a test group of 10%. Training was carried out in two

stages (pipelines) to train a branched CNN based on ResNet152v2 architecture. The goal is to cooperatively predict B-type Natriuretic Peptide (BNP) or BNPP (BNP precursor) cases. With a preset learning rate of 1e-5 and a patch size of 16, Adam's optimizer was used to train all CNNs. The region of attention was determined using a heatmap. Another factor that is considered is the blur sensitivity. Consequently, the trained models attained an AUC of 0.801 for the detection of pulmonary edema.

- In [32], a 2.5D CNN model was developed to detect multiple diseases, such as: atelectasis, pneumonia, edema, and nodules. The study investigated 5000 CT images that contained 156 edema cases, 225 pneumonia cases, and other cases. The research split the image set for each disease into training, validation, and test sets. The model achieved accuracies of 0.963, 0.818, 0.878, and 0.784, for edema, atelectasis, pneumonia, and nodule, respectively. Moreover, AUC of 0.940, 0.891, 0.869, and 0.784 were obtained for categorizing edema, atelectasis, pneumonia, and nodule diseases, respectively.
- In [33], a 2.5D CNN model was developed to detect multiple diseases, that are: atelectasis, pneumonia, edema, and nodules. The study investigated 5000 CT images that contained 156 edema cases, 225 pneumonia cases, and other cases. The research split the image set for each disease into training, validation, and test sets. As a result, the model achieved an accuracy of 0.963, 0.818, 0.878, and 0.784, for edema, atelectasis, pneumonia, and nodule, respectively. Moreover, The AUC of 0.940, 0.891, 0.869, and 0.784 were attained for categorizing edema, atelectasis, pneumonia, and nodule diseases, respectively. As shown in Table 1, a summary of previous studies on the detection of pulmonary edema using CNN models from chest X-ray images is provided.
- Table 1. Summary of previous studies on the detection of pulmonary edema using CNN models from chest X-ray images
- Study Architecture Performance
- Serte et al. [18]
- ResNet152v2-CNN AUC = 0.801
- Hayat [32]
- DesneNet-CNN AUC = 0.714
- Geng et al. [33]
- 2.5D-CNN ACC = 0.963
- AUC = 0.940
- 2.2. Related Studies on CNN-Based Detection of Pleural Effusion
- Previous studies in the domain of pleural effusion detection have explored various approaches and architectures to improve the accuracy and efficiency of diagnostic systems. With the aim of automating Lung Ultrasound (LUS) image evaluation for pleural effusion detection, Hammon et al. [30] employed a deep-learning model that was constructed based on the Regularized Spatial Transformer Network (Reg-STN) architecture to perform binary classification of pleural effusion in clinical LUS imaging. The dataset, obtained from the Royal Melbourne Hospital, consisted of 623 videos containing 99,209 2D LUS images obtained from examinations of 70 patients using a phased array transducer. This model was trained using weakly supervised and supervised methodologies utilizing a video-based labeling approach, resulting in an accuracy of 91.1%, and a frame-based labeling approach, resulting in an accuracy of 92.4%. Notably, the reference was proficient clinicians who assessed the interpretation of images.
- Researchers in [34] applied a deep learning model based on the ResNet18 architecture to the chest radiography images. The model was applied to identify pleural effusion arising from three types of respiratory disorders, namely tuberculosis, COVID-19, and pneumonia. Hence,

the developed system can detect these three diseases once they occur at an early stage before evolving into pleural effusion. Three experiments were conducted for binary classification. Consequently, the performance in terms of accuracy for early detection of pleural effusion disease from tuberculosis, COVID-19, and pneumonia was 99%, 100%, and 75%, respectively. In contrast, a multiclass experiment was applied, which included the following categories: tuberculosis, COVID-19, pleural effusion, bacterial pneumonia, and viral pneumonia. Thus, the best result was obtained for bacterial pneumonia detection, with an accuracy of 83% and an AUC of 81%. Furthermore, the multiclass system detected pleural effusion with an accuracy of 82% and AUC of 77%.

- In a study by Bar et al. [35], the identification of various pathologies, such as right pleural effusion, from chest radiographs was investigated. Their analysis utilized a CNN trained on non-medical data, achieving an AUC of 0.95. Lakhani et al. [36] explored deep-learning approaches for tuberculosis detection on chest radiographs containing pleural effusion, miliary patterns, and cavitation, and achieved an impressive AUC of 0.99. As shown in Table 2, a summary of previous studies on the detection of pleural effusion using CNN models from chest X-ray images is provided.
- Table 2. Summary of previous studies on the detection of pleural effusion using CNN models from chest X-ray images
- Study Architecture Performance
- Serte et al. [34]
- ResNet18-CNN ACC = 0.82
- AUC = 0.77
- Bar et al. [35]
- CNN + classical features AUC = 0.95
- Lakhani et al. [36]
- DCNNs (AlexNet and GoogLeNet) AUC = 0.99
- 3. Material and Methodology
- As essential as it is in practice, this study developed an AI system to detect fluid buildup in the lungs by categorizing three patterns using chest X-ray images including pleural effusion disease, pulmonary edema disease, and normal cases as illustrated in Fig. 2. The proposed computer vision-based medical classification system encompassed various stages including Data Preprocessing, Build and Training Model (learning), and Model Output (testing). Fig. 2 illustrates the research methodology. From this perspective, chest X-ray images will pass through a preprocessing stage before being fed into the training model. Furthermore, the output of the system includes class activation mapping and the category to which each test image belongs.
- Download: Download high-res image (157KB)
- Download: Download full-size image
- Figure 2. The research methodology
- 3.1. Datasets
- With the aim of conducting a classification task to reveal the presence or absence of pleural effusion and pulmonary edema disorders in the lungs using X-ray images, a new dataset of 28,309 samples was formed by combining several public datasets, including ChestX-ray14 [37], PadChest [38], and CheXpert [39]. The new dataset under consideration was distributed among three classes as follows: approximately 10,287 samples depicting pleural effusion, about 6022 samples representing pulmonary edema, and 12,000 samples exhibiting normal cases.

- 3.2. Data Preprocessing
- During this stage, a stratified split of the medical image dataset was conducted, with 85% allocated to the training set and 15% to the test set. Thus, the training and test sets are independent. This stratification was aimed at maintaining a consistent distribution of classes across both the training and test sets. Particularly, pixel normalization was excluded from the preprocessing steps, as empirical evidence suggests its unnecessary approach in certain medical image classification tasks [40].
- To achieve the computer vision classification goal, the image data should be handled properly before reaching the input layer of the model. For the application at hand, a dedicated pipeline was employed on the image data by conducting three sequential steps, as illustrated in Fig. 3. First, enhancing the contrast of the chest X-ray images was enhanced using the CLAHE approach. Second, all images were resized to 380×380 pixels. Lastly, multiple data augmentation techniques were employed.
-
- Download: Download high-res image (41KB)
- Download: Download full-size image
- Figure 3. Preprocessing steps
- 3.2.1. CLAHE Technique
- The CLAHE technique has been used in various image processing applications because of its capability to enhance image contrast by partitioning the image into small blocks and equalizing the histogram of each block. This method also mitigates contrast amplification within each block, thus minimizing noise amplification [41]. It serves to improve image contrast, facilitates better visibility and interpretation, and is adept at enhancing image details [42]. Fig. 4a shows the original X-ray image selected from the data under consideration. Conversely, Fig. 4b illustrates the enhanced X-ray image after employing the CLAHE technique, which demonstrates the contrast improvement compared to the original X-ray image proving the effectiveness of applying CLAHE in rendering certain lung details more discriminant.
-
- Download: Download high-res image (195KB)
- Download: Download full-size image
- Figure 4. (a) The original X-ray image; (b) The enhanced X-ray image after employing CLAHE
- 3.2.2. Resize
- Determining the image size for training CNN is important when considering the trade-offs between accuracy, speed, and memory requirements [43]. Larger image sizes typically exhibit better accuracy, but they also require more computation and memory [44]. Additionally, the benefits of using larger images tend to diminish as the size increases [45].
- CNNs frequently downsample the dimensions of an input image, resulting in an irregular final size [46]. To avoid this, it is advisable to employ a square image size during the training phase [47]. In our approach, we resized all images to 380×380 pixels, maintaining the original aspect ratio and implementing zero-padding as needed.
- 3.2.3. Data Augmentation
- To improve the performance of the deep learning model and promote its capacity for generalization, a data-augmentation approach was employed. Data augmentation involves integrating subtly modified versions of current data or generating synthetic data based on existing samples, thereby expanding the effective dataset size. For this purpose, a total of six augmentation methods were adopted, including: CutMix [48], MixUp [49], CenterCrop,

RandomChannelShift [50], RandomGaussianBlur [51], and Random Brightness [50] transformations during the training process, aiming to improve the robustness of the model.

- 3.3. Build and Training Model
- Attaining superior performance for image categorization necessitates not only creating a superb architecture but also selecting an appropriate optimizer that can significantly minimize the loss function. Thus, this study presents a deep learning model that was constructed based on the EfficientNet-V1-B4 architecture along with the AdamW optimizer that was utilized for training this model.
- 3.3.1. EfficientNet-V1-B4 Architecture
- The EfficientNet-V1 architecture was introduced by Tan and Le in 2019 [20] in which a novel compound scaling approach was proposed. In this view, the EfficientNet-V1 model uses R to uniformly scale all the dimensions of the network including the width, depth, and resolution. Thus, the scaling method of the model is mathematically described as follows [20]:
$$\text{depth} = \alpha R, (1) \text{width} = \beta R, \text{and resolution} = \gamma R s.t. \alpha \cdot \beta^2 \cdot \gamma^2 \approx 2, \alpha \geq 1, \beta \geq 1, \gamma \geq 1$$
where the coefficients α, β, γ are constant, and they are specified by a small grid search, whereas the value of (R) is determined by the user depending on the available resources to scale the model. As illustrated in Eq. (1), the Floating-Point Operations (FLOPs) of the ordinary convolution operation are typically proportional to $\alpha \cdot \beta^2 \cdot \gamma^2$. Considering the restriction of $\alpha \cdot \beta^2 \cdot \gamma^2 \approx 2$, such that for each change in the value of R, the overall FLOPs roughly increase by $2R$.
- Therefore, it can be straightforward to increase the dimensions of the network by (R) if there is a need to use $2R$ times more computational resources. Hence, utilizing the abovementioned compound scaling strategy has an intuitive implication if there is a larger input image that requires additional layers in the network to expand its receptive area and additional channels to obtain more fine-grained patterns. Hence, scaling the network dimensions leads to a systematic increase in the performance of the model.
- Furthermore, there are eight variations of EfficientNet-V1, referred to as EfficientNet-V1-B0 through EfficientNet-V1-B7. This study employs EfficientNet-V1-B4. Fig. 5 depicts the details of the EfficientNet-V1-B4 architecture considered in this study. The architecture of EfficientNet-V1-B4 is segmented into seven blocks, called Mobile Inverted Bottleneck Convolution (MBConv), which are the elementary building blocks of EfficientNet-V1-B4, followed by a fully connected layer. For a particular stage(s) within this architecture, the block appears as MBConvX×L, where the notation X = 1 and X = 6 indicate the block type signify the standard Swish activation function, and (L^s) denotes the number of layers. The kernel size associated with the MBConvX block also appears under the block type.
-
- Download: Download high-res image (237KB)
- Download: Download full-size image
- Figure 5. The EfficientNet-V1-B4 architecture
- Lastly, the input resolution ($H^s \times W^s$), and the number of output channels (C^s), is depicted as $(H^s \times W^s \times C^s)$, respectively. For example, in the second stage of the architecture where ($S = 2$), the $\text{MBConv1} \times 2$ notation indicates that the MBConv1 block is repeated twice ($L=2$), the kernel size is ($k3 \times 3$), and the notation ($190 \times 190 \times 24$) implies the input resolution which is (190×190), and the number of channels is (24).
- In this study, the optimal performance was pursued by fine-tuning the pre-trained weights of EfficientNet-V1-B4 using Noisy Student data. Subsequently, a fully connected layer with three neurons was used to represent the class scores (i.e., the output layer).

- Furthermore, the MBConvX blocks utilize the Swish activation function and squeeze-and-excitation (SE) optimization which enables the efficient extraction of high-quality features, and minimize computational complexity while maximizing accuracy. Additionally, MBConv's lightweight design extracts informative features from early stages, while SE dynamically refines them, resulting in sharper detections and improved accuracy compared to traditional Convolutional Neural Networks. Fig. 6a illustrates MBConv1, while Fig. 6b presents MBConv6, both representing distinct design points in the EfficientNet-V1-B4 architecture. MBConv1 emphasizes early feature extraction with minimal computational cost, making it particularly well-suited for the initial stages of the network. By contrast, MBConv6 concentrates on advanced feature refinement, achieving heightened accuracy although with a modest increase in complexity. The deliberate utilization of MBConvX variants in this manner enables EfficientNet-V1-B4 to achieve a balance between efficiency and accuracy.
-
- Download: Download high-res image (262KB)
- Download: Download full-size image
- Figure 6. The MBConv blocks in the EfficientNet-V1-B4 architecture. (a) MBConv1; (b) MBConv6
- 3.3.2. AdamW Optimizer
- An AdamW optimizer was used to train the model. The AdamW optimizer is an extension of the Adam optimizer with the addition of a weight decay regularization approach [22]. Furthermore, weight decay serves as a method to mitigate overfitting by imposing penalties on substantial weights.
- Accordingly, the Adam optimizer exhibited comparatively reduced efficiency in weight regularization when compared to alternative optimizers, such as SGD with momentum. However, AdamW disentangles the weight decay from the adaptive estimation of the first and second moments of the gradients. This decoupling empowers AdamW to enhance the weight regularization more efficiently without compromising the speed of convergence.
- 4. Model Outputs
- In this section, the experimental settings, and results for the dataset under consideration are illustrated. The performance of the classification model was evaluated based on complexity and different metrics including accuracy (A), precision (P), recall (R), and F1-score. Finally, Ablation-based Class Activation Mapping (Ablation CAM) was employed to provide meaningful and interpretable explanations of the results.
- 4.1. Experiments Setting
- In this study, TPU 3-8 was utilized to train the network. Subsequently, the training and testing phases occurred within the same environment, employing the Keras deep learning framework and Python 3.8 as the programming language. Network training involved the utilization of the hyperparameters outlined in Table 3.
- Table 3. Hyperparameters
- Parameter Value
- Input size $380 \times 380 \times 3$
- Batch size 256
- Learning rate $1e-4$
- Optimizer AdamW
- Epochs 70
- Loss function Categorical crossentropy
- 4.2. Computational Complexity

- The computational complexity of a CNN is an important consideration for its practical deployment and can be analyzed along two dimensions which are spatial and temporal [52]. The spatial complexity (SC) indicates the storage requirements (i.e., disk space) of a trained CNN model, including both its parameters and intermediate feature maps. The temporal complexity (TC) reflects the computational cost, commonly measured in floating-point operations per second (FLOPS), required for the CNN to make predictions. For the proposed CNN model evaluated in this study, we obtained SC of 243 MB and TC of 4.51 GigaFLOPS. These values can be used to assess the resource requirements and inference speed of a model in real-world applications.
- 4.3. Classification Performance Evaluation
- The performance evaluation of the proposed model on the test set relies on the utilization of a confusion matrix. The accurate determination of this matrix requires knowledge of the true values associated with the validation data. As illustrated in Fig. 7, the confusion matrix was implemented to evaluate the performance of the model. In this view, multiple measures were computed including P, R, A, and F-1, utilizing the predetermined methods described in previous research [53]. The formulations for these evaluation measures are detailed in Eqs. (2) through (5).
 - Download: Download high-res image (149KB)
 - Download: Download full-size image
 - Figure 7. The confusion matrix for chest X-ray images
 - $(2)P=TPTP+FP$
 - $(3)R=TPTP+Fn$
 - $(4)A=TP+TNTP+TN+FP+FN$
 - $(5)F1=2\cdot PRP+R$
- Specifically, the TP represents True Positives, denoting correctly identified positive instances. TN represents True Negatives, signifying correctly identified negative instances. FP represents False Positives, indicating instances incorrectly identified as positives. FN represents False Negatives, representing instances incorrectly identified as negatives.
- The results of the calculation of the aforementioned matrices are presented in Table 4, which shows that the developed system classifies pleural effusion, pulmonary edema, and normal patterns with a high classification rate compared with previous studies as shown in Tables 1 and 2. According to this viewpoint, the average achieved accuracy was approximately 0.983, the average accomplished precision was approximately 0.987, the attained average recall value was roughly 0.983, and the average F-1 was score approximately 0.987. These findings confirm that the classification system is precise and robust in identifying pleural effusion and pulmonary edema disorders using X-ray images.
- Table 4. The classification report of our proposed approach to X-ray images
- Classes Precision Recall F1-score Accuracy
- Edema 0.99 0.98 0.98 0.98
- Effusion 0.98 0.98 0.99 0.98
- Normal 0.99 0.99 0.99 0.99
- Average 0.987 0.983 0.987 0.983
- Finally, we confirmed a comprehensive evaluation of the model's performance across various sensitivity and specificity thresholds. The ROC curve tool was used specifically to analyze three medical classes: pulmonary edema, pleural effusion, and normal cases using the dataset of X-ray images under consideration in this study, as represented in Fig. 8. The results revealed that the AUC was 1.00 for pulmonary edema and normal cases. Additionally, the AUC was 0.99 for pleural effusion disease. These ROC evaluations confirmed the robustness of the developed categorization system that differentiated between pulmonary edema,

pleural effusion, and normal cases, thus providing valuable insights into its diagnostic capabilities.

-
- Download: Download high-res image (84KB)
- Download: Download full-size image
- Figure 8. ROC curves for pulmonary edema, pleural effusion, and normal cases using chest X-rays
- This work proves the effectiveness of the proposed neural network architecture combined with the AdamW optimizer for the detection of Pulmonary Edema and Pleural Effusion diseases. The results were compared with well-known classification architectures such as VGG19, DenseNet121, InceptionV3, EfficientNet, and ResNet101. Hence, the average accuracy of these architecture models was assessed using various training-based optimizers including SGD, Adagrad, RMSprop, Adam, Radam, and AdamW. Table 5 compares the aforementioned optimizers and architectures. As a result, the proposed model achieved the highest average accuracy of 0.983 when employing the AdamW optimizer across EfficientNet-V1-B4 compared to the others utilizing the same datasets applied in this study.
- Table 5. Comparison of various optimizers applied to renowned architectures in terms of average accuracy on the datasets used in this study
- | Model | SGD | Adagrad | RMSprop | Adam | Radam | AdamW |
|-------------------|-------|---------|---------|-------|-------|-------|
| VGG19 | 0.820 | 0.814 | 0.81 | 0.822 | 0.825 | 0.83 |
| DenseNet121 | 0.850 | 0.832 | 0.844 | 0.858 | 0.861 | 0.864 |
| InceptionV3 | 0.832 | 0.834 | 0.830 | 0.845 | 0.847 | 0.85 |
| ResNet101 | 0.871 | 0.870 | 0.871 | 0.879 | 0.883 | 0.881 |
| EfficientNetV1-B0 | | 0.932 | 0.924 | 0.92 | 0.948 | 0.95 |
| EfficientNetV1-B1 | | 0.935 | 0.927 | 0.921 | 0.95 | 0.951 |
| EfficientNetV1-B2 | | 0.945 | 0.935 | 0.933 | 0.955 | 0.966 |
| EfficientNetV1-B3 | | 0.951 | 0.947 | 0.949 | 0.967 | 0.968 |
| EfficientNetV1-B4 | | 0.961 | 0.953 | 0.959 | 0.975 | 0.979 |
| EfficientNetV1-B5 | | 0.961 | 0.951 | 0.96 | 0.97 | 0.973 |
| EfficientNetV1-B6 | | 0.961 | 0.952 | 0.962 | 0.972 | 0.975 |
| EfficientNetV1-B7 | | 0.962 | 0.955 | 0.964 | 0.971 | 0.976 |
| EfficientNetV1-L2 | | 0.962 | 0.957 | 0.964 | 0.974 | 0.976 |
| EfficientNetV2-B0 | | 0.928 | 0.923 | 0.92 | 0.941 | 0.947 |
| EfficientNetV2-B1 | | 0.93 | 0.925 | 0.922 | 0.943 | 0.950 |
| EfficientNetV2-B2 | | 0.935 | 0.928 | 0.925 | 0.948 | 0.953 |
| EfficientNetV2-B3 | | 0.943 | 0.938 | 0.935 | 0.952 | 0.956 |
| EfficientNetV2T | 0.953 | 0.95 | 0.946 | 0.957 | 0.958 | 0.961 |
| EfficientNetV2_GC | | 0.957 | 0.963 | 0.958 | 0.976 | 0.978 |
| EfficientNetV2S | 0.96 | 0.957 | 0.951 | 0.976 | 0.978 | 0.979 |
| EfficientNetV2M | | 0.963 | 0.96 | 0.956 | 0.979 | 0.979 |
| EfficientNetV2L | 0.969 | 0.966 | 0.96 | 0.976 | 0.974 | 0.979 |
| EfficientNetV2XL | | 0.968 | 0.964 | 0.96 | 0.978 | 0.980 |
- 4.4. Localization Using Ablation-CAM
- In the context of medical image classification using deep learning, it is imperative to enhance the interpretability and significance of the results. Ablation-CAM emerged as a gradient-free methodology designed to provide visual explanations for models based on deep CNNs [54]. This technique operates by selectively ablating (removing) individual units within feature maps and measuring the subsequent drop in the activation score for the target class. The

significance of each feature map unit was then quantified as the proportion of decrease in the activation score.

- To generate the ablation-CAM map, feature map units are weighted based on their calculated importance and superimposed onto the original image. The outcome is a coarse localization map that accentuates the pivotal regions in the image, thereby influencing the model's concept predictions.
- Notably, ablation-CAM exhibits superiority over the state-of-the-art Grad-CAM technique across diverse image classification tasks [55]. Because ablation-CAM is more resilient to local irregularities and saturations within the neural network, it is considered an effective and robust approach to visual interpretation. To utilize this functionality, ablation-CAM was applied after the prediction of the class label by the developed classification system. Further, we visualized the effect of employing the ablation-CAM technique on X-ray test images. Fig. 9a shows the heatmap for a test image from the pulmonary edema class; Fig. 9b depicts the heatmap for a test image from the pleural effusion class; and Fig. 9c exhibits the heatmap for a test image from the normal cases class.
-
- Download: Download high-res image (395KB)
- Download: Download full-size image
- Figure 9. Visualization of the effect of employing the ablation-CAM technique on X-ray test images. (a) The heatmap for a test image from the pulmonary edema class; (b) The heatmap for a test image from the pleural effusion class; (c) The heatmap for a test image from the normal cases class
- Based on radiographic differences, a normal chest X-ray (Fig. 9c) shows clear lungs at which there is no buildup in the person's lungs and a physician can define the borders of the vessels very well because they appear sharp and demarcated. Moreover, the vessels in the upper lung were relatively smaller than the vessels in the lower lungs of a person with a healthy lung. Besides, the pleural cavity typically contains approximately 15 ml of pleural fluid.
- In contrast, increased hydrostatic pressure leads to pulmonary vascular congestion and cephalization of the pulmonary vasculature. This case is not yet edema because the fluid is still in the pulmonary vessels. Consequently, once the fluid leaves the pulmonary vessels and enters the interstitial space, the patient will develop interstitial pulmonary edema (actual edema). Subsequently, the fluid spills into the alveolar space in which the patient will get alveolar pulmonary edema (airspace edema). The appearance of edema was heterogeneous with interstitial and airspace edema. Hence, if a patient develops pulmonary edema, there may be two signs. First, the upper lungs are much more indistinct which means that the edema fluid has moved from the vessels to the interstitial space, and the vessels seem to be more enlarged and not well-defined. The other sign is, that the patient has interlobular septal thickening, which is manifested by Kerley B lines, which are typically less than 1 cm in length at the lung periphery and represent fluid in the interstitial space (Fig. 9a).
- On the contrary, pleural effusion is excess fluid that accumulates between two layers of the plural including the parietal pleura and visceral pleura. Because the lungs are always in motion, there must be some fluid between the two layers of the pleura to protect them from injury by friction. Furthermore, pleural effusion is the result of any process that causes more fluid to develop than it can be absorbed (>15 ml in the pleural cavity). Typically, the area that is the first to present plural effusion is the right and left costophrenic angle. This is because the fluid is heavier than the lung and it must fall towards gravity. In the normal case (Fig. 9c), the appearance of both costophrenic angles was clear and sharp. In contrast, left-sided

pleural effusion is present in Fig. 9b, because the left costophrenic angle is blunt and is not visible due to the high fluid level.

- Lastly, based on the abovementioned analysis of X-rays for normal cases, pulmonary edema disease, and pleural effusion disease, it is obvious that employing the ablation-CAM technique on X-ray test images provides meaningful insight into the chest X-rays of the target medical application.
- 5. Conclusion
- There is a growing need to promote the advancement of medical image classification systems that demonstrate superior performance in diagnosing diseases within the field of pathology. Therefore, this study incorporated a deep learning model based on the EfficientNet-V1-B4 architecture with the training-based AdamW optimization method. Consequently, the developed system operated on chest X-ray, which required passing through a preprocessing stage before being fed into the training model. The preprocessing stage involves enhancing the contrast of the chest X-ray images using the CLAHE approach, resizing images to 380×380 resolution, and applying the data augmentation process.
- To carry out the classification task, a new dataset of 28,309 samples was formed by combining several publicly available datasets. This dataset comprised three patterns: pleural effusion, pulmonary edema, and normal cases. Further, the dataset was divided into 85% samples for training the model and 15% samples for testing the model. The results show that the developed system achieved a classification rate of approximately 0.983. In addition, the achieved AUC was 1.00 for pulmonary edema and normal cases, and the obtained AUC for pleural effusion disease was approximately 0.99. Additionally, the categorization system utilizes ablation-CAM which provides meaningful insight into the chest X-rays of the target medical application.
- In summary, early and accurate detection of pulmonary conditions such as edema and effusion can significantly influence patient outcomes. This study has the potential to revolutionize the detection of pulmonary edema and pleural effusion, leading to improvements in patient care, healthcare efficiency, and accessibility of advanced diagnostic tools. In line with this, the study may contribute to reducing the workload of radiologists and healthcare providers. Automating the initial screening and diagnosis process can allow specialists to focus on more complex cases and patient care, thereby enhancing the overall healthcare efficiency.
- Future work should focus on further validating the suitability of the model under consideration in this research to identify other diagnoses using larger and more diverse datasets. Further research can be conducted using the EfficientNet-V2 model and examining its performance on smaller X-ray image sizes to reduce memory usage for the image classification problem under investigation.

Discussion

Blunt chest injury following cardiopulmonary arrest is associated with several iatrogenic complications including sternal fractures, rib fractures, pneumothoraces, and pleural effusions. Point-of-Care Ultrasound (POCUS) is a well-established clinical tool for assessment of these cardiopulmonary clinical presentations and can be utilized in the Emergency Department (ED) for efficient assessment of cardiac function, evaluation of thoracic trauma, and identification of pneumonic fluid collections.

Visual case discussion

An 82-year-old female with a history of advanced pancreatic adenocarcinoma and recent PEA cardiac arrest presented to the ED via EMS from her oncologist's office for left-sided stabbing chest pain radiating to her back. Symptoms were exacerbated by movement and coughing. During her arrest twelve days prior, the patient underwent resuscitation including CPR with LUCAS Device resulting in blunt chest injury. After ROSC she was hospitalized for one week and discharged just days before this ED

Question 1

The plankton sign in ultrasonography refers to:

Answer Options

a)

Movement of the diaphragm with respiration.

b)

Rising and falling movement of collapsed lung in pleural effusion.

c)

Floating cellular material within pleural fluid.

Correct Answer = c

Explanation:

There are several dynamic signs that confirm the presence of pleural effusion/fluid including visualizing movement of the diaphragm and “jellyfish sign” (answer b). Plankton sign specifically refers to the small echoic particles that may be

A 28-year-old woman presented to the outpatient setting with right-sided intermittent chest pain for the past 8 months. For the past 3 months, she noticed breathlessness initially on exertion, which had progressed to dyspnea at rest. She also reported intermittent cramping abdominal pain, predominantly in the pelvis, that worsened during each menstrual cycle. She had regular menses and denied the use of any hormonal-based or barrier methods of contraception. She had never smoked. She was married and delivered a child 10 years ago. Two years before this presentation, she had undergone medical termination of pregnancy. A previous Pap smear of the cervix was normal. She denied any history of cough, hemoptysis, vomiting, diarrhea or hematemesis, dyspareunia, or post-coital bleeding. There was no relevant family history. Physical Examination Findings

The patient was conscious and well oriented at presentation and had mild respiratory distress from using accessory muscles. Her vitals were as follows: heart rate of 104 beats/min, BP of 106/80 mm Hg, respiratory rate of 30 breaths/min, and oxygen saturation of 97% on ambient air. A physical examination of the chest showed reduced tactile fremitus, dull percussion notes, and reduced intensity breath sounds on the right side. Palpation of the abdomen revealed minimal tenderness in the suprapubic area. Examination of the cardiovascular and central nervous systems was normal. Pelvic examination showed the uterus was anteverted with restricted mobility. The bilateral adnexa were free, and a nodular, nontender lesion approximately 2 x 2 cm was palpable posteriorly in the pouch of Douglas.

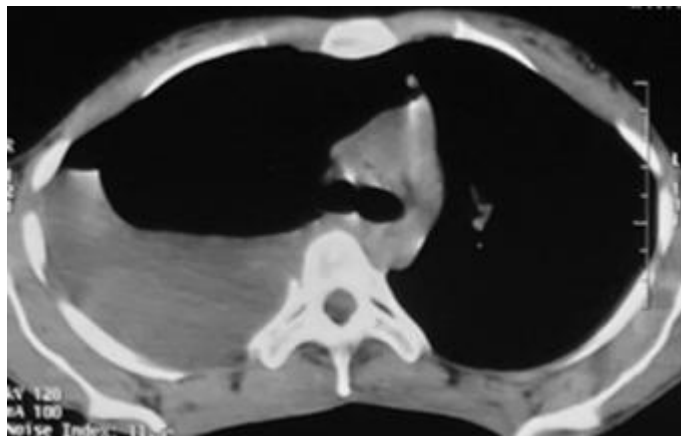
Diagnostic Studies

Initial laboratory investigation revealed a hemoglobin level of 10 g/dL, a WBC count of $10.8 \times 10^9/L$ (differential levels are as follows: neutrophils 56%, lymphocytes 36%, eosinophils 4%, monocytes 4%), and a platelet count of $661 \times 10^9/L$. Blood metabolic panel, including renal and liver parameters, was normal. Chest radiograph revealed near-complete opacification of the right hemithorax with a contralateral shift of the heart, indicating a massive pleural effusion ([Fig 1](#)). A CT scan of the chest showed only pleural effusion without any pleural thickening or nodules ([Fig 2](#)). Transvaginal ultrasonography revealed a right ovarian cystic lesion of size $2.4 \times 2 \text{ cm}^2$, no findings on the left ovary, and a relatively well-defined hyperechoic lesion measuring $1.7 \times 2.3 \text{ cm}^2$ in the pouch of Douglas with minimal ascites in the pelvis. A MRI scan of the abdomen corroborated the ultrasound findings. Thoracentesis revealed hemorrhagic fluid, an exudate with a low adenosine deaminase level. Pleural fluid cytology was negative for malignant cells ([Table 1](#)). A flexible bronchoscopy excluded an endobronchial lesion. Given the undiagnosed pleural effusion, a medical thoracoscopy was performed, which revealed yellow to dark brown nodules measuring between 2 and 3 cm over the posterior parietal pleura and on the surface of the diaphragm ([Fig 3](#)). Thoracoscopic biopsy demonstrated hemosiderin-laden macrophages, tiny areas of endometrial stroma, and a focal collection of foamy histiocytes and foreign body giant cells ([Fig 4](#)). Immunohistochemistry showed positive staining for CD10 ([Fig 5](#)) and estrogen receptor ([Fig 6](#)).



1. [Download: Download high-res image \(142KB\)](#)
2. [Download: Download full-size image](#)

Figure 1. Chest radiograph posteroanterior view shows an opaque right hemithorax with a contralateral shift of the mediastinum.



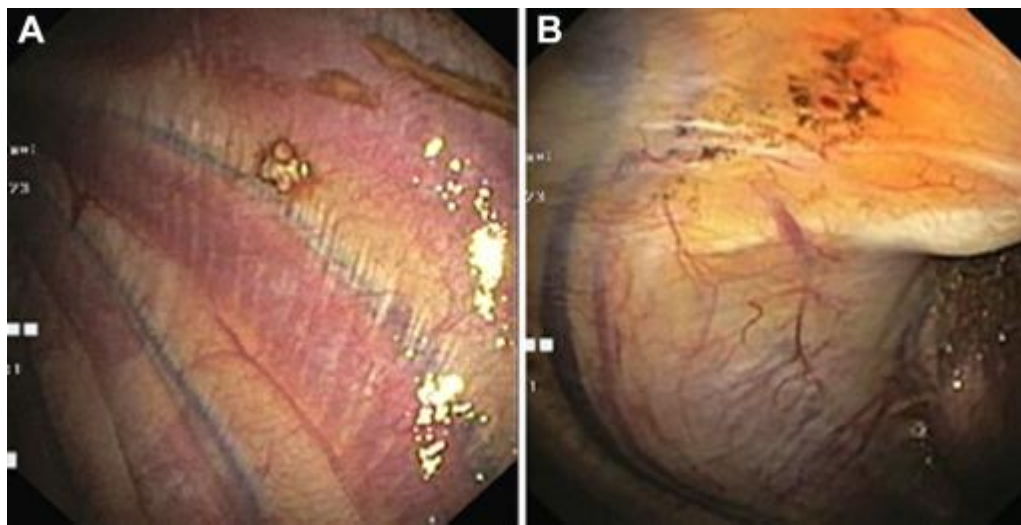
1. [Download: Download high-res image \(65KB\)](#)

2. [Download: Download full-size image](#)

Figure 2. CT scan of the chest shows a hypodense opacity on the right hemithorax.

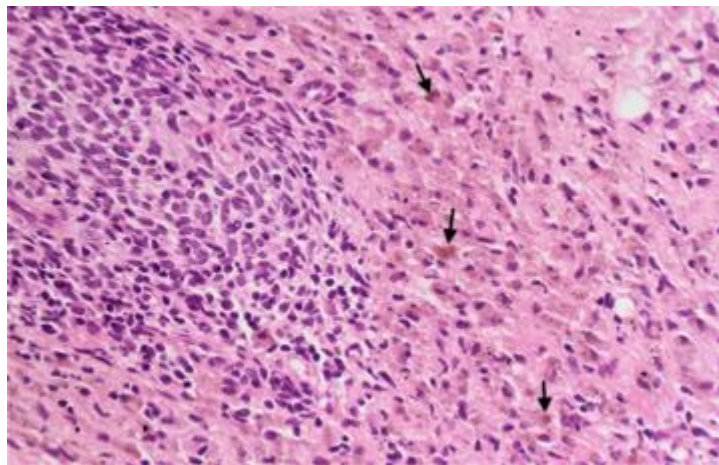
Table 1. Pleural Fluid Characteristics of the Reported Case

Characteristic	Description
Color	Hemorrhagic
Type of fluid	Exudative Total protein: 4.3 g/dL Pleural fluid protein/serum protein ratio: 0.51 Lactate dehydrogenase: 490 units/L (serum lactate dehydrogenase was 418 units/L)
Cytology	Macrophage: 80% Lymphocyte: 15% Polymorph: 5%
Malignant cells/endometrial glands	Negative
Adenosine deaminase	20.42 units/L
Glucose	62 mg/dL



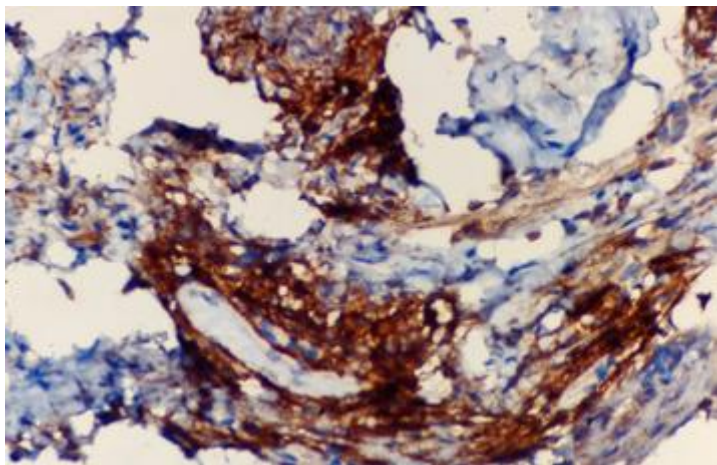
1. [Download: Download high-res image \(170KB\)](#)
2. [Download: Download full-size image](#)

Figure 3. Medical thoracoscropy reveals yellow to dark brown nodules on the parietal pleural surface.



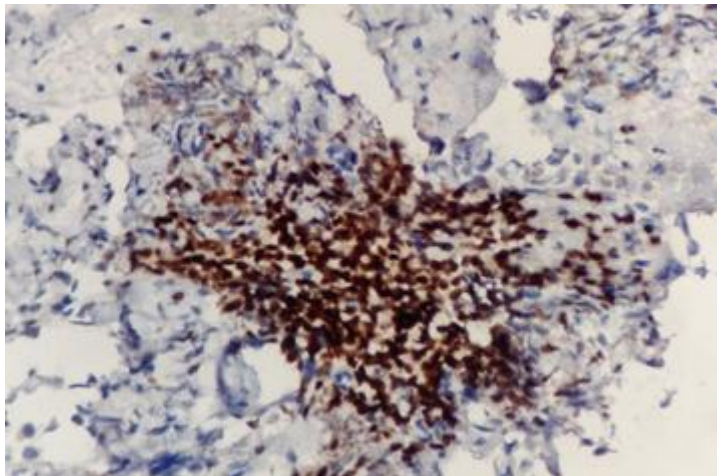
1. [Download: Download high-res image \(239KB\)](#)
2. [Download: Download full-size image](#)

Figure 4. Microscopy shows the presence of islands of spindle cells (endometrial stromal cells) with collections of hemosiderin-laden macrophages (arrows) (hematoxylin-eosin stain, original magnification $\times 400$).



1. [Download: Download high-res image \(209KB\)](#)
2. [Download: Download full-size image](#)

Figure 5. Stromal cells are positive for CD10 (immunohistochemistry, original magnification $\times 400$).



1. [Download: Download high-res image \(198KB\)](#)
2. [Download: Download full-size image](#)

Figure 6. Stromal cells are positive for estrogen receptor (immunohistochemistry, original magnification $\times 400$).

What is the diagnosis?

Diagnosis: Pleural endometriosis with endometriosis-related pleural effusion

Discussion

Endometriosis is the presence of endometrium-like tissue outside the uterus, often associated with a chronic inflammatory response. The pelvis and peritoneal cavity are the most common sites for endometriosis. An estimated 5% to 10% of women in their childbearing age develop pelvic endometriosis. They usually present with pain in the abdomen, dysmenorrhea, abnormal uterine bleeding, and infertility.

Endometriosis outside the abdominopelvic cavity is rare. The most common site of extrapelvic endometriosis is the thoracic cavity, affecting the pleura, lungs, and diaphragm. Thoracic endometriosis most commonly presents as pneumothorax followed by hemothorax, hemoptysis, and lung nodules. Most often, although not always, these symptoms develop in association with menstruation and predominantly affect the right hemithorax. Concomitant pelvic endometriosis is commonly seen.

Endometriosis-related pleural effusion is a rare manifestation of thoracic endometriosis. Most patients are young (aged < 40 years), have concomitant pelvic endometriosis, and are nulliparous. The median duration between the onset of symptoms and diagnosis of pleural effusion is usually 6 months. The most common symptom is dyspnea, followed by chest pain and abdominal pain. The symptoms coincide with menstruation in most patients. The effusion is usually unilateral and right-sided in nearly 90% of patients. More than one-half of patients present with a large effusion. Concomitant pneumothorax can be seen in one-third of patients. The pleural fluid is exudative and appears bloody in almost all patients. The pleural fluid glucose level is usually > 60 mg/dL. Limited data suggest that the adenosine deaminase level can be low or high (> 35 units/L) in equal proportions of patients.

Various theories are proposed to explain the pathophysiology of endometrial deposits in the pleural space. According to Sampson's theory of retrograde menstruation, endometrial cells travel backward through the fallopian tubes and into the peritoneal cavity. In the peritoneal cavity, there is a predictable flow of fluids and cells from the pelvis to the right subdiaphragmatic area through the right paracolic gutter while deviating away from the left hemidiaphragm due to obstruction of flow by the falciform and phrenicocolic ligaments. Afterward, the endometrial cells may get implanted in the diaphragm or migrate to the right pleural cavity through congenital defects or acquired fenestrations in the diaphragm. The preponderance of congenital defects in the right hemidiaphragm and the underlying liver exerting the piston effect may explain the preferential occurrence of endometriosis in the right hemithorax. The coelomic metaplasia theory postulates the origin of the endometrial tissue from the mesothelial cells lining the pleura, and estrogen may have a role in this metaplastic transformation. Furthermore, lymphatic and hematogenous dissemination of endometrial cells can lead to endometriosis in distant organs.

Diagnosis of endometriosis-related pleural effusion is challenging and often requires a high index of suspicion. Clinically, one may suspect endometriosis as the cause of a pleural effusion when the effusion is recurrent, right-sided, and associated with menstruation. However, definitive diagnosis requires demonstrating endometrial tissue in the fluid cytology or pleural biopsy. Pleural fluid cytology has a lower yield (9%) than pleural biopsy. The yield of pleural fluid cytology will likely improve if the pleural fluid is collected during menstruation and the cytopathologist is informed of the possibility of pleural endometriosis. A thoracoscopic biopsy is superior to a closed pleural biopsy in diagnosing pleural endometriosis. Typically, endometrial deposits in the pleura and diaphragm appear dark brown to violet, and size ranges from a few millimeters to 1 cm. Imaging modalities (eg, CT scan, MRI scan) can aid the diagnosis by excluding other diseases and delineating diaphragmatic endometrial deposits.

Histologically, the triad of endometrial glands, stroma, and hemosiderin-laden macrophages is considered diagnostic but seen infrequently in thoracic endometriosis. Furthermore, the diagnosis remains challenging when only small foci of endometrial stroma are found in lung or pleural tissue. Sometimes, it is difficult to distinguish endometrial stroma and inflammatory cells by histomorphology alone. Given these challenges, immunohistochemistry is crucial for the

diagnosis of thoracic endometriosis. Generally, estrogen receptor, progestin receptor, and CD10 immunostaining are performed to confirm endometriosis. The estrogen and progestin receptors are expressed in large proportions of endometrial stroma and endometrial gland, whereas CD10 is a marker of endometrial stroma but not endometrial gland. Therefore, a positive estrogen receptor, progestin receptor, and CD10 are required for the identification of the endometrial stroma, whereas estrogen and progestin receptor positivity are required for the identification of the endometrial gland. CD10 has a sensitivity of nearly 96% in detecting endometrial stroma. Furthermore, two staining patterns are recognized for estrogen and progestin receptors—scattered and aggregated patterns. Notably, a scattered pattern staining is also identified in many cases of resected specimens of spontaneous pneumothorax in men. Therefore, merely identifying scattered patterns of staining for estrogen and progestin receptors in women is insufficient to diagnose pleural endometriosis. In an appropriate clinical context, a positive estrogen and progestin receptor in an aggregated pattern, along with positive CD10, is essential to confirm the diagnosis of pleural endometriosis.

Management of endometriosis-related pleural effusion includes treatment with antigenadotropic agents and surgery for the risk reduction of recurrence. Antigonadotropic agents act by decreasing endogenous estrogen production, leading to atrophy of endometrial tissue. Some of the agents that are used include cyclic or continuous oral contraceptives, dienogest, danazol, cyproterone acetate, and gonadotropin-releasing hormone agonists (eg, leuprolide). To our knowledge, there is no head-to-head comparison between various agents. Usually, the treatment is continued for 6 to 24 months. Recently, dienogest has shown promising results in managing endometriosis. When taken continuously, it inhibits systemic gonadotropin secretion and has local antiproliferative and antiinflammatory effects on endometriotic lesions. Furthermore, long-term treatment with dienogest 2 mg/d is associated with significant improvements in physical, mental, social, emotional, and general health parameters in women with endometriosis. The drug has been shown to be well tolerated and has been safely administered for up to 5 years in patients with endometriosis.

Medical therapy alone is associated with a higher recurrence rate. Therefore, surgical procedures are often performed upfront or on medical treatment failure. Video-assisted thoracic surgery remains the procedure of choice in managing thoracic endometriosis. It can detect blebs, bullae, and endometrial implants on the diaphragm, lungs, and visceral and parietal pleura. Furthermore, the surgeon can perform definitive surgery in the same setting, including pleurodesis. Hysterectomy and bilateral salpingo-oophorectomy may be performed in women who do not want to have pregnancy in future.

Clinical Course

The lung remained unexpanded after a week of thoracoscopy. The chest tube was kept in situ, and negative suction was applied. Two weeks later, a complete expansion of the lung occurred, and the chest drain was removed. The patient has initiated oral dienogest 2 mg once daily and is scheduled for periodic assessment of the pleural and presumed pelvic endometriosis. She was doing well in her last follow-up 5 months after starting treatment.

Clinical Pearls

- 1.

Endometriosis-related pleural effusion is a rare manifestation of thoracic endometriosis. It usually affects young women in their reproductive years. Concomitant pelvic endometriosis is seen in most patients and is an important clue to suspect pleural endometriosis.

- 2.

Pleural effusion is usually exudative and hemorrhagic and mostly occurs on the right side. Pleural fluid cytology is usually noncontributory. The diagnosis is usually made by closed or thoracoscopic pleural biopsy.

- 3.

Treatment includes progestins and gonadotropin-releasing hormone analogs that are usually given for 1 to 2 years.

- 4.

Medical therapy is associated with a high recurrence rate. Video-assisted thoracoscopic surgery remains the modality of choice for surgical management of thoracic endometriosis.

Abstract

Necrotizing pneumonia (NP) is characterized by destruction of pulmonary tissue, resulting in multiple thin-walled cavities. There are limited reports on NP and parapneumonic effusion cases in children associated with Pseudomonas aeruginosa. Currently, there is no consensus regarding the optimal timing for video-assisted thoracoscopic surgery (VATS) following failure of chest tube placement and antibiotic treatment. A healthy 20-month-old child was hospitalized with symptoms of community-acquired pneumonia, progressing to severe NP and parapneumonic effusion. Despite receiving broad-spectrum antibiotics and chest tube placement on the third day of treatment, the condition continued to deteriorate, prompting VATS intervention on the sixth day. The presence of a “split pleural sign” and extensive lung necrosis on chest computed tomography contributed to initial treatment failure. Multidrug resistance *P. aeruginosa* was identified through nasal trachea aspiration specimens on the eighth day of treatment, leading to an adjustment in antibiotic therapy to high-dose meropenem and amikacin. Subsequently, the patient became afebrile, showed clinical improvement, and was discharged after 35 days of treatment. Through this case, we aim to emphasize an unusual pathogenic bacteria in the context of NP and the need for standardized surgical interventions in pediatric patients with NP.

Introduction

Necrotizing pneumonia (NP) is characterized by destruction of pulmonary tissue, resulting in multiple thin-walled cavities [1]. This condition predominantly affects children aged between 2 and 5 years and is an infrequent complication of community-acquired pneumonia (CAP), accounting for 3.7% of CAP cases [2]. The complication rate of pneumonia, including parapneumonic pleural effusion (PPE), empyema, NP, and lung abscess, is reported at 8.9% based on a retrospective study spanning nearly 2 decades by Masarweh et al. [3]. However, approximately 40% of pneumonia cases develop complications during hospitalization [3]. NP increases the risk of respiratory failure, PPE, empyema, pneumothorax, bronchopleural fistula, and septic shock. NP is also associated with increased mortality rates, prolonged febrile episodes, and extended hospitalization [2,4].

Antibiotics and surgical intervention are the 2 primary treatment modalities for cases of NP associated with PPE. A retrospective study involving 746 pediatric NP cases revealed 46.6%

requirement for chest tube placement and 6.1% necessity for video-assisted thoracoscopic surgery (VATS) [2]. Although there is no consensus on the criteria for chest tube placement and VATS, studies indicated that the rate of surgical intervention for complicated CAP ranges from 38% to 77% [2,3,5]. The relatively high rate of surgical management, which includes chest tube placement, VATS, and lobular resection, emphasizes the necessity of early disease detection and prompt treatment.

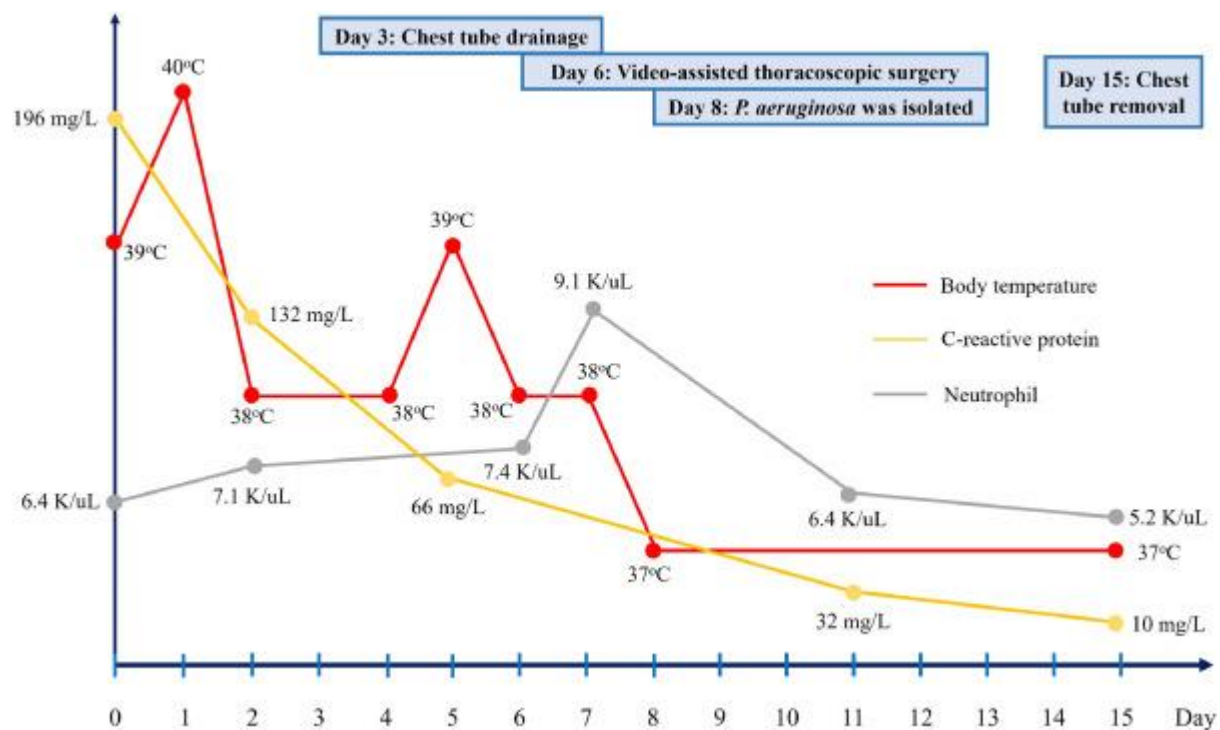
There is a lack of large-sample studies on NP in pediatrics, as NP remains an uncommon complication of CAP. Many aspects of NP remain unclear, including risk factors, methods for early screening and diagnosis of NP in outpatients with CAP, the role of lung ultrasound, and the microbiological characteristics of NP-causing agents. Furthermore, there are no [randomized controlled trials](#) to inform guidelines on [antibiotic](#) therapy or the timing of surgical intervention following antibiotic treatment failure. We present a complex case of NP and PPE associated with the unusual [pathogen P. aeruginosa](#) in a healthy 20-month-old child. This case highlights the success of combined antibiotic therapy, chest tube placement, and VATS.

Case report

A 20-month-old female patient was admitted to Children's Hospital 2 due to fever and respiratory distress. The illness persisted for 7 days before hospitalization, initially presenting with [upper respiratory infection](#) symptoms such as [coughing](#) and [rhinorrhea](#) during the first 2 days. Subsequently, the patient developed a fever of 39°C and a worsening productive cough that did not respond to oral antibiotics (amoxicillin/clavulanic acid at 45 mg/kg/day, divided into 3 doses) over the next 3 days. The patient was diagnosed with pneumonia and treated with [ceftriaxone](#) (100 mg/kg/day, divided into 2 doses) at a lower-level hospital for 2 days. However, the symptoms did not improve, leading to the patient's transfer to Children's Hospital 2. No reported perinatal or psychomotor [development disorders](#) were reported, and no significant [medical history](#) was noted. The patient had received the complete series of the 5-in-one vaccine but had not received [vaccinations](#) against influenza and [pneumococcus](#).

At Children's Hospital 2, the patient showed chest retractions, a heart rate of 150 beats per minute, a respiratory rate of 50 breaths per minute, weighing 11 kilograms, measuring 83 centimeters in height, and a SpO₂ level of 95% with supplemental oxygen delivered via a [cannula](#) 3 liter/minute. [Lung auscultation](#) revealed diminished breath sounds in the left lung and right-sided crackles. Examination of other organs did not detect any abnormalities.

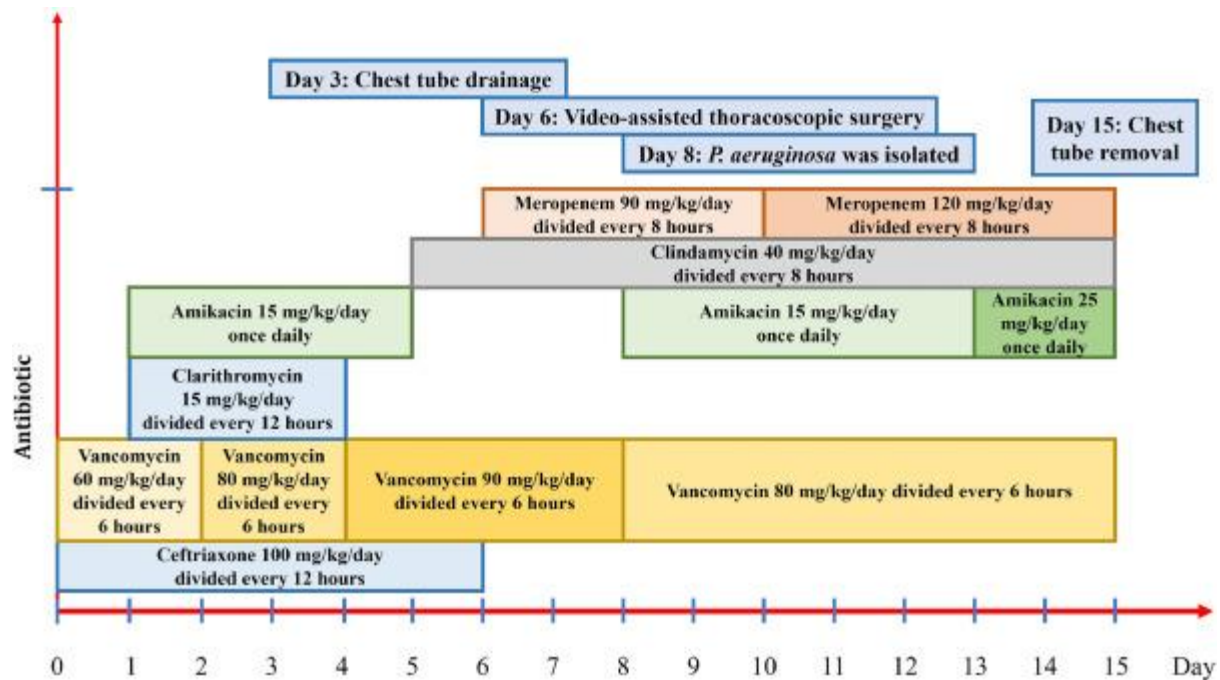
The clinical progression and [antibiotic](#) treatment are illustrated in [Fig. 1](#), [Fig. 2](#). During the first 3 days of antibiotic therapy, which included [vancomycin](#), [ceftriaxone](#), [amikacin](#), and [clarithromycin](#), the patient remained febrile, respiratory distress (requiring oxygen supplementation via nasal continuous positive airway pressure), and a chest X-ray revealed worsening [pulmonary consolidation](#) and [pleural effusion](#) ([Fig. 3](#)). The total [vancomycin](#) dose per day was modified based on the peak and [trough levels](#) of vancomycin ([Table 1](#)). The bedside lung ultrasound revealed consolidation and collapse of the left lung, with multiple hypoechoic lesions suggestive of [NP](#). Additionally, there was a moderate amount of [pleural effusion](#), with septations inside and [pleural thickening](#) ([Fig. 4](#)).



1. [Download: Download high-res image \(437KB\)](#)

2. [Download: Download full-size image](#)

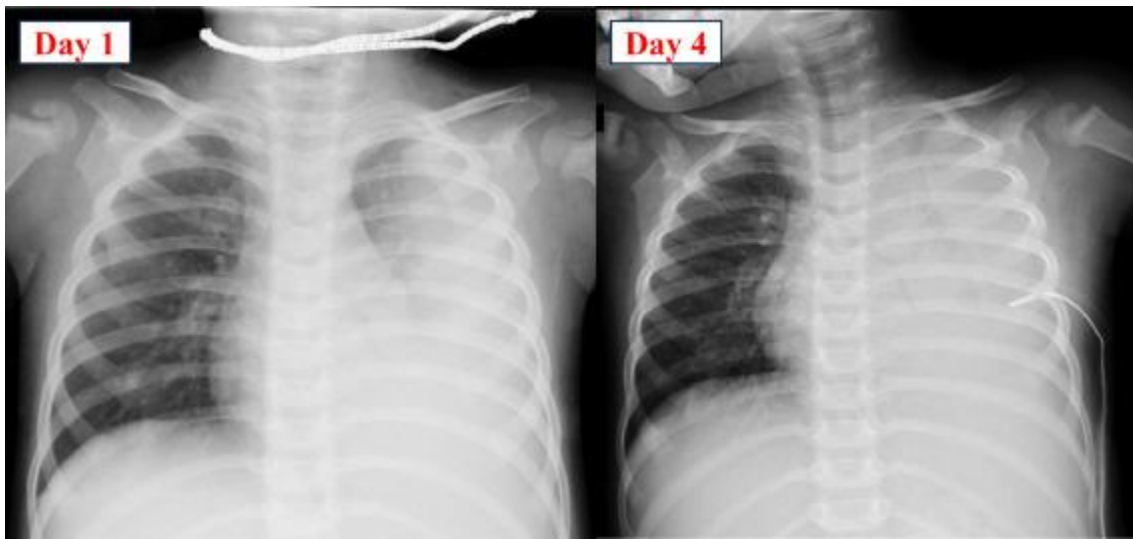
Fig. 1. The progression of body temperature, C-reactive protein level, and neutrophil count from day 1 to day 15 after hospitalization.



1. [Download: Download high-res image \(599KB\)](#)

2. [Download: Download full-size image](#)

Fig. 2. Summary of antibiotic types and duration of use by the patient.



1. [Download: Download high-res image \(330KB\)](#)

2. [Download: Download full-size image](#)

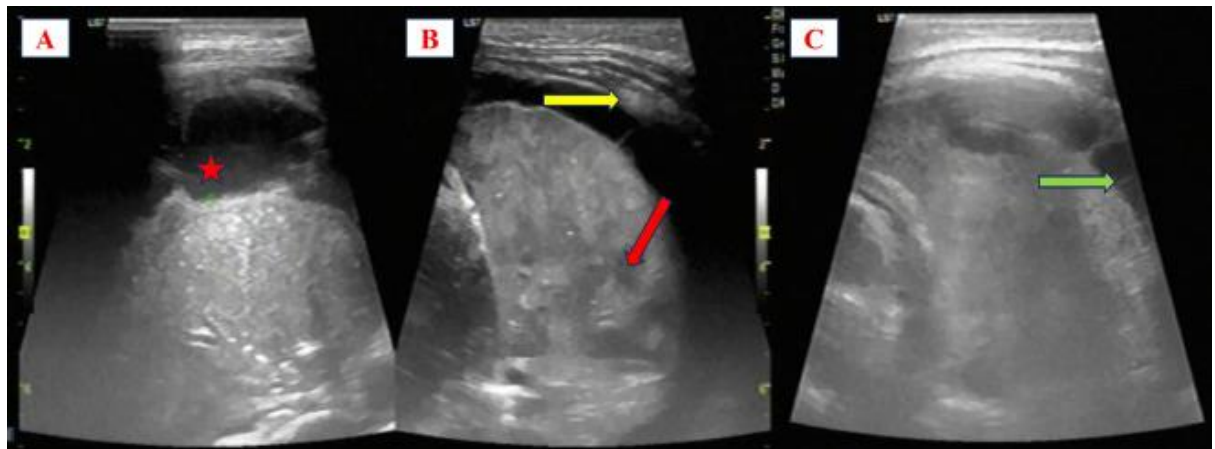
Fig. 3. The chest X-ray from day 1 to day 4 post-hospitalization revealed progressing left lung consolidation and pleural effusion despite antibiotic treatment.

Table 1. The patient's laboratory test results.

Laboratory tests	Normal range	Value
Blood		
Vancomycin trough level before fourth dose	µg/mL	2.28
Vancomycin peak level on the third day	µg/mL	22.25
Vancomycin trough level on the third day	µg/mL	5.57
AUC24 for vancomycin on the third day	µg/mL x hr	360
AST	<45 (U/L)	135
ALT	<40 (U/L)	5
Urea	1.67-7.49 (mmol/L)	2.2
Creatinine	20.33-88.4 (µmol/L)	30
Hemoglobin	10.5-14 (g/dL)	9.8
Platelet	150-400 (K/uL)	383

Laboratory tests	Normal range	Value
<i>Chlamydia pneumoniae</i> IgM		Negative
<i>Mycoplasma pneumoniae</i> IgM		Negative
Pleural fluid		
Protein	g/L	31.5
Glucose	mmol/L	2.5
LDH	U/L	3131
ADA	U/L	55
Neutrophil cellular component	%	80%
<i>Mycobacterium tuberculosis</i> PCR		Negative
Culture for bacteria		Negative
Nasotracheal aspiration specimens		
Culture for bacteria	Multi-drug-resistant <i>P. aeruginosa</i>	
GeneXpert MTB/RIF		Negative
<i>Mycobacterium tuberculosis</i> PCR		Negative
AFB		Negative

ADA, [adenosine deaminase](#); AFB, acid-fast bacilli; ALT, [alanine aminotransferase](#); AST, aspartate aminotransferase; AUC24, the area under the concentration-time curve from 0 to 24 hr; MTB, [Mycobacterium tuberculosis](#); PCR, polymerase chain reaction; RIF, [rifampicin](#). Abnormal values are highlighted in bold.

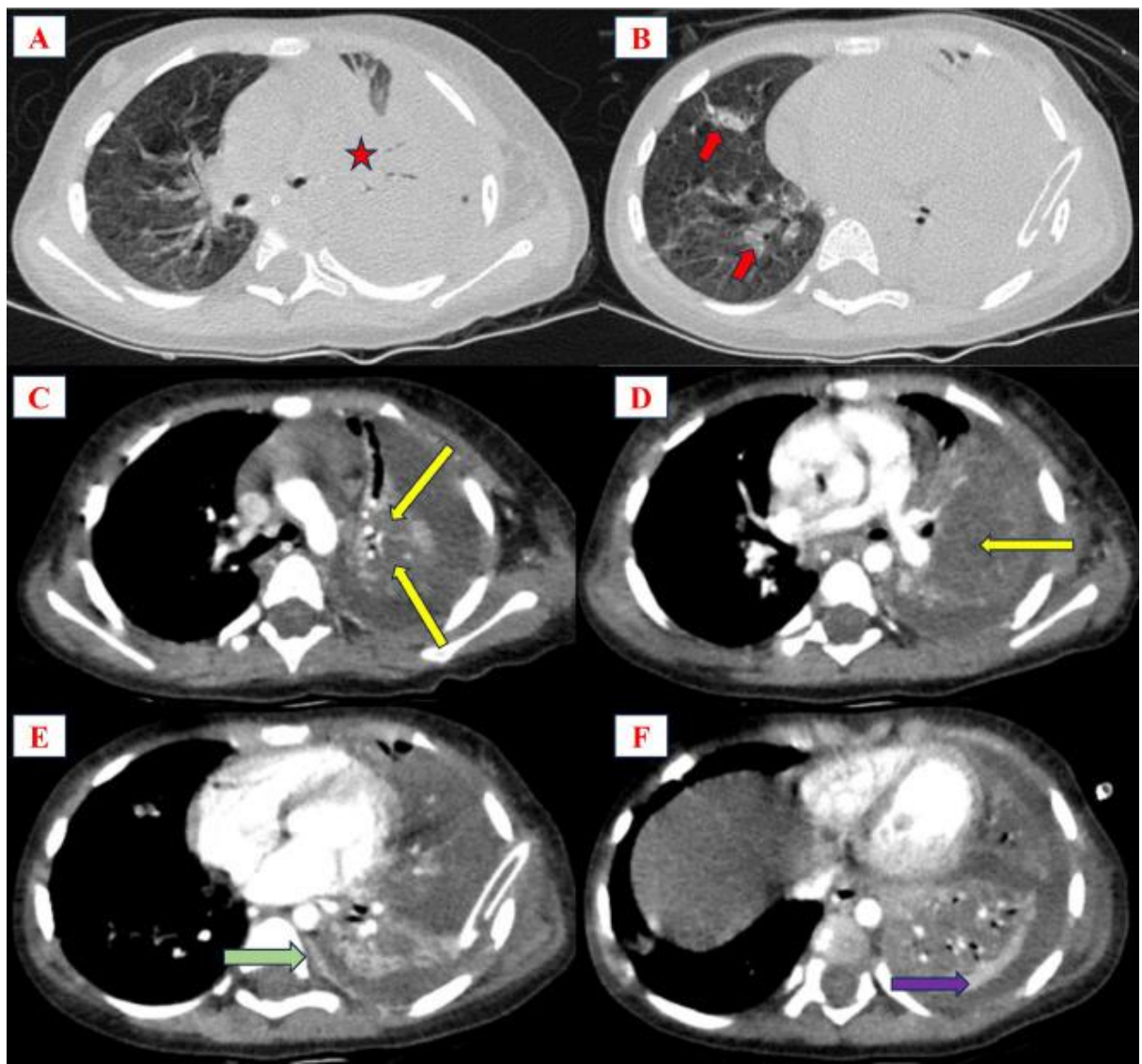


1. [Download: Download high-res image \(305KB\)](#)
2. [Download: Download full-size image](#)

Fig. 4. Bedside lung ultrasound on the third day. A shows echogenicity in the pleural fluid (red star). B shows multiple hypoechoic lesions within the left lung (red arrow) and pleural thickening (yellow arrow). C illustrates septation within the pleural cavity (green arrow).

On the third day, the patient underwent chest tube placement, leaking turbid yellow pleural fluid. The pleural fluid analysis is presented in [Table 1](#), with elevated LDH levels (3131 U/L) and reduced glucose levels (2.5 mmol/L), consistent with complicated PPE. Other laboratory tests are presented in [Table 1](#).

From day 3 to day 6 post-treatment (following the chest tube placement), the patient's fever persisted without improvement despite a reduction in CRP levels. Approximately 100 mL of turbid yellow pleural fluid through the chest tube per day was collected. The patient received additional intravenous clindamycin and an increased dose of vancomycin guided by AUC24. Blood cultures yielded negative results for bacterial growth. Transthoracic doppler echocardiography revealed no abnormalities. The contrast-enhanced chest computed tomography (CT) showed NP, PPE, and “split pleural sign” ([Fig. 5](#)).



1. [Download: Download high-res image \(955KB\)](#)
2. [Download: Download full-size image](#)

Fig. 5. Chest CT on the fourth day. A and B showed consolidation in the left lung with an air bronchogram sign (red star) and scattered consolidations in the right lung (red arrow). C and D revealed low-attenuated areas inside the consolidation, suggesting NP (yellow arrow). E and F showed thickened parietal (green arrow) and visceral (pink arrow) [pleura](#), referred to as “split pleural sign”.

The patient received [meropenem](#) supplementation based on the [multiplex PCR](#) results of nasal tracheal aspiration (NTA) presented in [Table 3](#), indicating a high concentration of [Stenotrophomonas maltophilia](#), [P. aeruginosa](#), and [Streptococcus pneumonia](#). During the [VATS](#) procedure on day sixth, nearly complete necrosis of the left upper lobe parenchyma with numerous pseudomembranes was observed. The pleural membranes of both upper and lower lobes were decorticated, pseudomembranes were removed, and adherent [lung parenchyma](#) was dissected. Multidrug-resistant *P. aeruginosa* ([Table 2](#)) was isolated from nasotracheal aspiration specimens (grade of Bartlett's criteria was 2 points), which were collected on the third day.

Table 2. Antibiotic susceptibility of *Pseudomonas aeruginosa*.

Antibiotic	Result	MIC
Piperacillin-Tazobactam	Susceptible	16/4 µg/mL
Ceftazidime	Resistant	> 16 µg/mL
Cefepime	Susceptible	8 µg/mL
Imipenem	Resistant	> 8 µg/mL
Meropenem	Resistant	> 16 µg/mL
Gentamicin	Resistant	> 8 µg/mL
Amikacin	Susceptible	≤ 8 µg/mL
Ciprofloxacin	Intermediate	1 µg/mL
Ceftazidime-Avibactam	Resistant	> 8/4 µg/mL
Colistin	Intermediate	≤ 1 µg/mL

MIC, minimum inhibitory concentration.

Table 3. The multiplex polymerase chain reaction results of nasal tracheal aspiration specimens.

Organism	CT	Result	Organism	CT	Result
Community-acquired bacteria			Fungal		
<i>Streptococcus pneumoniae</i>	28.1 4	7.47 × 10 ⁵	<i>Pan Aspergillus</i>	(-)	-
<i>Haemophilus influenzae</i>	33.2 6	2.14 × 10 ⁴	<i>Aspergillus fumigatus</i>	(-)	-
<i>Haemophilus influenzae type B</i>	(-)	-	<i>Aspergillus flavus</i>	(-)	-
<i>Moraxella catarrhalis</i>	(-)	-	<i>Aspergillus niger</i>	(-)	-
<i>Streptococcus pyogenes (GAS)</i>	(-)	-	<i>Aspergillus terreus</i>	(-)	-

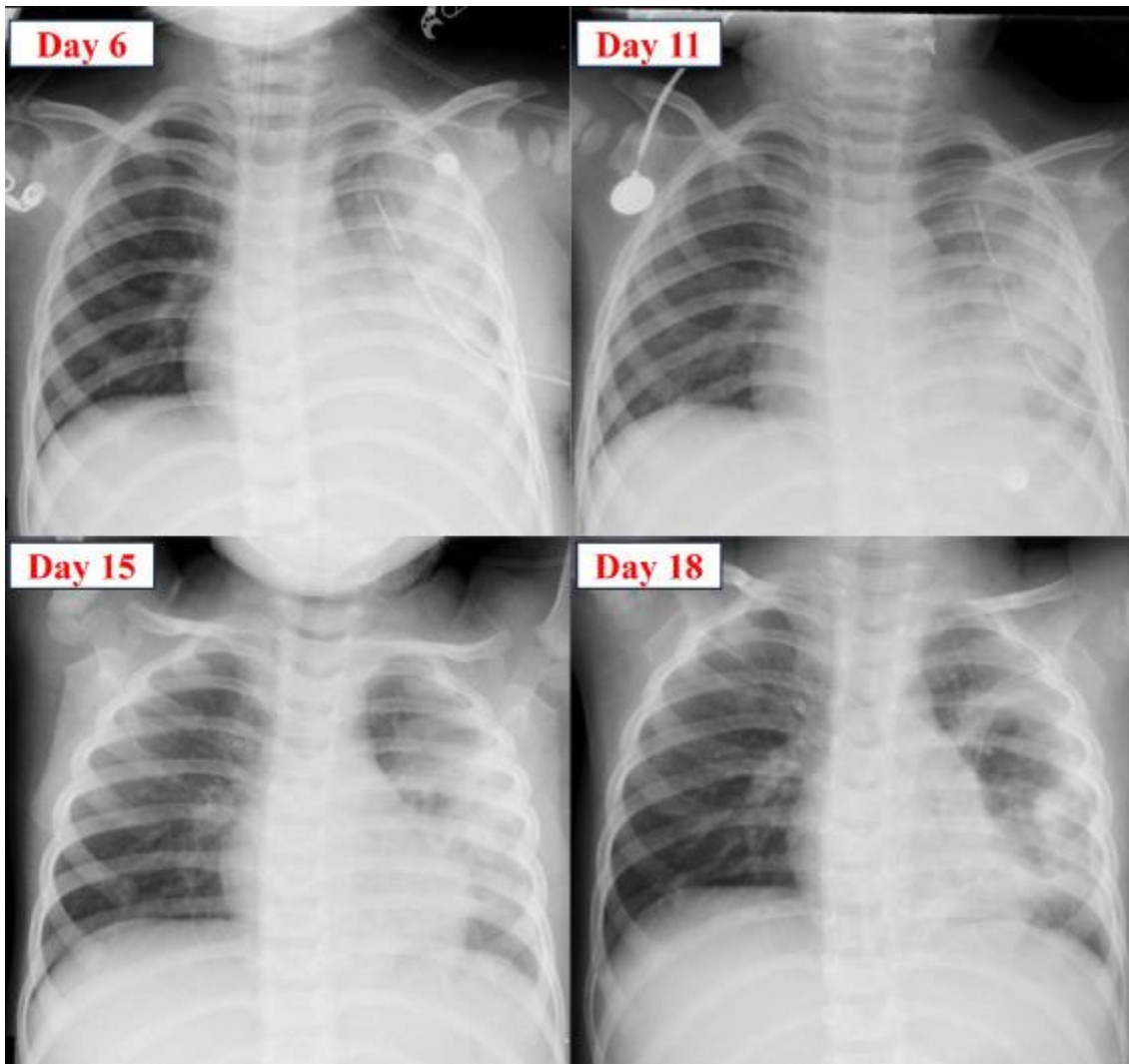
Organism	CT	Result	Organism	CT	Result
<i>Streptococcus agalactiae</i> (GBS)	(-)	-	<i>Candida albicans</i>	33.3 4	2.03×10^4
<i>Streptococcus suis</i>	(-)	-	<i>Candida kefyr</i>	(-)	-
Nosocomial bacteria			<i>Candida tropicalis</i>	(-)	-
<i>Staphylococcus aureus</i> (MRSA)	(-)	-	<i>Candida krusei</i>	(-)	-
<i>Staphylococcus aureus</i> (MSSA)	(-)	-	<i>Candida glabrata</i>	(-)	-
<i>Staphylococcus epidermidis</i> (MRS E)	(-)	-	<i>Cryptococcus neoformans</i>	(-)	-
<i>Staphylococcus epidermidis</i> (MSE)	(-)	-	<i>Pneumocystis jirovecii</i>	(-)	-
<i>Coagulase-negative staphylococcus</i>	32.1 1	4.76×10^4	<i>Penicillium marneffei</i>	(-)	-
<i>Panton Valentine Leukocidin</i> (PVL)	(-)	-	<i>Histoplasma capsulatum</i>	(-)	-
<i>Enterococcus faecalis</i>	(-)	-	<i>Fusarium oxysporum</i>	(-)	-
<i>Enterococcus faecium</i>	(-)	-	<i>Fusarium verticillioides</i>	(-)	-
<i>Escherichia coli</i>	(-)	-	<i>Coccidioides immitis/ posadasii</i>	(-)	-
<i>Enterobacter cloaceae</i>	(-)	-	<i>Sporothrix globosa</i>	(-)	-
<i>Enterobacter aerogenes</i>	(-)	-	<i>Sporothrix schenckii/ brasiliensis</i>	(-)	-

Organism	CT	Result	Organism	CT	Result
<i>Klebsiella pneumoniae</i>	(-)	-	<i>Mucormycosis (Rhizopus oryzae)</i>	(-)	-
<i>KPC</i>	(-)	-	<i>Fusarium solani</i>	(-)	-
<i>NDM-1</i>	(-)	-	Virus		
<i>Pseudomonas aeruginosa</i>	27.7 8	9.59 × 10^5	<i>Influenzavirus A</i>	(-)	-
<i>Burkholderia cepacia</i>	(-)	-	<i>Influenzavirus B</i>	(-)	-
<i>Burkholderia pseudomallei</i>	(-)	-	<i>Influenzavirus C</i>	(-)	-
<i>Acinetobacter baumannii</i>	36.4 4	2.36 × 10^3	<i>Parainfluenzavirus 1</i>	(-)	-
<i>Stenotrophomonas maltophilia</i>	25.6 5	4.20 × 10^6	<i>Parainfluenzavirus 2</i>	(-)	-
<i>Morganella morganii</i>	(-)	-	<i>Parainfluenzavirus 3</i>	(-)	-
<i>Providencia sp.</i>	(-)	-	<i>Rhinovirus</i>	(-)	-
<i>Proteus mirabilis</i>	(-)	-	<i>Respiratory syncytial virus (RSV)</i>	19.1 4	3.84×10^8
<i>Citrobacter freundii</i>	(-)	-	<i>Human metapneumovirus</i>	(-)	-
<i>Elizabethkingia meningoseptica</i>	(-)	-	<i>Measles virus</i>	(-)	-
<i>Fusobacterium nucleatum</i>	30.1 3	1.88 × 10^5	<i>Adenovirus</i>	(-)	-
Atypical bacteria			<i>Epstein-Barr Virus (EBV)</i>	26.8 1	1.88×10^6

Organism	CT	Result	Organism	CT	Result
<i>Mycoplasma</i>	(-)	-	<i>Cytomegalovirus (CMV)</i>	33.2	2.23×10^4
<i>Mycoplasma pneumoniae</i>	(-)	-	<i>Bocavirus</i>	(-)	-
<i>Chlamydia pneumoniae</i>	(-)	-	<i>Varicella-Zoster Virus (VZV)</i>	(-)	-
<i>Chlamydia trachomatis</i>	(-)	-	<i>Common-cold virus</i>	(-)	-
<i>Chlamydia psittaci</i>	(-)	-	<i>Rubella virus</i>	(-)	-
<i>Legionella pneumophila</i>	(-)	-	<i>SARS-CoV-2</i>	(-)	-
<i>Bordetella pertussis</i>	(-)	-	Mycobacterium		
<i>Bordetella parapertussis</i>	(-)	-	<i>Mycobacterium tuberculosis</i>	(-)	-
			<i>Nocardia asteroides</i>	(-)	-

CT, cycle threshold.

From the eighth day of treatment, the patient received additional [amikacin](#), continued [meropenem](#), vancomycin, and [clindamycin](#). The patient's condition improved with the resolution of fever, reduced CRP levels, and decreased [neutrophil](#) count. Chest X-rays showed improvement from the sixth day to the 18th day of treatment ([Fig. 6](#)). The patient was discharged on the 35th day of treatment.



1. [Download: Download high-res image \(661KB\)](#)
2. [Download: Download full-size image](#)

Fig. 6. Progression of the patient's chest X-ray from the sixth day to the 18th day of treatment.

Discussion

Our case describes a complex scenario of NP and PPE associated with an uncommon pathogen, *P. aeruginosa*, in a healthy 20-month-old child. The patient underwent successful treatment involving a combination of broad-spectrum antibiotics, chest tube placement, and VATS. Through this case, we intend to highlight the complexities of managing NP and PPE associated with *P. aeruginosa* in children.

Epidemiological studies illustrate inconsistent findings regarding risk factors for NP in children with CAP. Hsieh et al. conducted a retrospective study involving 71 children with NP due to *S. pneumoniae* in Taiwan, revealing that NP often progresses rapidly in previously healthy children. Identified risk factors for NP included an elevated immature neutrophil count, C-reactive protein levels exceeding 12 mg/dL, and the absence of pre-existing medical conditions [6]. Conversely, another study involving 746 children with NP indicated that complex chronic conditions increased the risk of NP and mortality [2]. Other potential risk factors, such as asthma and prior NSAIDS usage, have yet to be confirmed [1]. Moreover, lower SaO₂ levels, higher fever, and

elevated CRP levels in the complicated [CAP](#) group may predict the likelihood of requiring surgical intervention [3]. Although NP is a rare complication in children with CAP, clinical practitioners must remain alert to the potential rapid progression from CAP to NP in previously healthy [pediatric](#) patients.

P. aeruginosa is mainly recognized as a nosocomial infection and frequently causes diseases in immunocompromised, burned, or pediatric patients with [cystic fibrosis](#) [7]. However, *P. aeruginosa* is rarely reported as a pathogen in cases of CAP with NP in children. Common causative pathogens of pediatric NP include *S. pneumoniae*, *S. aureus*, *M. pneumoniae* [4], *Haemophilus influenzae*, and *Acinetobacter baumannii* [8]. A review of 197 bacterial or [fungal isolates](#) in children with NP revealed that 82% of NP cases were due to *S. pneumoniae* and *S. aureus*, with only 3 cases isolating *P. aeruginosa* (1.5%) [1]. The frequency of NP caused by *P. aeruginosa* is rare, as reported by Yonghan, accounting for only 1 out of 282 cases [8]. However, in children with complex chronic conditions, the rate of *P. aeruginosa* infection can increase up to 12.8%, compared to 4% in those without pre-existing medical conditions [2]. In adults, *P. aeruginosa* is recognized as a severe but rare causative agent of CAP, NP, or cavitation [lung disease](#), often associated with a high [mortality rate](#) [9]. In our case, *P. aeruginosa*, resistant to [ceftazidime](#) and [carbapenem](#), was isolated from NTA specimens. We cannot definitively confirm *P. aeruginosa* as the sole pathogen causing the disease; moreover, based on the [multiplex PCR](#) results, *S. pneumoniae* is also a potential coinfecting agent. We hypothesize that *P. aeruginosa* is the causative pathogen, given the higher copies per mL of *P. aeruginosa* compared to *S. pneumoniae* in the multiplex PCR results. Furthermore, the clinical progression lacks a distinct resolution phase, minimizing the suspicion of *P. aeruginosa* [superinfection](#) in the hospital. However, determining the actual causative agent remains challenging; hence, antibiotic therapy should still encompass common pathogens to address this uncertainty. NP associated with *P. aeruginosa* in a previously healthy child adds complexity to the treatment, as it is an unusual pathogen in this population. This poses a significant challenge in NP management since empirical antibiotics covering *P. aeruginosa* are not routinely used in NP cases.

Complicated CAP should be considered if symptoms do not respond to appropriate treatment within 48 to 72 hours [10]. Patients should undergo screening for PPE, NP, [lung abscess](#), [sepsis](#), or [metastasis](#) infection. Chest X-rays show lower sensitivity in diagnosing NP than [CT scans](#) [1]. Donnelly et al. highlighted that 50% of cases with fluid-filled cavities may be undetected on chest X-rays [11]. In the early stages of NP, the liquefied [lung parenchyma](#) not connected to the airway may be challenging to notice on X-rays. In cases of suspected NP, a chest CT scan should be performed. Several studies have used lung [ultrasonography](#) as a potential alternative to CT scans in diagnosing NP [12,13]. Lung ultrasonography offers the advantage of being noninvasive and avoiding radiation exposure, especially in the pediatric population. Moreover, impaired perfusion and hypoechoic lesions observed on ultrasonography can predict [pneumatocele](#) formation and correlate with necrosis in CT scans [12]. Our case encountered a delay in diagnosing NP, despite the potential for earlier diagnosis through lung ultrasonography. The lung ultrasonography images from the case correlated with findings on CT scans, including [pleural thickening](#), NP, and PPE.

The optimal timing for VATS intervention in cases of treatment failure with antibiotics and chest tube placement has yet to be confirmed. In our case, despite receiving broad-spectrum antibiotics and chest tube placement, the patient's condition did not improve. This could be attributed to the extensive [pleural thickening](#) and widespread lung parenchymal necrosis

contributing to treatment failure. VATS may aid in removing fibrous walls within the [pleural cavity](#), removing pleural peel to allow lung re-expansion, and eliminating pus from the pleural space under direct visualization. VATS is the first-line intervention when antibiotic treatment and chest tube placement fail, rather than an open [thoracostomy](#) [14]. Some authors define complicated NP as extensive necrosis or cavitation larger than 50% of the involved [lung lobe](#) [15,16]. Cases of complicated NP tend to require [wedge resections](#) or [lobectomies](#), and [postoperative complications](#), [pneumothorax](#), and more extended hospital stays are frequently observed. The recommended timeframe for surgical intervention in cases of NP and PPE unresponsive to appropriate treatment is 7 days [14]. Other situations requiring surgical intervention include complex [empyema](#) with significant lung pathology (extensive pleural thickening, trapped lung), [bronchopleural fistula](#), or secondary [empyema](#) [14]. Early VATS (e.g., within 24-48 hours of hospital admission) has been proposed by some authors due to its benefits in reducing hospital stay, complication rates, and the number of days with chest tube placement [17,18]. However, as VATS depends mainly on each center's and surgeon's experience, there is currently no consensus on the optimal timing for VATS procedures. Several studies have been conducted to predict extensive necrosis in NP using indicators such as CRP, [serum albumin](#), IgM [19], lung ultrasonography [12], or IFN- γ [20]; however, there are still limited data and [predictive factors](#) for the likelihood of requiring surgery during hospitalization.

Conclusion

Our clinical case highlights the complexities of managing NP in children. Multidrug-resistant *P. aeruginosa* can contribute to severe community-acquired NP in a healthy pediatric patient. Further research is needed to predict the likelihood of *P. aeruginosa* infection in NP, as empiric antibiotic therapy does not initially cover *P. aeruginosa*. Pediatric NP inpatients require close monitoring of clinical progression, as there is no consensus on the optimal timing or method of surgical intervention. Successful treatment relies on broad-spectrum antibiotics, chest tube placement, and timely surgical intervention.

Objectives

Cytoreductive surgery for advanced ovarian cancer involving a diaphragmatic or intrathoracic resection is associated with an increased risk of postoperative pleural effusion. Intraoperative chest tube placement has been shown to mitigate this risk. We aimed to analyze the factors that increase the risk of postoperative pleural effusion and identify the patients who could benefit most from intraoperative chest tube placement.

Methods

This was a retrospective cohort study of all patients with advanced ovarian cancer who underwent primary cytoreductive surgery with diaphragmatic and/or intrathoracic resection between January 1, 2015, and December 31, 2021. The Wilcoxon rank sum and Fisher's exact tests were utilized.

Results

A total of 421 patients with a median age of 61 years (range: 21–85) were included; 191 patients (45 %) underwent diaphragmatic peritonectomy only, 70 (17 %) had a full-thickness diaphragm resection only, and 160 (38 %) underwent additional intrathoracic procedures through a transabdominal approach. Among all 421 patients, 400 (95 %) had an optimal cytoreduction of

≤1 cm of residual disease, and 331 (79 %) had complete gross resection; 188 patients (45 %) had a chest tube placed

Conclusions

Among patients who undergo diaphragmatic resection as part of cytoreductive surgery for advanced ovarian cancer, age, CA-125 level, albumin level, residual disease status, and extent of diaphragm resection are factors associated with postoperative G3 pleural effusions. These factors should be considered if chest tube placement is omitted in this setting.

INTRODUCTION: Neurofibromas are peripheral nerve sheath tumours that occur sporadically or due to an underlying genetic disease such as neurofibromatosis.[1] Anywhere from 6-25% of neurofibromas occur in the thorax and mediastinum. On review of the literature, there is no case report of a pleural effusion secondary to an intrathoracic neurofibroma.

CASE PRESENTATION: An 81-year-old female with a history of a right chest wall neurofibroma, benign sphenoid meningioma and goiter, presented to the emergency department with delirium. On imaging, she had an incidental right pleural effusion (Figure 1). The patient had a pigtail chest tube inserted with pleural fluid analysis demonstrating an exudative effusion. A computed tomography (CT) chest was completed in the context of atypical cells found on cytology which was negative for malignant lesions. With a reduction in output (Figure 2), the pigtail was clamped. Two days later, there was evidence of significant reaccumulated pleural fluid. Repeat fluid analysis after reopening the tube to drainage grew Enterococcus faecalis. Although her positive culture was likely to be colonization of the tubing, and no loculations were observed on repeat CT (Figure 3), she was treated with ampicillin as per the infectious disease consultants. After switching the pigtail drain to an underwater seal, output continued to be minimal, and her chest tube was removed.

DISCUSSION: This case highlights the complexity in diagnosing the etiology of exudative pleural effusions with concurrent large intrathoracic neurofibromas not amenable to biopsy. One limitation to note is that we do not have genetic testing or biopsy results to confirm a diagnosis of neurofibromatosis. The sensitivity of pleural fluid cytology for malignant pleural effusions is low, 58.2%. [2] The pleural effusion was initially thought to be secondary to mass effect and lymphatic obstruction. However, lymphatic obstruction would result in a chylothorax which was not observed. [3,4] A triglyceride level would be indicated. [4] A pleural effusion from mass effect from benign tumors or malignant tumors carries the risk of recurrence, which has implications for long term management of chest tubes such as consideration of pleurodesis or tunneled pleural catheters. [3] Infection is another etiology to consider. Even prior to the positive E. faecalis growth, CT imaging was undergone as this has clinical utility in identifying airspace disease or loculations. [5] The second challenge presented is the decision to remove the chest tube without knowledge of the etiology and recurrence risk. Typically, chest tubes are removed once drainage falls below 20 ml/min for 8-12 hours without suction. [6] To make clinical decisions regarding removal, we recommend connecting the chest tube to a closed drainage system to augment drainage, identify patency and air leaks, and allow for suction. [6]

CONCLUSIONS: In conclusion, this case report highlights the importance of identifying etiology for a pleural effusion in a patient with an existing large intrathoracic mass to make practical decisions regarding chest tube removal or consideration of other techniques such as pleurodesis or tunneled catheters.

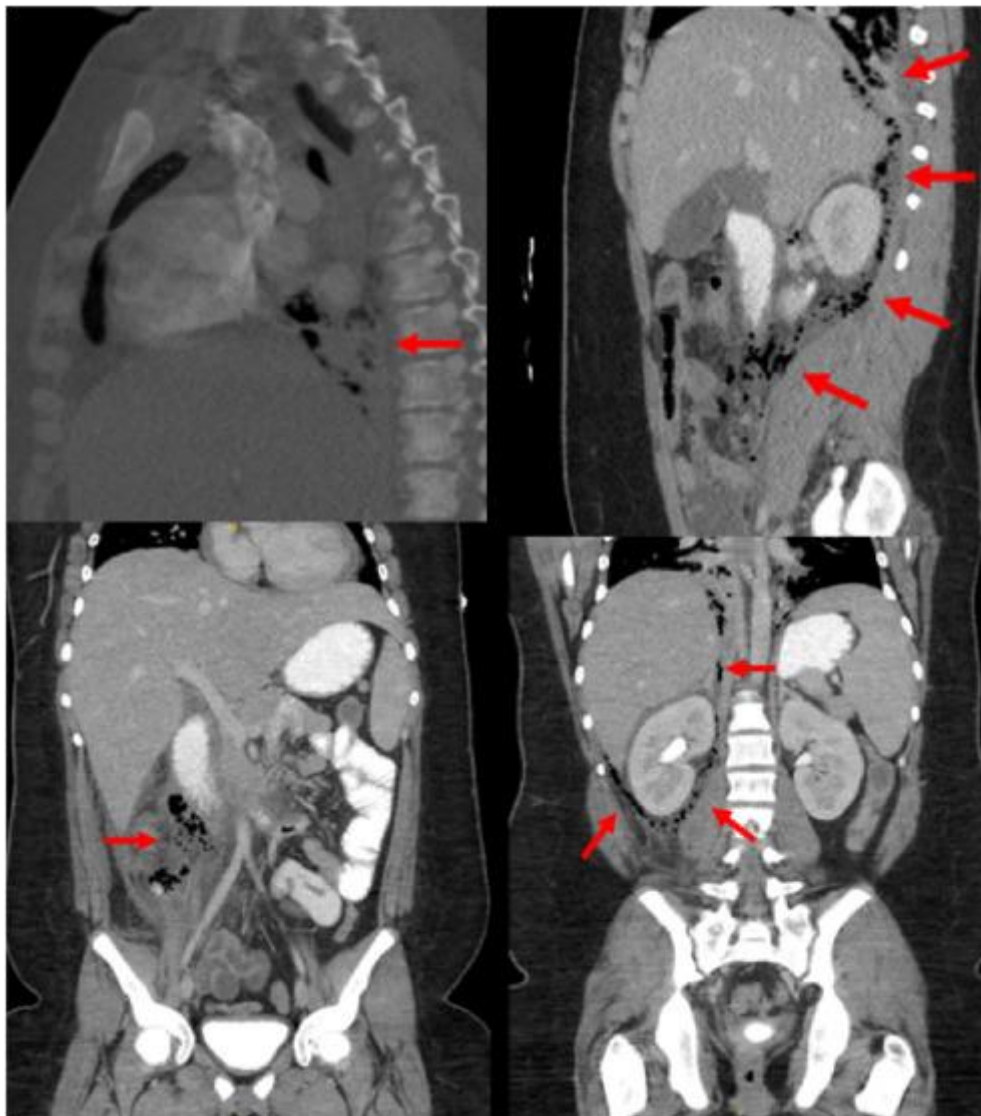
1. Background

[Acute appendicitis](#) is the most common abdominal surgical emergency encountered in the [Emergency Department](#) (ED) [1]. Referred [chest pain](#) is an extremely rare presenting symptom of [appendicitis](#). At the time of publication our case represents the first documented report of symptomatic [pneumomediastinum](#) as the primary symptom of ruptured appendicitis.

2. Case report

A 16-year-old male presented to our [pediatric ED](#) with [chest pain](#). He was awakened that morning by severe crushing left-sided chest pain and pleuritic shortness of breath. He was an otherwise healthy 16-year-old male with no significant [past medical history](#), took no medications, and had no [family history of sudden cardiac death](#) or hypercoagulable disorders. Review of systems was notable for an episode of diarrhea and abdominal pain two days prior that completely resolved prior to presentation. On arrival, he was febrile (38.2C), tachypneic (RR 36), tachycardic (145 BPM), with normal blood pressure and [oxygen saturation](#). Physical exam revealed a generally unwell appearing diaphoretic obese adolescent male with slightly muffled [heart sounds](#), clear lungs bilaterally, and minimal [abdominal tenderness](#). Initial triage EKG demonstrated [sinus tachycardia](#). Point of care cardiac ultrasound was positive for a small [pericardial effusion](#) with hyperdynamic cardiac function without regional wall motion abnormalities and a flat IVC. Chest X-ray showed no acute cardiopulmonary processes. Initial laboratory workup included serum chemistry, [troponin](#), CBC, ESR, CRP, and D-dimer and was notable for [hyponatremia](#) (129 mmol/L), [hypokalemia](#) (2.2 mmol/L), [leukocytosis](#) (13.9 K/ μ L), elevated ESR (93 mm/hr), elevated CRP (44.2 mg/dL), undetectable troponin, and elevated D-dimer (852 ng/mL).

A [CT pulmonary angiogram](#) was then obtained due to concern for [acute pulmonary embolism](#) and revealed a small pericardial effusion with stranding and [pneumomediastinum](#) and air tracking along the medial inferior aspect of the liver with no [pulmonary embolus](#). Further CT imaging of the abdomen and pelvis with IV and oral contrast demonstrated [perforated appendicitis](#) with [pneumoretroperitoneum](#) tracking into the mediastinal and retrocardiac space ([Image 1](#)). Pediatric surgery, [cardiology](#), and infectious disease teams were consulted. The patient was started on broad-spectrum antibiotics, subsequently became hypotensive, and was taken to the operating room for [exploratory laparotomy](#) which resulted in ileocecal resection and placement of end [ileostomy](#). The patient was found to have bowel necrosis in the [ascending colon](#), necrotic tissue and pus within the paracolic gutter, and pus in Gerota's [fascia](#) surrounding the right kidney. Blood cultures and intraoperative wound cultures were positive for *E. Coli*, [Enterococcus Faecalis](#) Group D, [Staphylococcus Haemolyticus](#), and [Enterococcus Durans](#) Group D. Patient was admitted to the PICU.



1. [Download: Download high-res image \(883KB\)](#)

2. [Download: Download full-size image](#)

Image 1. CT with IV contrast with perforated appendicitis, pneumomediastinum, and [pneumoretroperitoneum](#).

3. Outcome and follow-up

The patient's hospital course was complicated by [septic shock](#) requiring multiple vasopressors, prolonged [intubation](#), and purulent [pleural effusions](#) requiring IR guided catheter drainage, all prolonging his PICU stay to a total of 28 days. His fevers subsided 29 days after admission and he was treated with IV antibiotics for 33 days. He was eventually discharged 37 days after admission in stable condition. 115 days following his discharge, he underwent reversal of his [ileostomy](#) with primary [end to end anastomosis](#) without complications. He is continuing to do well six months after his initial hospitalization.

4. Discussion

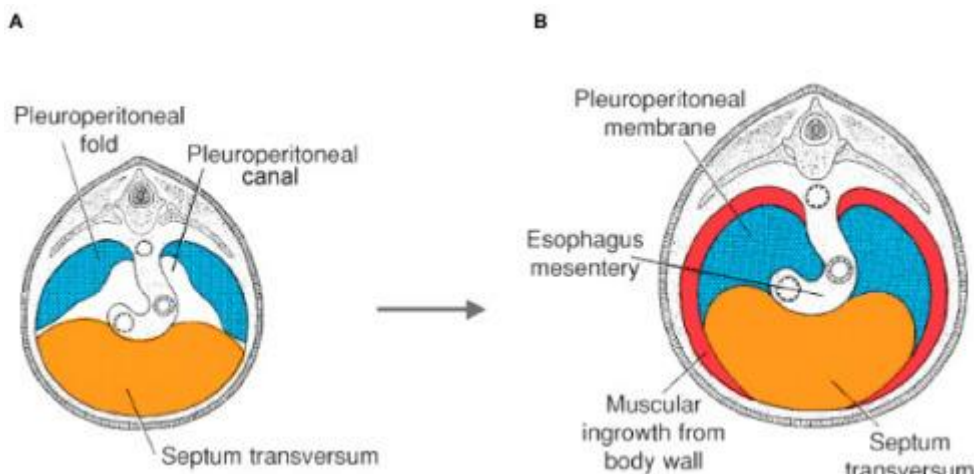
[Appendicitis](#) is the most common abdominal surgical emergency. Overall mortality is usually ~1% in the United States in uncomplicated cases, but significant morbidity is often seen in patients

with perforation and [retroperitoneal abscess](#) [1,2]. Appendicitis, which can frequently present in an atypical fashion, is well-known for being a “great mimicker” of other diagnoses, often making diagnosis based solely on history and physical examination difficult [3]. “Referred pain” is frequently described in the [geriatric](#) population as the etiology of missed diagnoses – including a single described case of an older man who was admitted for a cardiac workup in the setting of acute left sided chest pain only to be discharged and return with [perforated appendicitis](#) [4]. Conversely, “referred pain” is generally understood to be less prevalent in the [pediatric](#) population. Chest pain is an increasingly common presenting chief complaint in children, and while it is usually benign in nature, the differential is extremely broad – including musculoskeletal, idiopathic, psychogenic, respiratory, gastrointestinal and primary cardiac causes [[5], [6], [7]].

Chest pain as a [sequela](#) of perforated appendicitis is a rare presentation of a severe disease state that is consistently missed by emergency physicians [8]. [Pericarditis](#) and [pericardial effusions](#) caused by perforated appendicitis have been described in the past, including one case report described a patient presenting in [cardiac tamponade](#) requiring drainage who was eventually discharged after a two-month hospitalization and an extensive negative cardiac workup, only to return five days later to the ED where CT imaging diagnosed perforated appendicitis [9,10]. It has been speculated that these rare cases of pericarditis due to appendicitis are caused by seeding of the [pericardium](#) during transient [bacteremia](#) secondary to perforated appendicitis [11].

Pneumomediastinum is an exceedingly rare complication of perforated appendicitis. It has been described in the literature in a handful of cases as an incidental sequela of perforated appendicitis in patients with significant abdominal pain [12,13]. Our case is unique in that the patient presented with significant chest pain secondary to pneumomediastinum with a benign abdominal exam, making the initial clinical suspicion for appendicitis extremely low. Patients with perforated appendicitis and an associated pneumomediastinum tend to be more acutely ill, require multiple operations, and have prolonged hospitalizations with significantly higher mortality [14].

Unraveling the anatomic connections that allow for the communication of free air between the [retroperitoneum](#) and the mediastinum necessitates revisiting human embryology. In early development, the coelomic cavity encompasses what eventually becomes the chest and abdomen ([Image 2](#)). The [pleuroperitoneal](#) membranes, [septum transversum](#), and body wall converge to form the diaphragm which converts the coelomic cavity into the peritoneal, pleural, and pericardial sacs [15]. Microscopic defects in the pleuroperitoneal canals allow for a direct communication between the retroperitoneum and mediastinum, with broad [clinical significance](#) for both abdominal and [cardiothoracic](#) disorders.



1. [Download: Download high-res image \(466KB\)](#)
2. [Download: Download full-size image](#)

Image 2. The coelomic cavity.

5. Conclusion

Pneumomediastinum and pericardial effusion are extremely rare findings in the setting of [acute appendicitis](#). These findings have historically been misattributed to incorrect diagnoses that have led to significant delays in appropriate patient care as well as substantial increases in morbidity and mortality. Appendicitis is an extremely common ED diagnosis, and its rare complications and unique presentations should be thoroughly understood by emergency physicians and pediatric surgeons.

- 1.

Patient consent: Written [informed consent](#) was obtained from the patient and his mother per hospital research guidelines.

- 2.

Funding: No funding or grant support.

- 3.

Authorship: All authors attest that they meet the current ICMJE criteria for Authorship

SESSION TITLE: Disorders of [Pleura](#) Case Report Posters 9

SESSION TYPE: Case Report Posters

PRESENTED ON: 10/10/2023 09:40 am - 10:25 am

INTRODUCTION: Buffalo chest is a rare entity, named for the animal's incomplete separation of the left and right pleural spaces.¹ In humans, while buffalo chest may be congenital, it has also occurred after heart and [lung transplantation](#), [esophagectomy](#), [sternotomy](#), [thoracotomy](#), and Nuss procedure.² Patients often present with bilateral pneumothoraces.³ Here we present the first reported case in the literature of buffalo chest presenting with bilateral [pleural effusions](#).

CASE PRESENTATION: A 28-year-old female with a history of right atrial [angiosarcoma](#) diagnosed via [sternotomy](#) with biopsy in 2020, resection in 2021, and chemotherapy with [doxorubicin](#) for [metastatic disease](#) presented to the ED with dyspnea. She was found to have right greater than left bilateral [pleural effusions](#). Right [thoracentesis](#) removed 750mL of serosanguinous fluid with improvement in symptoms. After two days, a CT showed re-accumulation of her effusions and a left thoracentesis removed 1.6L of fluid negative for [malignancy](#). Repeat imaging showed reduction of both effusions. The following day, fluid quickly recurred and a chest drain was placed on the right side. Concurrent ultrasound of the left lung showed a reducing effusion while 1.7L was drained from the right. Post-procedure imaging revealed improvement of bilateral effusions as well as a posterior communication between the [pleural spaces](#). Her chest drain was removed after the output diminished, and she was discharged home the following week without subsequent recurrence.

DISCUSSION: Buffalo chest can be diagnosed by direct or radiographic visualization.³ Our patient's improvement of bilateral pleural effusions with drainage of either side strongly suggested the presence of a contiguous [pleural space](#) confirmed by CT imaging. Our patient's two prior sternotomies were likely the cause of her buffalo chest. Most iatrogenic communications likely heal over time, possibly in a few days.² While the patient's active [malignancy](#) and chemotherapy may have [impaired healing](#) of the pleuro-pleural connection, she had no other postoperative wound complications. This physiology is typically disadvantageous. A unilateral [pneumothorax](#) would present as bilateral pneumothoraces in the setting of buffalo chest, which may progress to tension physiology. Malignancy can spread through such a communication leading to progression of disease, but we do not suspect that this played a significant factor in our patient's pulmonary and hepatic metastases.² However, the [anatomy](#) was beneficial as the right pigtail catheter drained both pleural effusions without the need for bilateral chest drains or [thoracenteses](#).

CONCLUSIONS: Buffalo chest is a rare interpleural communication typically presenting with simultaneous [bilateral pneumothoraces](#). Patients with a prior history of mediastinal surgery are at risk and may present with bilateral pleural effusions instead. Both entities can be managed with a single-sided chest drain.

Introduction

We investigated the usefulness and safety of chest tube removal regardless of drainage volume of pleural effusion in patients who underwent anatomical pulmonary resection.

Methods

This multicenter, randomized controlled, non-inferiority trial included patients who underwent anatomical pulmonary resection (segmentectomy or lobectomy). Patients with chest tube drainage volume >300 mL/24 hours on the second postoperative day (POD 2) were randomly assigned to group A (removal of chest tube on POD 2) or group B (continuation of chest tube drainage until drainage volume decreased to ≤300 mL/24 hours). The primary endpoint was the frequency of respiratory-related adverse events

Results

The study included 1466 patients who were registered preoperatively to undergo anatomical pulmonary resection between April 2019 and October 2021. Of these 1466 patients, 175 (12.0%) patients whose chest tube drainage volume was >300 mL/24 hours underwent secondary

registration on POD 2. One patient who developed chylothorax after randomization was excluded from the study. Therefore, the study eventually included 88 patients (group A) and 86 patients (group B). We observed ≥Grade 2

Conclusions

Chest tube removal was safe regardless of drainage volume of pleural effusion in patients who underwent anatomical pulmonary resection. (jRCT1032180389)

SESSION TITLE: Disorders of [Pleura](#) Case Report Posters 1

SESSION TYPE: Case Report Posters

PRESENTED ON: 10/10/2023 09:40 am - 10:25 am

INTRODUCTION: Radiation therapy is one of modalities used to manage lymphomas and [solid tumors](#) and has been associated with various complications. This case report describes a rare case of recurrent [pleural effusion](#) in a 42 year old male patient with history of right vagus sheath tumor status post-surgical resection and recent radiation therapy 2 months prior to presentation. Radiation related [pleural effusion](#) is a condition characterized by recurrent pleural effusions. The infrequency with this condition makes it a formidable diagnostic challenge.

CASE PRESENTATION: A 42 year old male with a history of right Vagus sheath tumor status post surgical resection and 33 cycles radiation therapy, presented with the chief complaints of shortness of breath, [cough](#) and fever. chest x-ray showed right [pleural effusion](#). A [thoracentesis](#) drained 2.6L of bloody exudative with RBC 28000, WBC 905 (72% lymphocytes) and analysis revealing an exudative pattern. Pleural analysis including multiple [cytology](#) studies and ADA were negative. Pleural fluid [gram stain](#) and culture for AFB, fungal were negative. Infectious work up including [legionella](#), TB Quantiferon, fungitell, [aspergillus](#), urine [blastomycosis](#), [histoplasmosis](#), [mycoplasma](#) were negative. Blood and respiratory cultures were negative. A pigtail chest tube was inserted and high-dose corticosteroids was initiated. On the basis of the radiotherapy history, clinical manifestations, and pleural pathological analyses, a diagnosis of radiation therapy related [pleural effusion](#) was considered for our patient. The patient was treated with 40mg of [prednisone](#) daily resulting in a significant reduction in pleural effusion and an improvement in their physical condition.

DISCUSSION: Radiation therapy related- pleural effusion secondary to radiation treatment for lymphoma has rarely been described in the literature. Multiple case reports have been reported involving recurrent pleural effusion 8-23 years following mediastinal radiotherapy for [Hodgkin's disease](#) (1). In the current case, unilateral pleural effusion in the right chest, which was identified as exudative in nature based on Light's criteria, repeatedly occurred 3 months after radiotherapy. However, the manifestations, laboratory tests, imaging, and pathologic findings of our patient were non-specific and did not suggest any signs of infection or [malignancy](#), thereby making it difficult to perform an accurate diagnosis. A definitive diagnosis of radiation related pleural effusion is always presumptive. It necessitates a thorough work-up to rule out other disorders. Considering the history of the patient, the possibility of persistent pleural effusion related to a secondary malignancy must be strongly considered first. However, laboratory or imaging findings failed to provide any convincing evidence for our patient to support such a diagnosis. Another suspicion that should be raised from our physicians was [malignant pleural mesothelioma](#) (MPM), which has been noted as a secondary malignancy in patients who received chest radiotherapy. In the present study, the possibility of MPM was ruled out through a comprehensive evaluation(1).

CONCLUSIONS: In summary, radiation therapy-related pleural effusion is a rare complication that requires a thorough work-up to exclude other disorders, including [malignant pleural mesothelioma](#). Diagnosis can be challenging due to non-specific manifestations and laboratory findings. Prompt recognition and treatment are crucial, and more research is needed to improve our understanding of this condition.

Case Presentation

A 50-year-old woman with a history of [permanent atrial fibrillation](#) (AF) treated with [radiofrequency catheter ablation](#) (RFCA) 6 months ago was admitted to the respiratory department of a tertiary hospital because of recurrent episodes of pleuritic [chest pain](#) in the preceding 5 months. The patient reported multiple visits to a regional hospital, where she was treated with broad-spectrum antibiotics after discovery of a left alveolar consolidation on [chest radiograph](#) ([Fig 1](#)), subsequently imaged with CT scan ([Fig 2](#)). On treatment failure and appearance of a left-sided [pleural effusion](#) during outpatient follow-up, the patient was re-admitted. Pleural fluid was obtained via [thoracocentesis](#) characterized by exudative features and lymphocytic predominance. Abdomen CT scan, with IV and per os contrast agent, was devoid of findings consistent with [malignancy](#), and serum autoantibody levels were below positivity cut off values (anticellular, [cyclic citrullinated peptide antibody](#), [rheumatoid factor](#), and anti-neutrophil cytoplasmic antibodies). The patient underwent flexible [bronchoscopy](#) without endobronchial pathology on visual inspection. Microbiologic studies and cytological examination of samples obtained by bronchial washing/aspiration yielded no clinically relevant information. Lung perfusion/ventilation [scintigraphy](#) was ordered to exclude [chronic thromboembolic pulmonary hypertension](#); however, a deficit in [vascularization](#) for the left inferior lobe was found, prompting further investigation ([Fig 3](#)). Progression of left inferior lobe consolidation and the presence of a small [pericardial effusion](#) became evident on reimaging after a 2-month interval. The patient was empirically started on corticosteroids. After emergence of left hilar [lymphadenopathy](#) (< 1 cm), a PET-CT scan was performed. The left lower inferior lobe consolidation, whose metabolic activity pattern was consistent with that of inflammation (standardized uptake value equal to 4.4) ([Fig 4](#)), as well as the left sided-pleural effusion were markedly improved compared with previous imaging 20 days after corticosteroid initiation ([Fig 2](#)). On the grounds of recalcitrant pleuritic pain and pleural effusion recurrence during corticosteroid tapering, the patient was referred to the respiratory department of our university hospital to have her condition diagnosed.

Physical Examination Findings

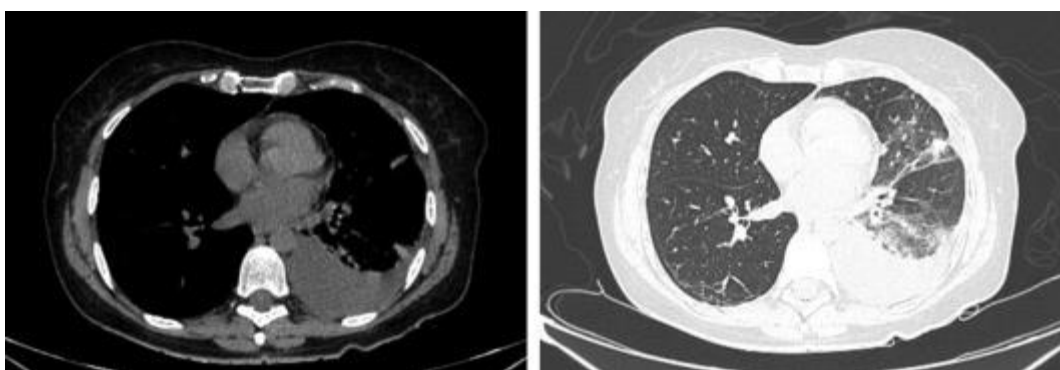
At presentation, the patient was hemodynamically stable (BP, 123/74 mm Hg) with peripheral capillary hemoglobin saturation of 96%. Peripheral lymph nodes were normal. During [lung auscultation](#), the lower left lung field was silent. No pathological [heart sounds](#) were detected. No other abnormalities were found.



1. [Download: Download high-res image \(103KB\)](#)

2. [Download: Download full-size image](#)

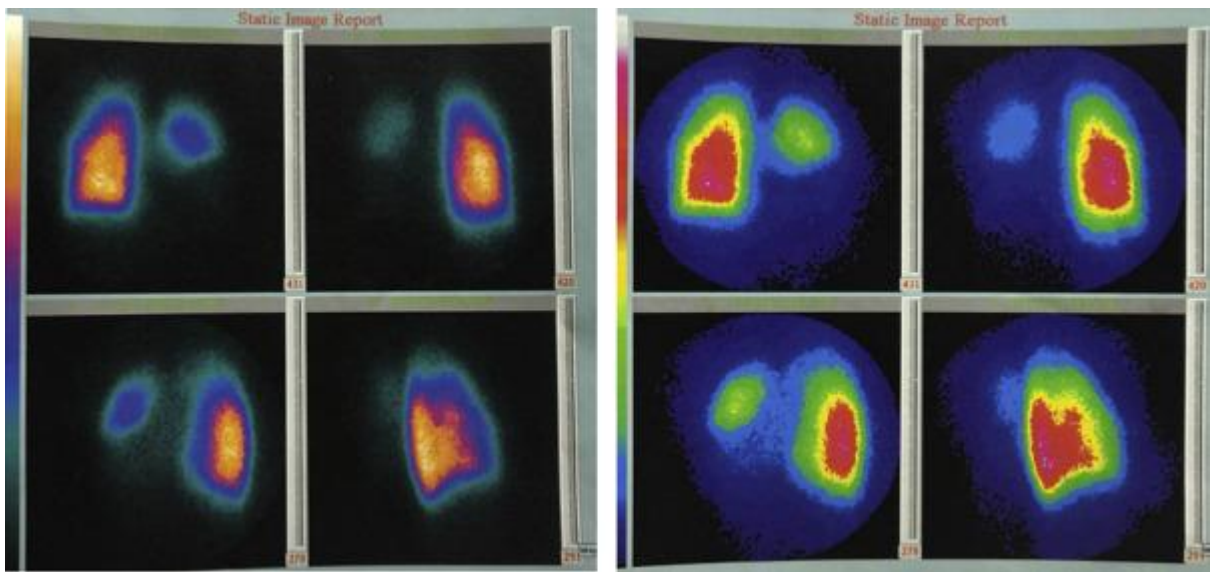
Figure 1. Chest radiograph compatible with left pleural effusion.



1. [Download: Download high-res image \(125KB\)](#)

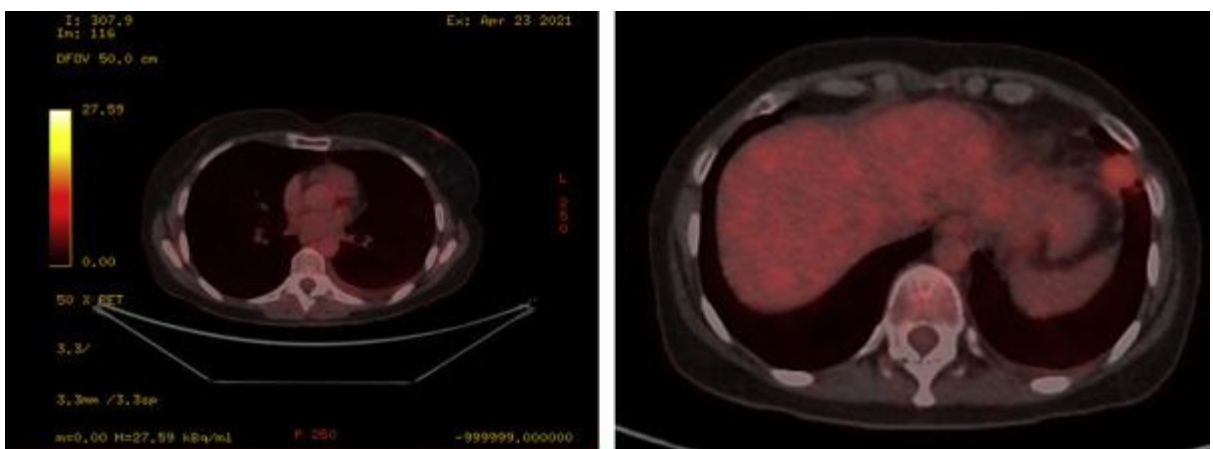
2. [Download: Download full-size image](#)

Figure 2. Airspace opacification in left inferior lobe and pleural fluid in left hemithorax.



1. [Download: Download high-res image \(276KB\)](#)
2. [Download: Download full-size image](#)

Figure 3. Lung perfusion blood scan showing a deficit in [vascularization](#) for the left inferior lobe. The scan was performed to the peripheral hospital after inspiration of the pleural fluid.



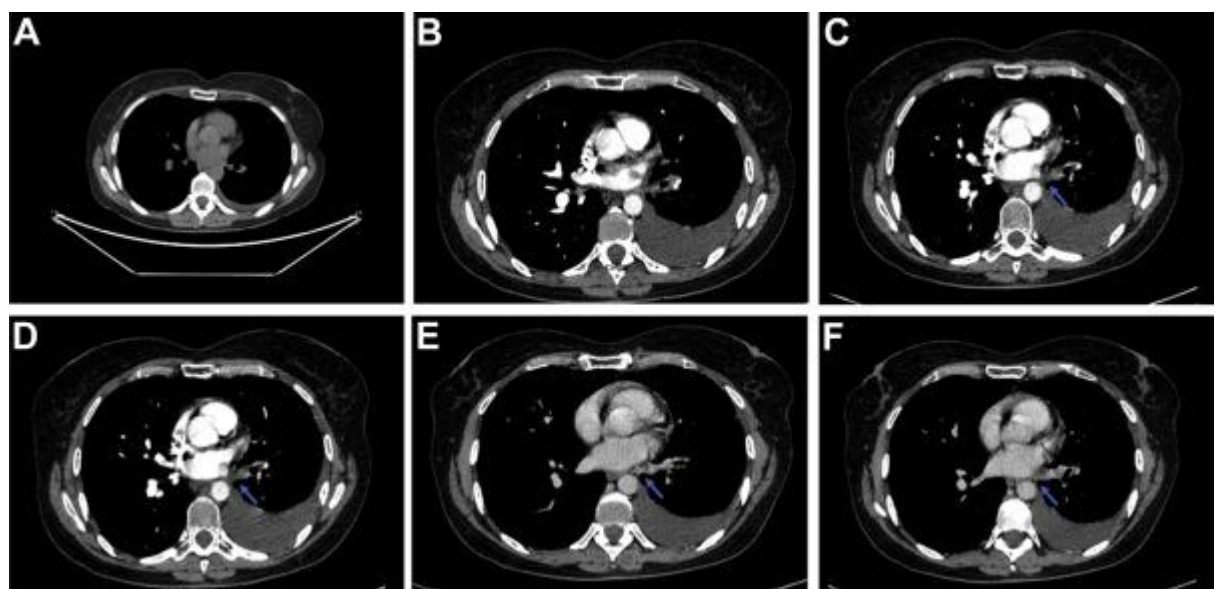
1. [Download: Download high-res image \(122KB\)](#)
2. [Download: Download full-size image](#)

Figure 4. PET-CT showing reduction of the pleural effusion and the consolidation in the left inferior lobe with low SUV.

Diagnostic Studies

Per [arterial blood gas analysis](#), Po_2 , Pco_2 , and pH were 75 mm Hg, 34 mm Hg, and 7.46 respectively. ECG showed [sinus rhythm](#) pattern. Transthoracic [echocardiogram](#) was normal, and [CT pulmonary angiogram](#) revealed no filling defect consistent with [pulmonary embolism](#). WBC count ($8.4 \times 10^9/\text{L}$) was normal, and C-reactive protein was mildly increased (2.7 mg/dL; normal values, 0-1.5 mg/dL). In addition, prothrombin time/international normalized ratio, activated [partial thromboplastin time](#), and plasma levels of [proteins S](#), [C](#), and [antithrombin III](#) were all within physiological limits. Genetic screening did not detect well-known prothrombotic polymorphisms of [factor V](#), antithrombin III, [proteins C](#) and S, prothrombin,

and [plasminogen activator inhibitor 1](#). Blood, urine, and [sputum cultures](#) were negative. Pleural fluid obtained by [thoracocentesis](#) showed exudative features with lymphocytic predominance (280 cells per well, 70% lymphocytes), [adenosine deaminase](#) concentration of 15 U/mL, and pH of 7.6. The cytological examination of pleural fluid specimens was negative for [malignancy](#). Imaging of [mediastinal lymph node](#) stations by means of endobronchial US disclosed no malignant features. Considering the filling defect of [lung perfusion scintigraphy](#) and the past [surgical history](#) of [RFCA](#), a CT angiogram in the venous phase was performed that successfully visualized stenosis and infarction by [thrombi](#) of the left inferior [pulmonary vein](#) (Fig 5). [Transesophageal echocardiography](#) was then recommended to measure pulmonary vein [blood flow velocities](#); however, the patient refused to undergo the procedure and did not provide written consent, for undisclosed reasons.



1. [Download: Download high-res image \(214KB\)](#)
2. [Download: Download full-size image](#)

Figure 5. A, Scan before contrast dye. B, C, D, Early-phase CT scan with contrast showing material in the left inferior vein (LIV) with coexistence of pleural effusion. E, Z. Flow obstruction in the left inferior vein (LIV), by [thrombi](#) (blue arrow).

What is the diagnosis?

Diagnosis: [Pulmonary vein stenosis](#) (PVS) complicated by pulmonary [vein thrombosis](#) (PVT) in the setting of [postoperative complications](#) of RFCA for AF.

Discussion

[Radiofrequency catheter ablation](#) has been increasingly used to abolish foci within the [pulmonary veins](#) that may trigger AF by producing [ectopic beats](#) in patients with drug-refractory or symptomatic [paroxysmal AF](#) and symptomatic [permanent AF](#). Despite significant theoretical and technological advancements, rare detrimental complications may occur. [Pulmonary vein stenosis](#) arises during the late postprocedural phase (approximately 2–5 months) and is accompanied by considerable patient morbidity, according to a well-designed study involving meticulous follow-up of 10,368 patients. Conversely, co-existence of PVS and [PVT](#) is less prominent and has only been described in select case reports.

The exact mechanism leading to PVS/PVT post-RFCA requires further elucidation. At the tissue level, radiofrequency-derived thermal energy is associated with cardiomyocyte death followed by [myofibroblast](#) proliferation, organizing [thrombus formation](#), endovascular contraction, [intimal thickening](#), and laminal [sclerosis](#) of postcapillary pulmonary veins. Additionally, in the case of PVT, besides the inflammatory process leading to stenosis, possibly the turbulent flow inside the stenotic area further damages the endothelium, leading to thrombus formation. The number of vessels involved, the degree of stenosis, the energy level used, the experience of the operators, and the ablation strategy contribute to the development of complications. However, compensatory [hemodynamics](#) and [collateral circulation](#) may underlie spontaneous improvement of many cases.

Clinical manifestations of PVT are atypical and involve shortness of breath, decrease in exercise capacity, cough, chest pain or discomfort, and [hemoptysis](#). Cases presenting with consolidation or [pleural effusion](#) may initially be confounded with pneumonia, [malignancy](#), [pulmonary embolism](#), or even autoimmunity. Given that a large number of cases are initially misdiagnosed and mistreated and that most centers do not routinely screen patients after ablation, approximations of real-world incidence are not feasible.

Diagnostic evaluation requires a multimodal approach with high clinical suspicion and either a transthoracic and a [transesophageal echocardiography](#) or a pulmonary venous phase CT scan or gadolinium-enhanced MRI [venography](#). In agreement with our report, \dot{V}/\dot{Q} mismatch on [scintigraphy](#) has also been described in 21 cases with severe RFCA-related stenosis.

No guidelines are available to inform treatment decisions, an issue that is further perplexed by the fact that suboptimal management may lead to deleterious complications such as progression to total [pulmonary vein occlusion](#), pulmonary hypertension/right ventricular failure, peripheral embolism, massive hemoptysis, and parenchymal damage. In cases of severe luminal stenosis (defined as > 70% narrowing on CT scan), pulmonary artery stenting is superior to [balloon angioplasty](#) in terms of patency rate (27%-33% vs 56%-72%). [Embolectomy](#) can be performed in refractory thrombosis when vessel wall stricture does not adequately explain flow defects. [Pulmonary resection](#) should be reserved for patients with massive hemoptysis and parenchymal necrosis.

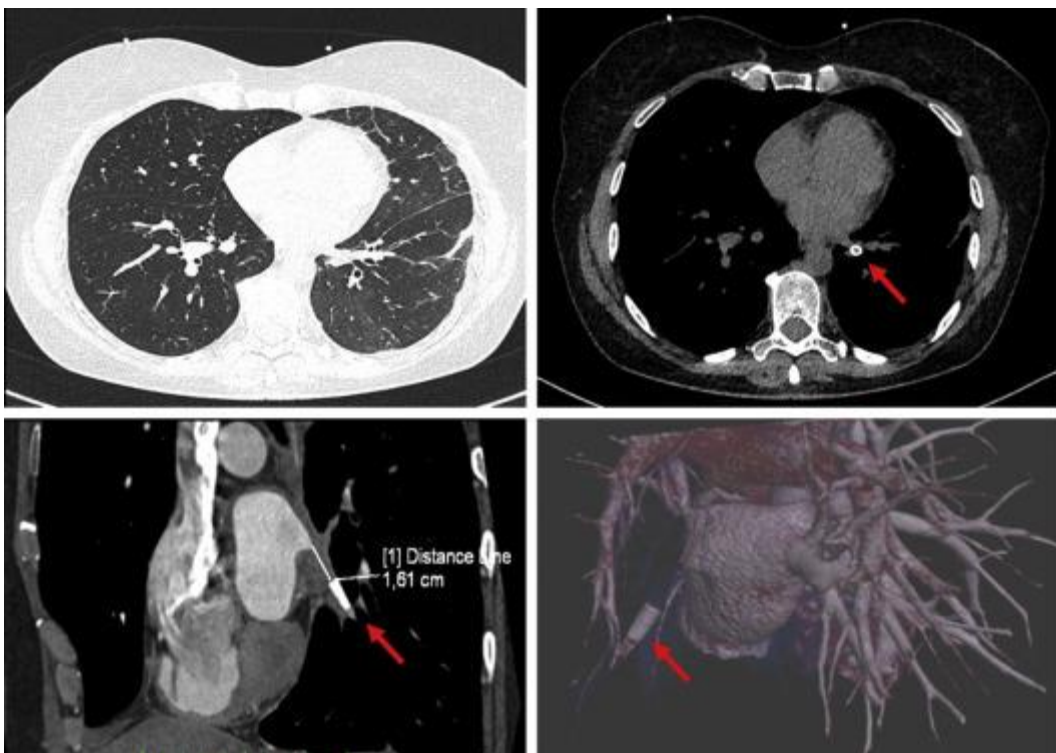
Taken together, clinical suspicion of post-RFCA PVT relies on clinician vigilance. [Transthoracic echocardiography](#), pulmonary venous phase CT scan, and gadolinium-enhanced MRI venography are viable diagnostic methods. No well-established treatment guidelines for post-RFCA PVT are currently available. In the absence of contraindications, systemic [anticoagulation](#) is advised. Invasive procedures are considered for severe disease and life-threatening complications. Prompt diagnosis is a prerequisite for preventing baneful [sequelae](#).

Clinical Course

The diagnosis of post-RFCA PVS/PVT was envisaged in light of the history of RFCA, the temporal onset of symptoms, the [lung scintigraphy](#) defect, and the prior exclusion of other alternative causes. Infection can be readily ruled out in the absence of fever, markedly elevated acute-phase reactants, response to antibiotic therapy, and microbiological evidence from biological fluid analysis. No radiological or cytological findings in favor of malignancy were present. Pulmonary embolism can be omitted from the differential diagnosis because no filling defects were found on [CT pulmonary angiogram](#). Serum autoantibodies were within normal limits, and

rheumatological consultation corroborated that at present no autoimmune disease associations exist despite pericardial/pleural involvement and initial response to corticosteroids.

As soon as the outcome of the venous phase CT scan confirmed the diagnosis, therapeutic dosage of low-molecular-weight heparin was initiated while corticosteroids were tapered off. The patient was then immediately referred for embolectomy and transcatheter stenting of the left inferior pulmonary vein. One month after successfully undergoing the operation, the patient showed complete resolution of symptoms and [radiological findings](#) during the follow-up visit at the outpatient clinic ([Fig 6](#)).



1. [Download: Download high-res image \(281KB\)](#)

2. [Download: Download full-size image](#)

Figure 6. CT scan after [thrombectomy](#) and stenting of the of left inferior pulmonary vein (red arrow), showing absorption of the pleural effusion, with disappearance of the lobar consolidation.

Abstract

Background

[Immunotherapy](#) has become a critical class of [anticancer therapy](#) in recent years, functioning by releasing brakes on the immune system that ultimately results in [immune cell](#) activation which eliminates [cancer cells](#). Immune related [adverse events](#) (IRAEs) are a specific type of adverse event described in patients taking checkpoint inhibitor immunotherapy which results from unrestrained immune activation. Immune related [pericardial effusion](#) has been described however has not been comprehensively characterized. Here, we present the most extensive report to date detailing this adverse event.

Methods

We queried our [medical record](#) system to retrospectively identify patients on checkpoint inhibitor therapy for lung cancer who subsequently developed [pericardial effusion](#). We analyzed the clinical and radiographic characteristics, prior therapies, treatment for the effusion, and outcomes in patients with immune related [pericardial effusion](#) and compared them to similar patients with [pericardial effusion](#) not attributable to checkpoint inhibitor therapy.

Results

Our data demonstrate that most of these pericardial effusions were small and not clinically significant. The majority were successfully treated with steroids or resolved spontaneously. Anti-PD-1 inhibitors were the most common checkpoint inhibitor preceding pericardial effusion, and a significant number of patients who went on to develop IRAE pericardial effusion previously had treatment with [carboplatin](#) for their cancer.

Conclusions

These data suggest that IRAE pericardial effusion is not a clinically significant adverse event however it sometimes leads to permanent discontinuation of checkpoint inhibitor therapy which is not necessary.

Introduction

Lung cancer is the leading cause of cancer death and the second most common cancer in both men and women.¹ It is commonly divided into small-cell and non-small-cell subtypes, with non-small cell representing approximately 85% of cases.^{2., 3., 4.} Prior to the advent of immunotherapy, treatment for non-small-cell lung cancer (NSCLC) was comprised of surgery for stage I and II disease with adjuvant chemotherapy for stage II, and chemotherapy for stage II and IV disease.⁵ Radiation therapy is also commonly used in treatment.^{6., 7.} A comprehensive trial evaluating four chemotherapeutic regimens for treatment of patients with advanced NSCLC found an overall survival of 7.9 months and a response rate of 19% for all groups.⁸ Furthermore, their data showed no difference in outcomes in patients treated in the experimental regimens compared to the reference regimen of carboplatin and paclitaxel.⁸

The advent of targeted therapy represented a paradigm shift in the treatment of lung cancer. Numerous therapies targeting specific driver mutations have been developed; though addressing only a small subset of patients, these therapies have contributed to substantially improved outcomes for patients carrying these actionable mutations.^{9., 10.} Specific targets include EGFR^{11., 12., 13.} and ALK,^{14., 15.} as well as less common mutations such as BRAF for which a therapy was developed to treat a different type of cancer.¹⁶

Checkpoint inhibitor therapy can be used to treat a broader patient population, and at the molecular level functions by targeting cell signaling proteins involved in immune recognition and modulation. Clinical trials of these drugs in patients with non-small-cell lung cancer have demonstrated dramatic improvements in survival. In 2015, PD-1 inhibitor nivolumab was approved for use in NSCLC with greater than 50% PD-L1 expression and no EGFR or ALK mutation. A head-to-head trial of nivolumab versus docetaxel demonstrated improved overall survival of 12.2 months and 50.5% one year overall survival with nivolumab compared to 9.4 months overall survival and 39.0% one year survival with docetaxel (CheckMate 057, [NCT01673867](#)).^{17., 18.} Further trials optimizing combinatorial immunotherapy have demonstrated that a combination of nivolumab and anti-CTLA-4 inhibitor ipilimumab resulted in

a 23.2 month response compared to 6.2 months with chemotherapy.¹⁹ Despite the success of this combination, data has demonstrated an adverse event rate greater than 20%.¹⁹

Adverse events occurring as a result of immune system overactivation in the context of immunotherapy are known as Immune Related Adverse Events (IRAEs). Immune system checkpoints are necessary to balance appropriate immune activation when needed versus overabundant response leading to excessive microenvironmental damage.²⁰ Animal studies have shown that disruption of the molecular pathways responsible for immune checkpoints can lead to overactivation of the immune system and severe organ damage associated with loss of self-tolerance.^{21., 22.} IRAE pneumonitis and pericardial effusion are established manifestations of immune hyperactivity in the setting of immunotherapy and are diagnosed on chest CT.

IRAE pneumonitis has been extensively characterized radiographically.^{23., 24., 25.} Importantly, research has shown that grade 1–2 pneumonitis is associated with checkpoint inhibitor efficacy, likely attributable to the underlying mechanism of overabundant immune response mediating both drug efficacy and pneumonitis.²⁶ IRAE pericardial effusion was initially thought to be a rare complication of checkpoint inhibitor therapy but increased use of these agents have shown a growing number of cases, with presentations that can be severe enough to result in cardiac tamponade.^{27., 28., 29.} To our knowledge, studies of IRAE pericardial effusion have been limited to case reports and case series, limiting clinical and radiographic characterization. Here, we present a cohort of patients with IRAE pericardial effusion after treatment with immunotherapy so as to characterize the associated clinical and radiographic characteristics to gain insight into the clinical correlates of this adverse event.

Data collection

We obtained Internal Review Board approval (IRB AAAS7350 approved 10/29/2020) to study the effects and side effects of immunotherapy. We queried the hospital medical record system *Epic* for patients who had been administered checkpoint inhibitor therapy including ipilimumab, nivolumab, pembrolizumab, atezolizumab, and durvalumab. We also identified patients who had been administered targeted therapies, including gefitinib, erlotinib, afatinib, dacomitinib, osimertinib, crizotinib, and ceritinib.

Demographic and clinical characteristics of patients with IRAE pericardial effusion

We first sought to characterize the demographic and clinical characteristics of patients treated with checkpoint inhibitor therapy who developed pericardial effusions compared to control patients. Table 1 summarizes these characteristics. Patients with IRAE pericardial effusion did not differ significantly in age, smoking history, or type of cancer. Significantly more patients with pericardial effusion secondary to checkpoint inhibitor use were male ($p = .000488$) and had diabetes mellitus (p)

Discussion

Immunotherapy has become an important pillar of anticancer therapy over the last decade. With the increasing number of patients on these drugs, it is important for providers to fully understand the associated adverse events so they can appropriately weigh the risks and benefits. IRAEs are specific to immunotherapy agents due to the common the mechanism of action of therapy.³¹ Here, we provide the most comprehensive characterization of IRAE pericardial effusion to our knowledge.

Importantly, lung

Conclusions

Patients with IRAE pericardial effusion did not differ significantly in demographic or clinical characteristics from patients with lung cancer who developed pericardial effusion from other etiologies. Prior studies have described large pericardial effusions with significant clinical implications,^{27., 28., 29.} however our data suggest that these cases are the exception and that the majority of cases are not clinically significant. A minority of patients developed symptoms attributable to their

Methods

We obtained pleural effusion samples from a patient with bilateral effusions after esophagectomy with anastomotic leakage, avoiding contact with alcoholic disinfectants. Ethanol and glucose were measured with Roche Cobas (Roche Diagnostics, Mannheim, Germany). To analyze congeners, we performed gas chromatography (Perkin Elmer Turbo Matrix [Waltham, Mass, USA] and Clarus 500 [Oberkochen, Germany]). Pleural fluid was incubated in culture bottles (BD Bactec, Franklin Lakes, NJ, USA). Species were

Results

The left-sided pleural effusion was of a clear amber color. The right-sided effusion was of a dirty brownish color (Figure). In the right-sided effusion, yeasts were detected (Figure) and identified as *Candida albicans*. Ethanol was 0.5 g/L in the yeast-infected pleural fluid and 0.0 g/L in the non-infected pleural fluid and in the blood. Glucose was 9 mg/dL in the infected pleural fluid, and 137 and 110 mg/dL in the non-infected effusion and in the blood, respectively. In the culture bottle

Discussion

We have shown that yeasts can generate alcohol in a pleural effusion, making the chest a “barrel chest” in terms of function, not form. The reaction formula of alcoholic fermentation is $C_6H_{12}O_6 \rightarrow 2C_2H_5OH + 2CO_2$. Hence, under perfect conditions, 0.51 g of ethanol can be produced from 1 g of glucose. As glucose in pleural effusion depends on glucose concentration in blood (typically 0.75 to 1.1 g/L), ethanol concentration in pleural effusion is limited. The concentration measured here appears

Abstract

Background

Data regarding predictors of the outcome in patients with community-acquired complicated parapneumonic effusion (CPPE) or [empyema](#) are insufficient. The aim of the present study was to investigate the [prognostic factors](#) in these patients.

Methods

Patients with community-acquired pneumonia (CAP) were classified into a CPPE or [empyema](#) group and a control group. The patients with CPPE or empyema were further divided into longer and shorter length of stay (LOS) groups, and clinical variables and computed tomographic (CT) findings were compared between the 2 groups.

Results

Of outcome variables, LOS was significantly longer in the CPPE or empyema group than in the control group (13 days [interquartile range, 10–17 days] versus 8 days [6–12 days], $p < 0.001$), whereas 30-day mortality and in-hospital mortality were not significantly different between the 2 groups. Patients with CPPE or empyema were divided into shorter LOS (<14 days) and longer LOS (≥ 14 days) groups. [Pneumonia severity index](#) (PSI) class IV–V (odds ratio [OR], 2.79; 95% confidence interval [CI]: 1.35, 5.76; $p = 0.006$), increased attenuation of extrapleural fat (OR, 2.26; 95% CI: 1.06, 4.80; $p = 0.034$), and pleural microbubbles (OR 3.93; 95% CI: 1.03, 14.98; $p = 0.045$) were independent predictors for prolonged LOS in CAP patients with CPPE or empyema.

Conclusions

Increased attenuation of extrapleural fat and pleural microbubbles assessed with [CT](#) and PSI class IV–V independently predicted prolonged LOS in CAP patients with CPPE or empyema. These findings may be helpful to identify patients who need more intensive evaluation and intervention.

Introduction

Community-acquired pneumonia (CAP), a common acute infectious disease, is the leading cause of hospitalization and mortality worldwide.¹ Pleural effusion is detected in approximately 20% of patients with CAP on chest radiograph^{2,3} and more frequently in 30%–54% on ultrasonography.^{4,5} Similarly, for the detection of pleural effusion, chest computed tomography (CT) is more sensitive than chest radiography.⁶ In addition, chest CT scan is a better modality to determine the extent of pleural infection.⁶ Several CT findings suggestive of CPPE or empyema have been proposed.^{7,8} Many CAP patients with parapneumonic effusion (PPE) may improve with antimicrobial treatment alone, but approximately 30% of those with PPE requiring pleural drainage are considered to have complicated PPE (CPPE) or empyema.^{3,9} The differentiation of CPPE or empyema from uncomplicated PPE is pivotal in determining the therapeutic strategy in patients with PPE. To this end, clinical, laboratory, and chest radiographic parameters have previously been provided.^{2,3,10}

The presence of pleural effusion, as evidenced by one of the factors of pneumonia severity index (PSI) for CAP, is an important factor for the treatment and clinical outcomes of CAP.¹¹ In terms of treatment success or failure for CPPE or empyema, the absence of pleural fluid purulence predicted success with medical therapy,¹² and loculation and pleural fluid leukocyte count of $\leq 6,400/\mu\text{L}$ were independent predictors for treatment failure.¹⁰ Hospital stay has been used as an outcome variable in several studies for CPPE or empyema.^{9,13,14} Prolonged hospital stay in patients with CPPE or empyema was associated with a variety of clinical and microbiological factors, such as comorbidities,¹³ fever,⁹ lower PaO₂,⁹ higher neutrophil fraction in blood,⁹ high pleural fluid levels of lactate dehydrogenase (LDH),¹⁴ purulent pleural fluid,^{13,14} culture-negative pleural effusion,¹⁴ or identification of microbe in pleural fluid;⁹ some predictors were conflicting in different studies. Predictors for prolonged hospital stay in patients with CPPE or empyema undergoing pleural drainage remain to be elucidated.

Among CT findings suggestive of CPPE or empyema, some variables are considered to be associated with the extent of inflammation infiltrating chest wall and the stage of pleural infection.^{15,16} Therefore, we hypothesized that these CT parameters might contribute to the prediction of the prognosis in patients with CPPE or empyema. This study aimed to investigate

which CT findings could distinguish CPPE or empyema from uncomplicated PPE and predict the prognosis of CPPE or empyema.

Study population and design

Patients who had been hospitalized, diagnosed, and treated with CAP between January 2011 and July 2019 at the Kyungpook National University Hospital, a tertiary referral center in Daegu, South Korea, were included in this retrospective study. Clinical data were collected from the electronic medical records. CAP was diagnosed based on the following criteria: symptoms or signs suggestive of lower respiratory tract infection plus new radiological abnormalities on chest radiograph or CT, which

Clinical characteristics of CAP patients with or without CPPE or empyema

Of the 2404 patients who were diagnosed as having CAP during the study period, 1705 patients with enhanced chest CT were enrolled after excluding 699 patients without enhanced chest CT scan (Fig. 2). Of the 1705 patients, 692 (41%) had pleural effusion on their CT scans, and 225 of the 692 patients (33%) were assigned to the CPPE or empyema group. The control group included 1480 patients who did not fulfill the diagnostic criteria of CPPE or empyema.

The patients with CPPE or empyema were

Discussion

Similar to previous studies,^{9,13,14} CAP patients with CPPE or empyema exhibited significantly longer LOS than those without CPPE or empyema. CAP patients with CPPE or empyema were divided into shorter and longer LOS groups. In multiple logistic regression analysis, PSI class IV–V and the 2 CT findings were independent factors for predicting prolonged hospitalization, suggesting that chest CT scan may contribute to enhancing the prediction of LOS in CAP patients with CPPE or empyema.

A previous

Conclusions

In conclusion, along with PSI class IV–V, increased attenuation of extrapleural fat and pleural microbubbles assessed with CT can be used to predict prolonged hospital stay in CAP patients with CPPE or empyema treated with tube drainage. These predictors can be assessed easily at presentation, and help to identify patients who are expected to experience prolonged hospital stay. Thus, careful evaluation of pleura and chest wall on chest CT is necessary in patients with parapneumonic effusion to

Case Presentation

A 52-year-old man was referred to our hospital for [cough](#), fever, [chest pain](#), and progressive dyspnea. He has worked as a full-time security staff at a community center and was in a normal state of health until 11 months prior to referral when he began experiencing cough, expectoration, a high-grade fever (up to 39.7°C), [chills](#), and left [chest pain](#). He visited the local hospital several times with suspected lung cancer. [Bronchoscopy](#) showed chronic inflammatory changes in his bronchi. He was given a course of antibiotics, but his fever had not subsided. The patient had visited a bamboo rat farm and consumed bamboo rat meat one year previously. He had never smoked.

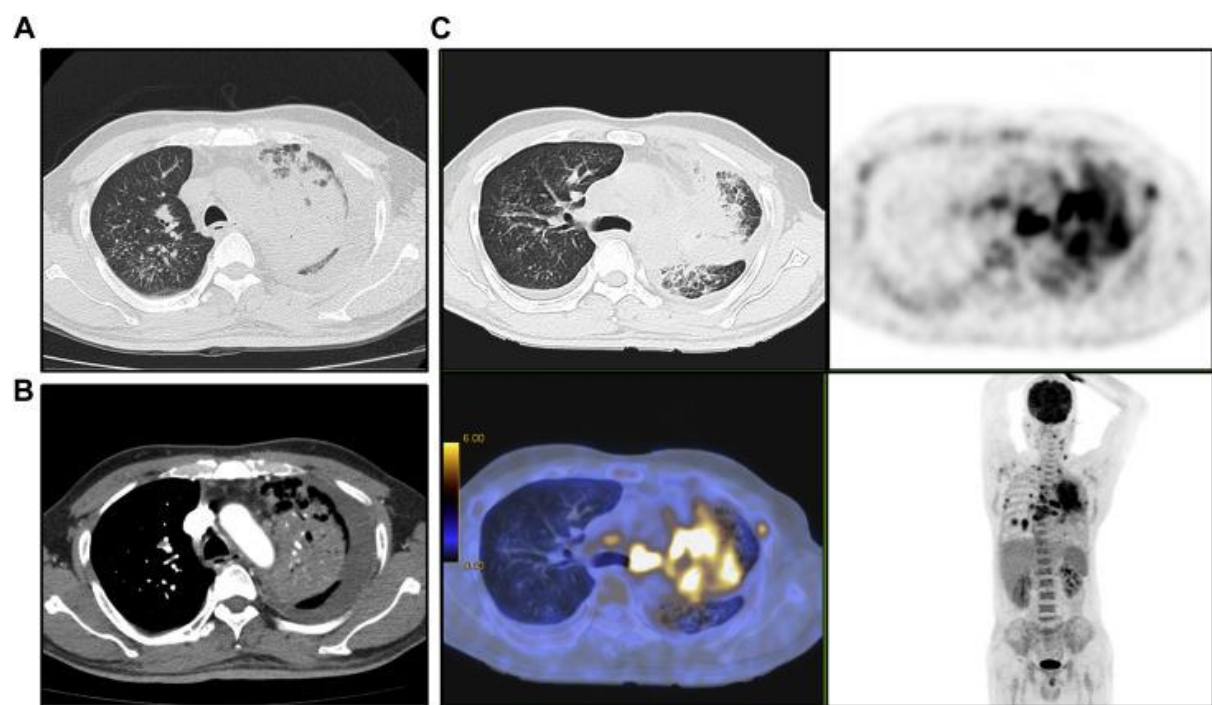
Physical Examination Findings

Several lymph nodes with a maximum diameter of approximately 0.5 cm^2 were palpated in the left cervical region. There was tenderness in the third and fourth anterior ribs on the left side and the manubrium. Breath sounds were diminished markedly in the whole left lung. No other abnormalities were noted, including skin lesions.

Diagnostic Studies

A complete blood count revealed a WBC count of $19.67 \times 10^9/\text{L}$ with 83.6% neutrophils and hemoglobin at 7.5g/dL. T-cell subset counts were all normal, and HIV antibodies were negative. Acid-fast bacilli, tuberculin test, (1-3)- β -D-glucan, and serum tumor markers were all negative or within normal limits. Blood and sputum cultures were negative for bacteria and fungi.

A chest CT revealed left lung atelectasis, enlarged mediastinal lymph nodes, and a left-sided pleural effusion (Fig 1A, B). A PET-CT scan indicated increased uptake of 18F-fluorodeoxyglucose with a maximum standardized uptake value of 11.4 in the left lung and multiple nodules in both lungs. There was an increase in glucose metabolism in the lymph nodes of the neck, mediastinum, abdominal cavity, and retroperitoneum, and there were multiple osteolytic lesions in the sternum and ribs (Fig 1C).

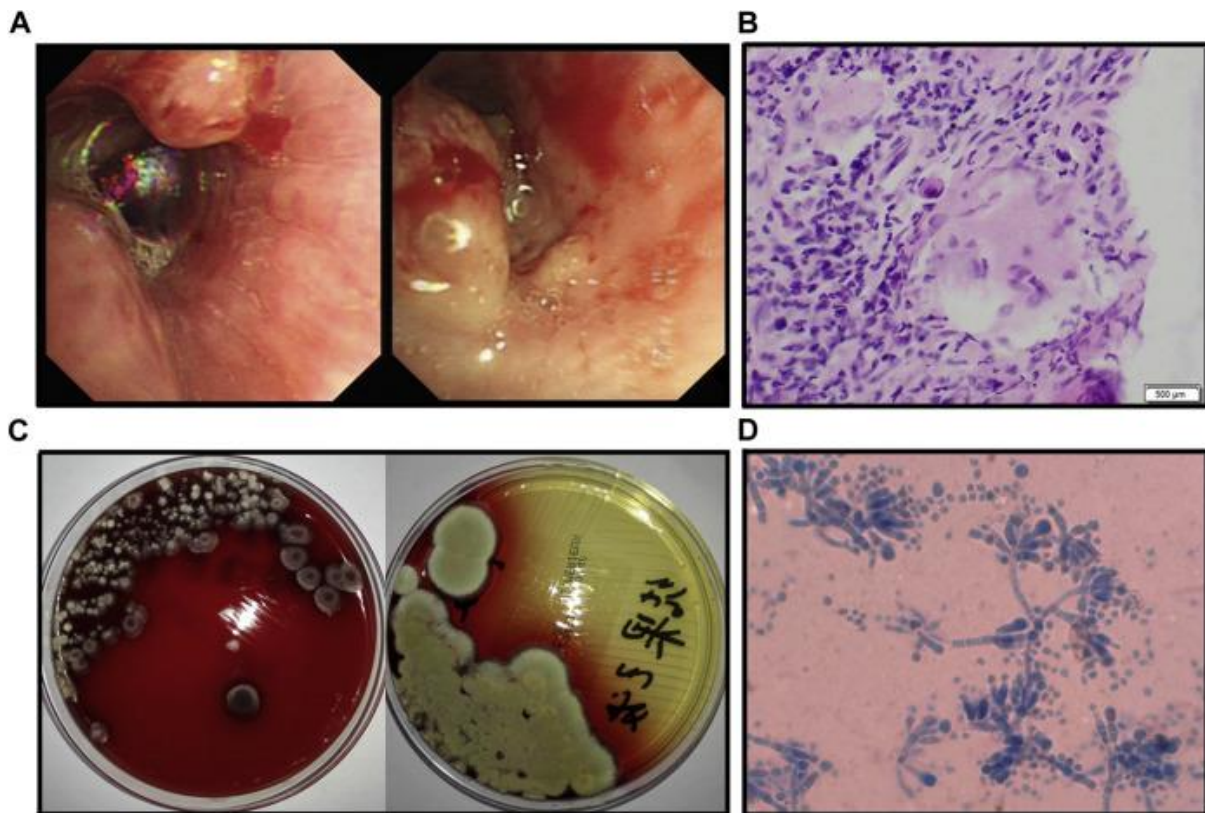


1. [Download: Download high-res image \(824KB\)](#)
2. [Download: Download full-size image](#)

Figure 1. A-C, Chest CT scan and PET-CT scans. A and B, Chest CT revealed pleural effusion and atelectasis in the left lung field and pleural effusion in the left thoracic cavity. C, PET-CT imaging revealed increased uptake of 18F-fluorodeoxyglucose with maximum standardized uptake values of 11.4 in left lung field, 11.3 in the lymph nodes, and 7.1 in bone.

Bronchoscopy revealed multiple submucosal nodules in the left principal bronchi (Fig 2A). Pathologic examination revealed congestion and edema in the submucosa with massive infiltration by lymphocytes and a granulomatous lesion (Fig 2B). Culture of the pleural fluid sample indicated a *Penicillium* species that exhibited temperature-dependent dimorphic growth

([Fig 2C](#)). Sausage-shaped yeast-like cells with septate hyphae (from culture at 25°C) were observed under a microscope ([Fig 2D](#)).



1. [Download: Download high-res image \(583KB\)](#)
2. [Download: Download full-size image](#)

Figure 2. A, Bronchoscopy revealed multiple submucosal nodules in the lower-left principal bronchi. B, The pathologic examination results of bronchoscopy showed congestion and edema in the submucous with massive infiltration by lymphocytes and a [granulomatous lesion](#). C, Fungal culture of pleural fluid during yeast phase at 37°C with no production of red pigment and [mycelia](#) obtained at 25°C with the production of red pigment. D, Sausage-shaped yeast-like cells with septate hyphae (from 25°C culture) were observed under the microscope (Medan staining, ×400).

What is the diagnosis?

Diagnosis: Disseminated [Talaromyces marneffei](#)

Discussion

Also called [Penicillium marneffei](#), *T marneffei* is a thermally [dimorphic fungus](#) that can cause severe [mycosis](#) in [immunocompromised patients](#), such as those with HIV, autoimmune disease, or [hematologic malignancy](#) and those who have undergone [organ transplantation](#). However, it rarely is observed in immunocompetent individuals. *T marneffei* infection therefore is considered an [opportunistic infection](#). It is prevalent mainly in Southeast Asia, which includes Thailand, Vietnam, Northeastern India, Southern China, Hong Kong, Taiwan, Laos, Malaysia, Myanmar, and Cambodia.

In China, [epidemiologic studies](#) show 87.72% of patients with *T marneffei* infection are HIV positive, and 8.5% are without any documented underlying diseases. Bamboo rats are the natural hosts of *T marneffei*. *T marneffei* is not only isolated from the organs of bamboo rats but also the surrounding environments of their burrow, such as soil. People, especially those with immunodeficiency, who are exposed to environments surrounded with bamboo rats are particularly vulnerable to *T marneffei*. Therefore, a history of residing or traveling in an endemic area and exposure to environments where bamboo rats live may well serve as an important clue/heuristic for a physician to diagnose *T marneffei*.

The pathogenesis of *T marneffei* infection is yet to be fully understood. Inhalation of [conidia](#) from the environment is a key pathway to infection. The [conidia](#) then proliferate in macrophages and disseminate to other internal organs through the [reticuloendothelial system](#), especially the lungs, bone marrow, bone, skin, lymph nodes, spleen, liver, and reticuloendothelial tissues. The most common symptoms of *T marneffei* infection are fever, [cough](#), [skin lesions](#), [generalized lymphadenopathy](#), and [hepatosplenomegaly](#), along with local abscesses and [osteolytic lesions](#).

The clinical manifestations of *T marneffei* infection are different in HIV-negative and HIV-positive patients. Osteolytic lesions are common in HIV-negative patients, but diagnosis is often delayed and misdiagnosed as [malignancy](#), TB, or [histoplasmosis](#). Osteolytic lesions typically occur at sites of [neutrophil](#) accumulation. The accumulation of [neutrophils](#) and the release of [proteolytic enzymes](#) lead to [osseous tissue](#) lysis, liquefaction, and necrosis. In HIV-negative patients, [WBC counts](#), neutrophils, and lymphocytes are increased significantly, and the ratio of CD4+/CD8+ is >0.5. The severity of the disease depends on the host's degree of [immunosuppression](#).

The [mortality rates](#) for patients not infected with HIV and those who are infected are 27.7% to 29.4% and 20.7%, respectively, which might be related to an initial misdiagnosis in HIV-negative patients who ultimately were found to have *T marneffei*. Alternatively, the diagnosis may be delayed due to a lack of clinical suspicion.

Microbiologic culture is the gold standard for diagnosing *T marneffei* infection. *T marneffei* is the only known *Penicillium* species that exhibits temperature-dependent dimorphic growth. Yeast-like cells are found in the culture at 37°C. The fungi outside the host cells are elongated, often curved, and sausage-like, and they have clear central septi. At 25°C, the fungus is mycelia-like and produces a characteristic red pigment that diffuses into the culture medium. Secreted enzymes that are expressed by [mycelia](#) and yeast are linked to virulence in *T marneffei*.

Fungal culture provides direct and reliable evidence for the diagnosis of *T marneffei*. Clinical specimens that are used commonly for culture include bone marrow aspirate, [skin biopsy](#) specimens, [lymph node biopsy](#) specimens, blood, [sputum](#) specimens, tissue, urine, stool, [pleura](#), [cerebrospinal fluid](#), pleural fluid, [ascites](#), and [pericardium](#). However, a disadvantage of this method is that the culture of fungi generally takes approximately three to four days, which frequently results in the delay of appropriate [antifungal therapy](#). In addition, the sensitivity of fungal culture from blood can be low (76.7%) in HIV-positive patients and is only 47.1% in HIV-negative patients. Currently, there are no reliable commercial kits for rapid testing of *T marneffei*. Nowadays, pathologic diagnosis is of extreme importance in *T marneffei* diagnosis. After being stained with [hematoxylin](#) and [eosin](#), periodic acid-Schiff, or [Grocott methenamine silver stain](#), *T marneffei* can be seen in macrophages or [histiocytes](#).

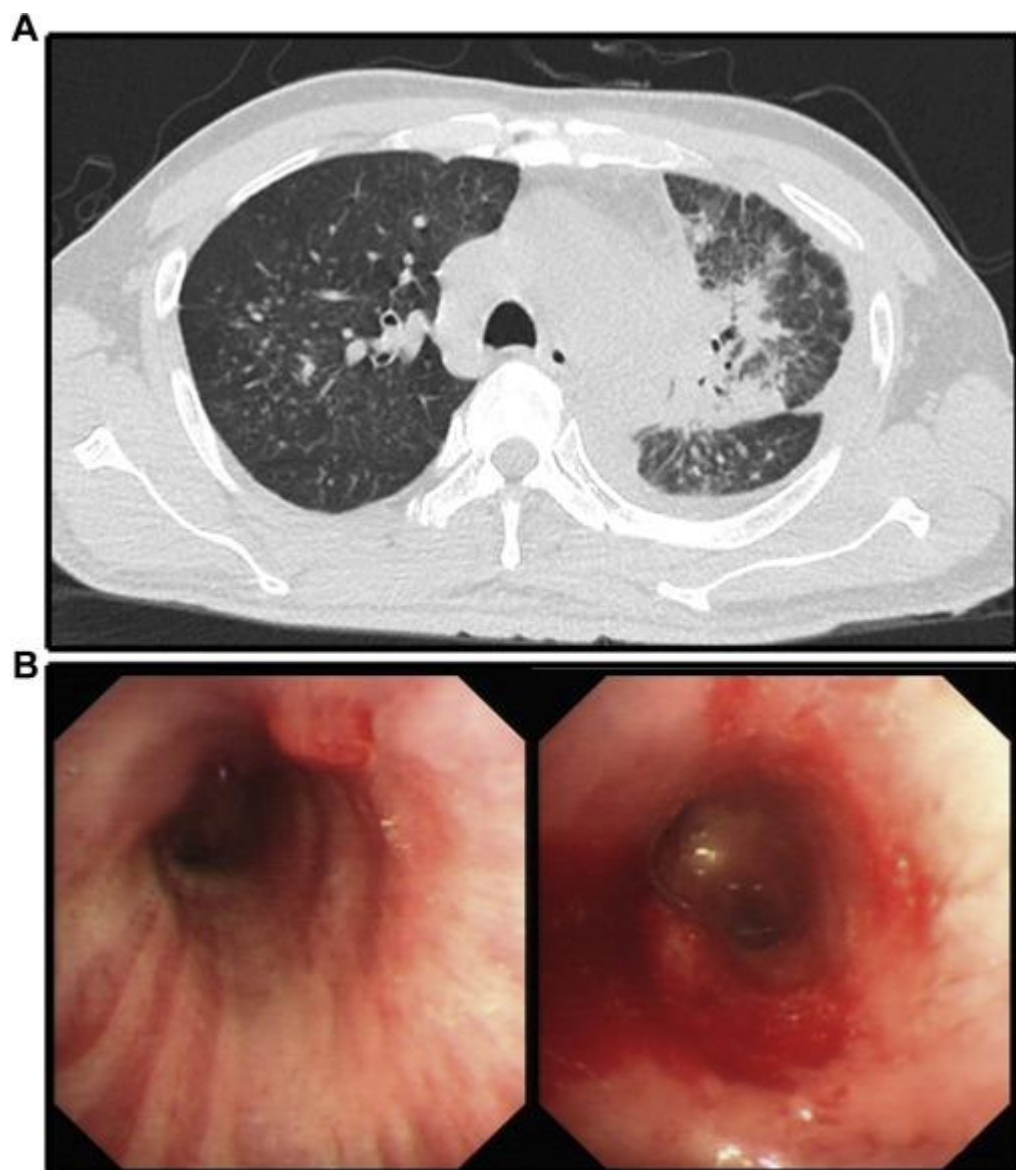
There are three main pathologic changes that occur in tissues that are infected with *T marneffei*: [granuloma](#), purulent inflammation, and reactive necrotizing inflammation. Most HIV-

positive patients with *T marneffei* infection show reactive necrotizing inflammatory changes; those with normal immune function show granulomatous lesions and suppurative reactions.

Currently, there is no uniform standard for antifungal treatment of *T marneffei* infection in HIV-negative patients, especially in cases with osteolytic lesions. The drugs most commonly used for antifungal therapy of *T marneffei* are amphotericin B, voriconazole, and itraconazole, which show good therapeutic effects. However, despite prolonged antifungal treatment, most patients, regardless of their HIV status, relapse after several months or years.

Clinical Course

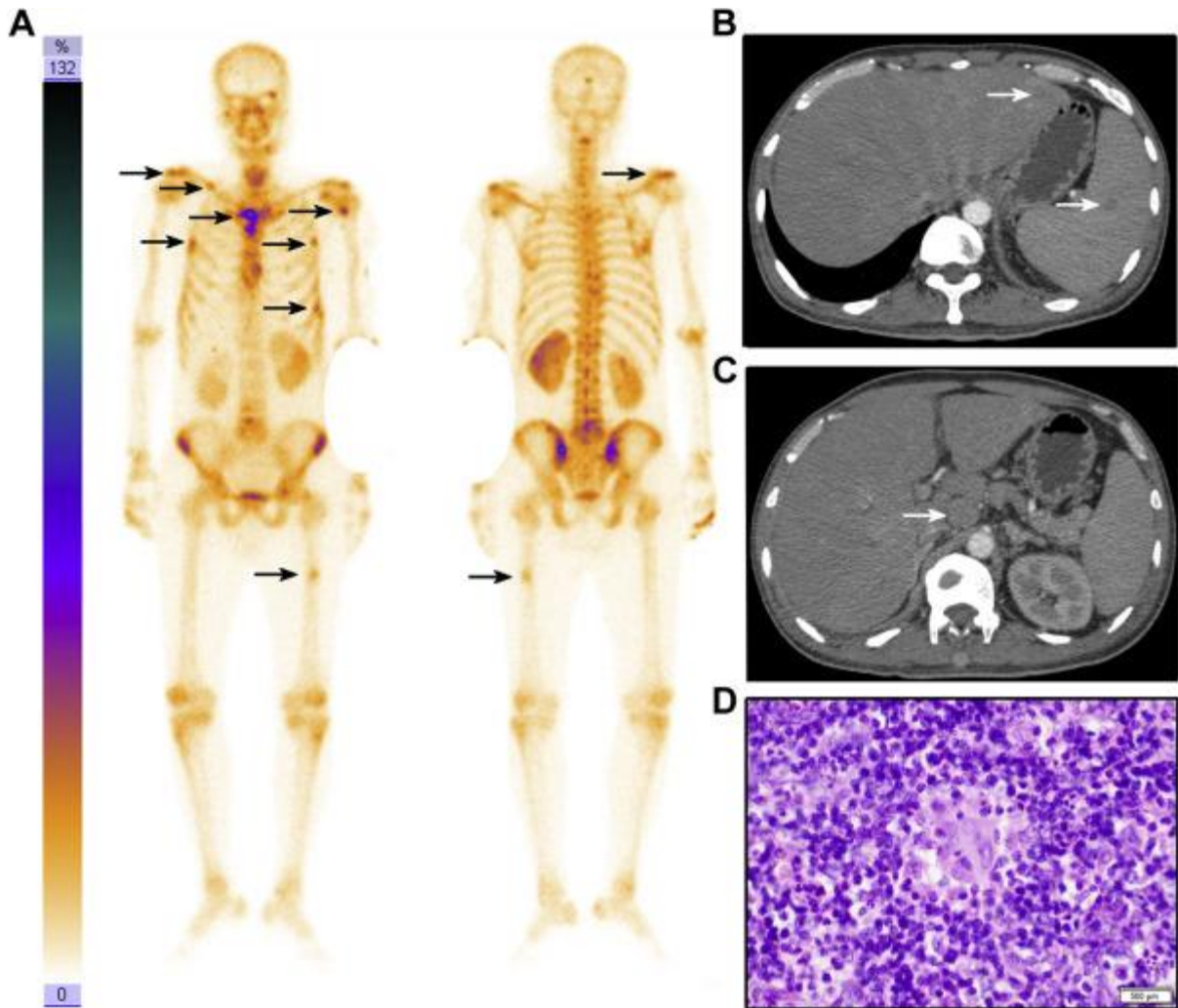
In our case, after the patients had received voriconazole treatment for one month, the results of lung CT ([Fig 3A](#)) and bronchoscopy ([Fig 3B](#)) showed improvements. Unfortunately, the patient still showed osteolytic lesions ([Fig 4A](#)) and systemic lymphadenopathy. New lesions were found in the liver, spleen, and abdominal lymph nodes ([Fig 4B, C](#)), and there was still intermittent fever. The patient eventually died after receiving antifungal therapy for four months. This outcome is considered to be related to the delayed diagnosis and treatment that resulted in its systemic spread.



1. [Download: Download high-res image \(389KB\)](#)

2. [Download: Download full-size image](#)

Figure 3. A-B, Chest CT and submucosal nodules in bronchi of the patient decreased in size after receiving antifungal treatment for one month. A, Chest CT reveals that the pleural effusion and left lung atelectasis had improved. B, Bronchoscopy shows that multiple submucosal nodules in the lower-left principal bronchi were smaller than before.



1. [Download: Download high-res image \(530KB\)](#)

2. [Download: Download full-size image](#)

Figure 4. A, [Bone scan](#) shows abnormally active [bone lesions](#) throughout the body. B and C, Abdomen CT reveals new lesions in the liver, spleen, and abdominal lymph nodes (arrows). D, Histopathologic findings of [cervical lymph nodes](#) reveal lymphatic sinus dilatation with massive infiltration by neutrophils and granuloma formation in the cortex.

Clinical Pearls

- 1.

*Clinicians should be attentive to both the symptoms and travel histories that are characteristic of a *T marneffei* infection. Additionally, a diagnosis of a *T marneffei* infection should be considered*

if patients continue to experience symptoms such as [cough](#), fever, [lymphadenopathy](#), and [osteolysis](#), despite being HIV-negative and having completed their course of antibiotics from the previous diagnosis.

- 2.

*Microbiologic culture and pathologic evidence are the key to *T marneffei* diagnosis. If a patient is suspected of being infected with *T marneffei*, the cultures of [sputum](#), [BAL fluid](#), and/or [pleural effusion](#) should be obtained.*

- 3.

**T marneffei* infection is characterized by a high rate of recurrence. Patients should continue to receive [antifungal](#) treatment until clinical symptoms of *T marneffei* infection have waned, cultures of *T marneffei* are negative, and radiographic abnormalities are resolved.*

Case Presentation

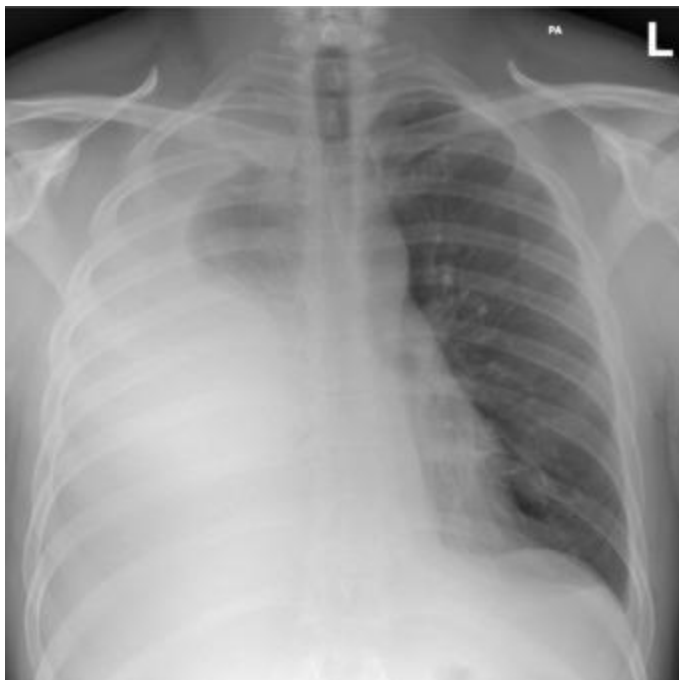
A 33-year-old white man presented to the ED with 1-month history of worsening dyspnea. He experienced gradual onset of right-sided scapular pain and shortness of breath on exertion that progressively worsened over the course of 1 month. He had a mild nonproductive [cough](#) and intermittent subjective fevers and reported weight loss of approximately 2 kg over 1 month. He had a history of two episodes of [acute pancreatitis](#) that was thought to be autoimmune in origin. He was a never smoker; he denied [illicit drug](#) use or recent alcohol consumption. He had no known TB exposure, but his mother had a history of [sarcoidosis](#).

Physical Examination Findings

On examination, his [oxygen saturation](#) was 97% on room air; his heart rate was 96 beats per minute; his respiratory rate was 20 breaths per minute; his temperature was 36.2°C, and his BP was 135/85 mm Hg. There was no evidence of respiratory distress. Examination of the chest revealed reduced breath sounds in the right hemithorax with associated stony dullness to percussion. The abdomen was soft, with no tenderness, guarding, or palpable masses. There was no palpable [lymphadenopathy](#). The remainder of the physical examination was unremarkable.

Diagnostic Studies

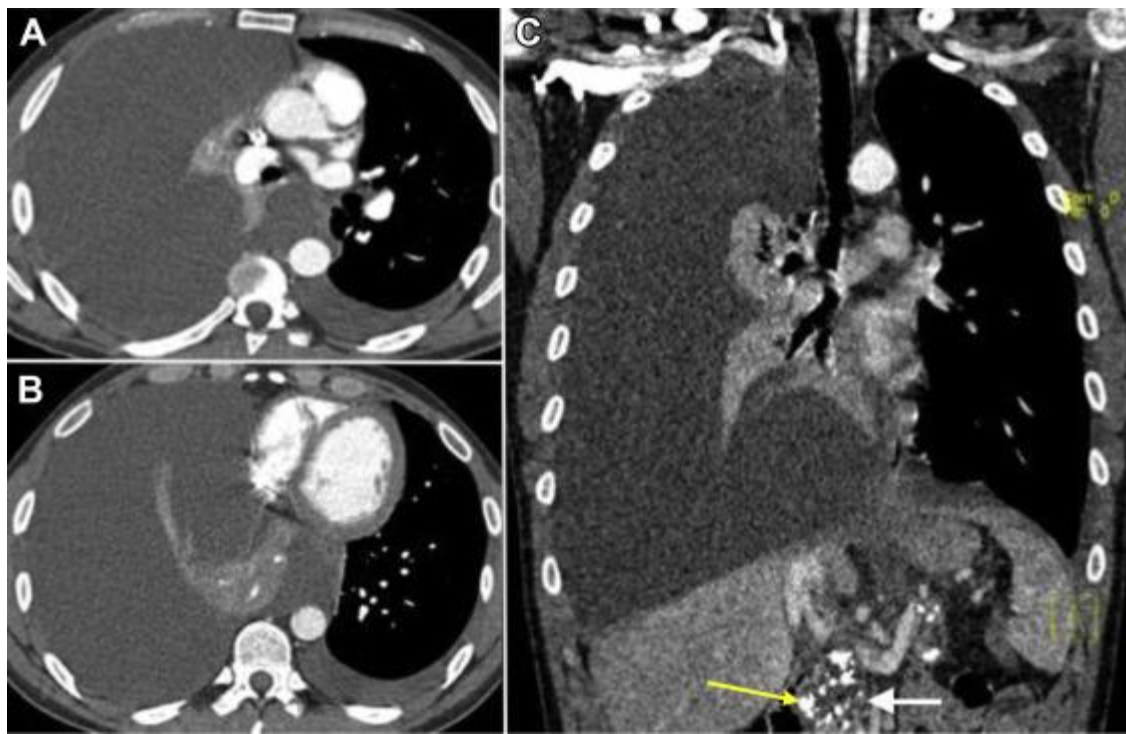
[Chest radiograph](#) shows a large right-sided [pleural effusion](#) (Fig 1). Laboratory results were as follows: WBC count, 9.2×10^9 cells/L; [eosinophil](#) count, 0.8×10^9 cells/L (normal range: 0-0.5 $\times 10^9$ cells/L); platelet count, 500×10^3 cells/ μ L; C-reactive protein, 12 mg/dL (normal range: 0-0.5 mg/dL); [alanine aminotransferase](#), 110 units/L (normal range: 9-59 units/L); aspartate aminotransferase, 61 units/L (11-34 units/L). Serum [amylase](#) was markedly raised 1784 units/L (normal range: 28-100 units/L), D-dimer, >10 [fibrinogen](#) equivalent unit/mL (normal range: 0-0.5 [fibrinogen](#) equivalent units/mL).



1. [Download: Download high-res image \(181KB\)](#)
2. [Download: Download full-size image](#)

Figure 1. Chest radiograph at presentation demonstrates a large right-sided pleural effusion with subtotal right [lung collapse](#).

Chest CT imaging was performed ([Fig 2](#)). This demonstrated a large right-sided [pleural effusion](#) with near complete collapse of the right lung. There was no visible [pleural thickening](#) or enhancement. A chest drain was inserted under ultrasound guidance. Pleural fluid was serosanguinous in appearance, and laboratory analysis revealed the following results: total protein, 24 g/L (serum protein, 78 g/L); [lactate dehydrogenase](#), 382 units/L (serum [lactate dehydrogenase](#), 400 units/L); glucose, 6.1 mmol/L; [amylase](#), 7500 units/L; and WBC count, 1,300 cells/mL (30% [polymorphs](#) and 70% lymphocytes). No organisms were seen on [Gram stain](#), and no acid-fast bacilli were seen on [auramine](#) stain. No malignant cells were seen, only benign [mesothelial cells](#) and lymphocytes.



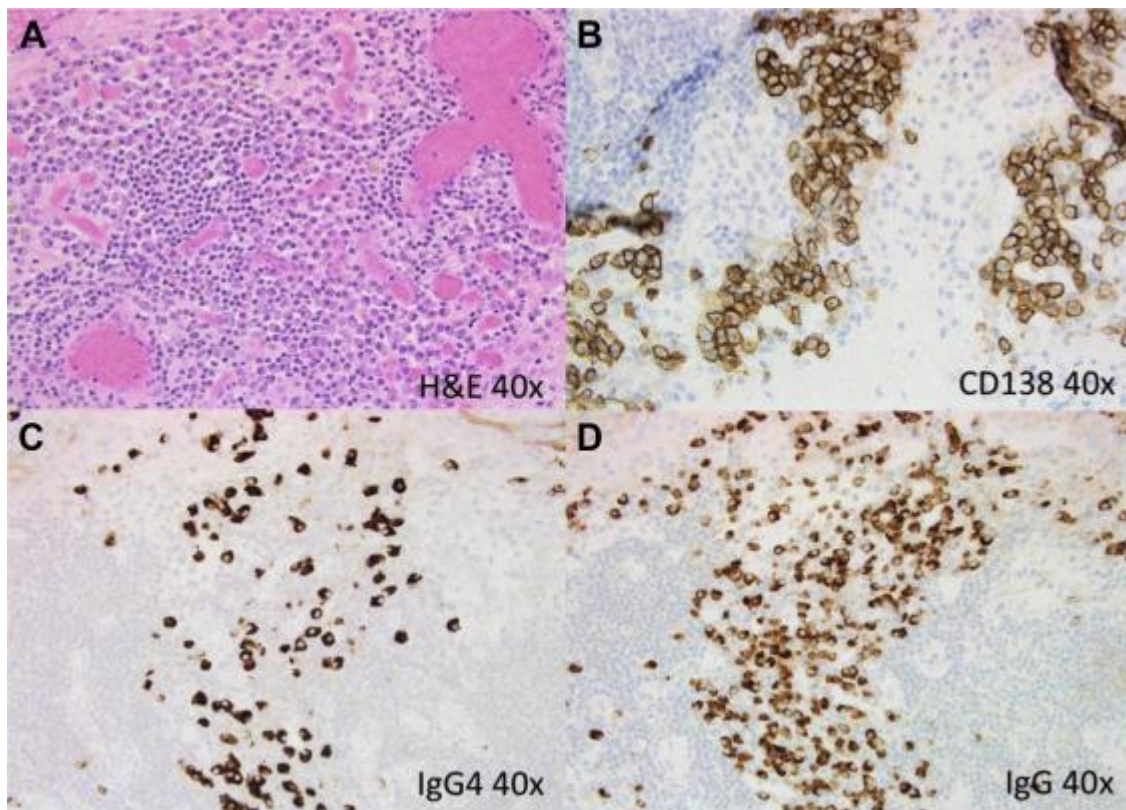
1. [Download: Download high-res image \(549KB\)](#)

2. [Download: Download full-size image](#)

Figure 2. A-C, Chest CT scan at presentation. A and B, Axial and C, coronal images from a CT thorax with IV contrast with a large right-side pleural effusion with almost complete right lung atelectasis, mild contralateral mediastinal shift, and a small left basal pleural effusion. There was no visible pleural thickening, nodularity, or enhancement. Multifocal pancreatic calcification (yellow arrow) with pancreatic duct dilatation is also shown (white arrow), which is consistent with chronic pancreatitis.

Magnetic resonance cholangiopancreatography revealed loss of pancreatic parenchymal volume with coarse calcifications most consistent with chronic pancreatitis. Given the patient's history of possible autoimmune pancreatitis, serum IgG4 was measured and was found to be elevated at 2.7 g/L (normal range, 0.039-0.864 g/L).

Pleural biopsies were performed via video-assisted thoracoscopic surgery. This revealed pleura with a prominent lymphoplasmacytic inflammatory infiltrate and mesothelial cell hyperplasia. Immunohistochemical studies demonstrated a population of cluster of differentiation 138 positive plasma cells that express IgG4, with >50 IgG4 positive plasma cells per high-power field ([Fig 3](#)) and an IgG4/IgG ratio of 47%.



1. [Download: Download high-res image \(1MB\)](#)
2. [Download: Download full-size image](#)

Figure 3. A-D, Histologic findings. A, Hematoxylin-eosin staining of histologic sections of pleural biopsy shows a prominent diffuse inflammatory infiltrate. B, Immunohistochemistry with the use of the plasma cell marker cluster of differentiation 138 shows that the infiltrate consists primarily of plasma cells. C, Immunohistochemical staining for IgG4 demonstrates >50 IgG4+ plasma cells per high-power field. D, Immunohistochemical staining for IgG demonstrates an IgG4:IgG ratio of >40%.

Question

What is the diagnosis?

Answer

Diagnosis: IgG4-related disease with pleural and pancreatic involvement

Discussion

IgG4-related disease is a fibroinflammatory condition that is characterized by dense lymphoplasmacytic infiltrate with abundant IgG4-positive plasma cells and fibrosis. It is now understood to be a multisystem disorder, but it was recognized as a systemic disease only in 2003 when extra-pancreatic manifestations were seen in patients with autoimmune pancreatitis. It is believed that 40% to 60% of cases of autoimmune pancreatitis represent a pancreatic manifestation of IgG4-related disease.

The underlying pathogenesis of IgG4-related disease remains incompletely understood.

It is widely believed that [IgG4](#) antibodies are not themselves pathogenic but represent a response to a separate primary process. There is some evidence that the disease may be autoimmune in nature with a number of recognized autoantibodies believed to be involved (eg, [annexin](#) A11, [laminin](#) 111, and galectin-3). Cluster of differentiation 4+ cytotoxic T cells are the most abundant cells found within affected tissues in IgG4-related disease; IL-1, transforming growth factor-beta, and [interferon gamma](#) are produced by this population of cells and may be responsible for the fibrosis that is such a prominent pathologic feature of IgG4-related disease.

IgG4-related disease can affect virtually any organ system, including biliary, [salivary gland](#), lungs, [thyroid](#), lymph nodes, breast, skin, [retroperitoneum](#), orbit, [peripheral nerves](#), and prostate. A single site or multiple sites may be involved by the disease. The more common presentations include [pancreatitis](#) (type 1 autoimmune), [sclerosing cholangitis](#), sclerosing sialadenitis (Mikulicz disease), [retroperitoneal fibrosis](#), and orbital disease. IgG4-related disease is mainly seen in men (70% to 80%), with a median age of 60 to 65 years at presentation. In Japan, the prevalence is 0.28 to 1.08 per 100,000 of the population, although, as understanding of the disease grows and recognition improves, this figure will likely increase.

Pulmonary manifestations of IgG4-related disease occur in approximately 14% of patients with IgG4-related disease. Intrathoracic disease may manifest with involvement of the [lung parenchyma](#), mediastinum, [pleura](#), lymph nodes, or airways. This may occur as part of a systemic IgG4-related disease, or it may occur in isolation. Pleural involvement in isolation is rare and generally manifests as pleural-based nodules. One half of patients with pulmonary IgG4-related disease will present with respiratory symptoms; the remaining patients are asymptomatic and diagnosed based on abnormal imaging alone.

The diagnosis of IgG4-related disease may be challenging because the lesions may be difficult to distinguish from [malignancy](#) or other chronic inflammatory conditions, based on imaging alone. Diagnosis relies on a multidisciplinary approach and on the availability of high-quality histologic sampling, which may be difficult to obtain for intrathoracic disease. Pathologic diagnostic criteria for IgG4-related disease stipulates that >40% of IgG-positive plasma cells must be IgG4-positive and that there must be >10 IgG4-positive cells per high-powered field of [biopsy sample](#).

Serum [IgG4](#) levels do not have the sensitivity or specificity to be used as a stand-alone test in the diagnosis of IgG4-related disease. It may be normal in 20% to 40% of those with the disease; 5% of people without the disease may have a positive result.

IgG4-related disease, given the fibrotic nature of the lesions, may result in [end organ damage](#); for that reason, the consensus is to initiate treatment for all symptomatic patients and to consider treatment in some asymptomatic patients. Some patients will undergo [spontaneous remission](#), but there is likely to be a high risk of relapse. The disease is sensitive to corticosteroids, although consideration must be given to the impact of long-term steroid use and the risk of relapse with their withdrawal. Second-line immunomodulatory treatments include [azathioprine](#), [methotrexate](#), [mycophenolate](#), [mercaptopurine](#), and [cyclophosphamide](#). [Rituximab](#) has been used in patients with refractory disease and in individuals who are intolerant of corticosteroids due to side-effects, and favorable results have been reported. Unfortunately, at this time, no long-term follow-up data are available on patients with IgG4-related disease, and no [randomized controlled trials](#) have been performed to date.

Clinical Course

Laboratory investigations were suggestive of a systemic inflammatory condition (elevated D-dimer, C-reactive protein, [alanine aminotransferase](#), aspartate aminotransferase and platelet count). Pleural fluid analysis was suggestive of an inflammatory or malignant condition (high [lactate dehydrogenase](#), elevated lymphocyte count), but it was felt that further pleural/lung tissue was needed to ascertain a definitive diagnosis. The patient underwent video-assisted thoracoscopic surgery with right-sided pleural and [lung biopsies](#). A talc [pleurodesis](#) was also performed. The surgical chest drain was removed on postoperative day 4. Consideration was given to a diagnosis of pancreatitis-associated [pleural effusion](#); however, serum [amylase](#) was elevated only modestly, and the patient did not complain of any abdominal pain or other [GI symptoms](#). There were no significant acute abnormalities demonstrated on [magnetic resonance cholangiopancreatography](#) (eg, no pancreaticopleural fistula). Given the history of autoimmune [pancreatitis](#) and raised serum levels of IgG4, specific staining of the pleural and lung biopsy for IgG and IgG4 was performed. A diagnosis of IgG4-related [systemic disease](#) with pleural and pancreatic involvement was made.

On review in the outpatient clinic 1 month later, the patient reported no dyspnea and no [chest pain](#). Follow-up [chest radiograph](#) showed near complete resolution of the right-sided [pleural effusion](#) ([Fig 4](#)).



1. [Download: Download high-res image \(276KB\)](#)
2. [Download: Download full-size image](#)

Figure 4. Chest radiograph at follow up. Posteroanterior chest radiograph after treatment shows almost complete resolution of the right pleural effusion.

Clinical Pearls

- 1.

Exudative, lymphocytic pleural effusion warrants further investigation with invasive pleural biopsy when the cause is not clear based on pleural fluid analysis alone.

- 2.

IgG4-related [pulmonary disease](#) is a rare entity; there is a strong association with autoimmune pancreatitis.

- 3.

Diagnosis of IgG4-related pulmonary disease requires a high degree of clinical suspicion and a multidisciplinary approach.

- 4.

Patients with IgG4-related pulmonary disease require ongoing follow up, given the risk of end-organ damage and high risk of relapse with withdrawal of corticosteroids.

Abstract

[Computed tomography](#) (CT) scanning is the gold standard when estimating [pleural effusion](#) volume; however, the procedure exposes patients to [ionizing radiation](#). Our study was aimed at developing ultrasound-based calculation models that can quantify the volume of [pleural effusion](#) in seated patients and validating each model using volumetric chest CT analyses as reference. Our study enrolled 36 hospitalized patients who underwent a chest CT scan and ultrasound, in the seated position, with the aid of a convex probe. To estimate the volume of pleural effusions, we applied one linear and two multiplanar ultrasound-based equations using a CT reconstruction as reference. Testing these models in our validation set ($n = 16$), we determined that 0.42 was the R^2 coefficient for the linear equation, and 0.97 and 0.98, respectively, were the R^2 coefficients for the cylindrical-sector models, and observed that the latter had the lowest dispersion of data and an optimal intraclass correlation coefficient. We then concluded that multiplanar ultrasound-based equations are accurate and reliable in estimating pleural effusions and outperform previously developed equations.

Introduction

Pleural effusion is a common finding in clinical practice and can be caused by several insults (Feller-Kopman and Light 2018). Assessment of the size of pleural effusions, especially transudative pleural effusions, may allow evaluation of the relationship between fluid accumulation and respiratory signs and symptoms (such as dyspnea, orthopnea and hypercarbia). Pleural drainage is not always required (Ferreiro et al. 2017) but repeated measurement is useful at follow-up and in monitoring (Bibby et al. 2018).

Recently, Walker et al. (2017) pointed out that in 46% of patients diagnosed with pleural effusion, there is a non-malignant etiology, and that transudative effusions are associated with a high mortality rate at 1 y.

Because pleural drainage is rarely required, quantifying the volume of fluid and the response to medical treatment over time becomes important to the clinician. It is especially useful in people affected by congestive heart failure, who account for the vast majority of transudative pleural effusion cases, to monitor and optimize their response to the therapy (Picano et al. 2018). In people with end-stage renal failure undergoing peritoneal dialysis (Bakirci et al. 2007) or in those with nephrotic syndrome (Light 2006), an overload of pulmonary fluid can have major

therapeutic and prognostic implications. For instance, the number of lung comets and the presence of pleural effusion are strong inverse correlates to left ventricular ejection fraction and selected indexes of a diastolic function (Miglioranza et al. 2013).

Finally, estimating the effused pleural fluid in oncological patients may help to optimize their palliation, minimizing unnecessary and invasive procedures (Neragi-Miandoab 2006).

Although a chest ultrasound may be well suited to spot pleural effusions, we still regard computed tomography (CT) as the more accurate tool to estimate the volume of pleural fluid in the chest (Moy et al. 2013). Chiao et al. (2015) recently reported that volumetric CT analyses equal or even surpass pleural tapping. Not always in fact, the pleural tap procedure succeeds in removing fluid completely, as proven by post-procedural CT (Chiao et al. 2015). Volumetric CT analyses can then be used to quantify pleural effusions accurately. However, this is time consuming and expensive and, mainly, exposes patients to additional radiation (Kearney et al. 2000; Genders et al. 2015).

For such reasons, many attempts have been made to measure the size of a pleural effusion by chest ultrasound. Several approaches have been proposed, but important issues are yet to be solved.

First, CT scans have never been used as a comparator, although they have been proven to be more precise (Vignon et al. 2005; Balik et al. 2006; Remérand et al. 2010); therefore, the results lack accuracy. Second, we know of one study providing predictive equations suitable for seated patients and directly comparing different calculation models (Hassan et al. 2017). However, the authors of this study applied equations developed for critically ill, decubent patients and even used the amount of drained pleural fluid as a reference, which might affect the reliability of the equation, particularly if applied to seated patients.

On these bases, we aimed to develop ultrasound-based calculation models to quantify pleural effusion in seated patients and validate each model using as our gold standard volumetric chest CT analyses.

Section snippets

Methods

Over a 4-mo period, we prospectively studied 36 patients (aged 45–88 y). Patients with documented pleural effusion were hospitalized at our pneumology outpatient clinic at the Campus Bio-Medico University Hospital. We identified and collected all underlying causes of effusion. We considered as eligible for CT and ultrasonographic assessment both unilateral and bilateral effusions. All patients underwent a chest CT scan (with or without contrast enhancement, as required) followed by a chest

Results

We enrolled 36 patients (mean age: 72 ± 12 , 55% males), 8 of whom (22%) presented with bilateral pleural effusion. Twelve patients were excluded on the basis of our exclusion criteria. In 9 cases, clinical presentation required for an immediate intervention (pleural drainage, diuretic treatment or electrical cardioversion), while 3 other patients refused to provide informed consent. No patients were excluded for poor ultrasound image acquisition.

The mean pleural fluid estimated by CT scan was

Discussion

To the best of our knowledge, no study has provided such a high correlation with the recognized gold standard. In fact, no multiplanar models have previously been tested to implement the diagnostic performance of chest ultrasound in pleural fluid detection and quantification. The accuracy of existing linear models is poor; therefore, results are highly variable. Using a linear model as control, we were able to confirm the superiority of a multiplanar approach over a linear approach (Table 4).

Conclusions

Our study compared three ultrasonographic volumetric measurements of pleural effusion using a 3-D CT scan reconstruction as a reference standard. We were able to validate two cylindrical models displaying an excellent degree of correlation with the gold standard and outperforming the currently available ultrasound-based equations.

Abstract

Aim

To compare the role of [chest US](#) and bedside plain [chest radiography](#) in the evaluation of intensive care patients having [pleural effusion](#) and [pneumothorax](#). Chest [computed tomography](#) has been used as an ideal standard.

Patients and methods

Sixty critically ill patients with chest troubles and positive CT, were be studied with chest US and bedside [CXR](#). Two pathologic abnormalities were be evaluated: [pneumothorax](#) and [pleural effusion](#). Each hemithorax had been examined for the existence or [absence](#) of each pathology. All patients had been assessed by clinical examination of chest, full clinical history, laboratory assessment. All patients who had pleural effusion underwent US guided FNAC.

Results

One hundred twenty hemithoraces had been investigated by the three [imaging techniques](#). The sensitivity, specificity and diagnostic accuracy of bedside CXR were 54.5, 96 and 83.3% for pneumothorax and 76.2, 70.6 and 75% for pleural effusion, respectively. The corresponding values for chest US were 85.7, 97.9 and 95.2% for pneumothorax and 100, 100, and 100% for pleural effusion, respectively.

Conclusions

In evaluation of ICU patients with pleural effusion and pneumothorax, chest US is the first bedside tool with high [diagnostic performance](#). These chest conditions are urgent especially in seriously ill patients, as both need US guided drainage. Chest US has many advantages, including non invasive examination in multiple planes, free of radiation hazard, less expensive, real-time, high sensitivity and diagnostic accuracy in chest lesions detection. Lung ultrasound is being exclusive than bedside chest X-ray and equal to chest CT in diagnosing pleural effusion and pneumothorax.

1. Introduction

Bedside plain [chest radiography](#) is routinely performed in the intensive care patients. Its limited [diagnostic performance](#) and efficacy have detected in multiple other studies [1]. Multiple

causes reported for the limited dependability of bedside chest radiography. First, the non stability of both patient and [thorax](#) caused the reduction in spatial resolution of the radiological image.

Second, the film cassette seated behind the thorax. Third, the X-ray beam originates anterior, at a shorter distance than recommended and quite often not tangentially to the diaphragmatic cupola, so masking the accurate interpretation of the [silhouette sign](#). Previous mentioned technical difficulties lead to wrong assessment of pleural effusion and pneumothorax [2]. Restrictions of bedside CXR have been well mentioned and lead to bad quality X-ray films with low sensitivity [3].

Chest [ultrasonography](#) is a brilliant apparatus in the ICU. It is better in multiple aspects than standard supine chest radiography, and its immediate availability allows the radiologists to rapidly evaluate the bedside patient with chest troubles [4]. Modern ultrasound tools are easily, available and portable, which makes them fit for bedside examination of the severely ill patient [5]. Chest US provides a dynamic assessment of the [pleural space](#), without radiation and so it considered safe. This is especially useful for repeating evaluations after therapeutic interventions. Additionally, compact and easily transportable devices have now made physicians themselves doing the exam and evaluate the scans in real-time to make bedside urgent clinical decisions [6].

We compared the diagnostic functioning of chest ultrasound and bedside CXR for the review of severely ill patients with pleural effusion and pneumothorax, using CT chest as an ideal standard [7].

2. Patients and methods

2.1. Methods

Comparative cross-sectional research had been done in the ICU (Medical and Surgical ICU) of Zagazig University Hospitals in the period between April 2016 and May 2017.

Approval from the hospital ethics committee and [informed consent](#) was obtained either from the patient himself or first degree relatives.

Inclusion criteria:

- 1.

Any age group and sex.

- 2.

ICU patients with chest troubles and previous positive CT.

Exclusion criteria:

- 1.

Seriously ill patients attached to multiple support devices drains and catheters that restrict the accurate placement of the probe.

- 2.

Pregnant women.

- 3.

Obese patients with bulky chest walls.

All patients assessed by the following:

(A) [Clinical evaluation](#):

- 1.

Complete [history taking](#) (from the patients or their relatives).

- *Dyspnea.
- *Chest pain.
- *Cough and fever.

- 2.

Clinical examination of chest

- *Vital signs: [Tachycardia](#), [tachypnea](#).
- *Local examination.

(B) Laboratory assessment

- *Elevated [C reactive protein](#).
- *Elevated Total Leukocyte Count.

(C) Chest radiography

Every patient underwent CXR examination before US. The antero-posterior view had been done by transportable X-ray equipment (Siemens). The assessment of CXR had been performed; pneumothorax and pleural effusion defined using the terms of the Classification Team of the Fleischner Society [\[8\]](#).

(D) Chest [ultrasonography](#)

Before performing the US examination, we review the previous patient's CT (positive for pneumothorax and pleural effusion).

US examinations have been done by YD-9000 A (China) and Fukuda denshi (UF-400AX) (Japan). The two ultrasound devices were with: fully digital [portable US](#) system, B-mode, M-mode and active convex and linear probes.

All patients had real-time gray-scale US with a 3.5–5 MHz and 5–8 MHz probes. M-mode (motion mode) was an excellent supporting imaging modality in all patients.

Each hemithorax divided into six regions bordered by the anterior and posterior [axillary lines](#), three in upper fields (anterior, posterior and lateral) and three in lower fields (anterior, posterior and lateral).

- (1)

The intercostal approach: The patient lies in [supine position](#). The probe places transversely between the ribs giving the maximum field of view without interruption of the ribs. This approach is excellent for imaging of the [pleura](#).

- (2)

The abdominal approach: Also in supine position, the [thorax](#) can be scanned with the liver and spleen exhibiting acoustic windows to the thorax.

- (3)

The suprasternal approach: Patients can be scanned in a supine posture with a cushion placed under the shoulders and neck extended. The probe placed at the root of the neck and angled caudally behind the [manubrium](#). The posterior chest is better imaged with patient sitting erect, while the anterior and lateral chest assessed in the lateral decubitus posture. Raising the patient's arm above his head increased the rib space distance and facilitated scanning when the patient was in recumbent position. Scanning had been done during calm respiration.

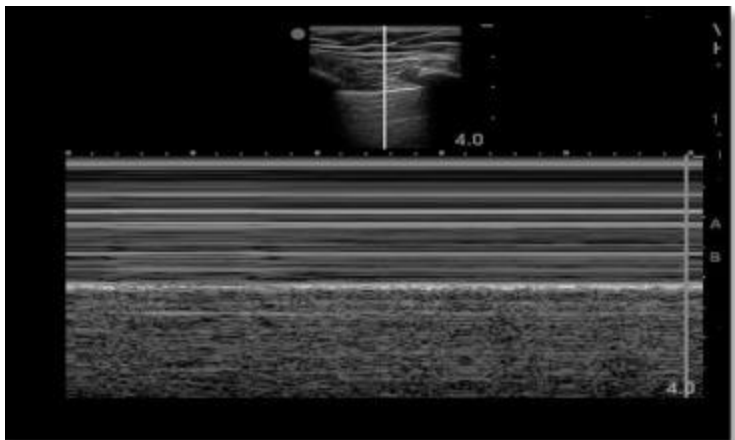
Normal chest US pattern:

*Normally the chest wall appears as sequences of echogenic soft tissue layers, denoting the layers of muscles and the [fascia](#) planes ([Fig. 1](#)) [9]. The ribs appear on transverse scans as curvilinear structures with posterior acoustic shadowing beneath the chest wall soft tissue. On longitudinal scans, the anterior cortex should come into view as an uninterrupted smooth echogenic line [10]. With a high resolution linear probe, the visceral and [parietal pleura](#) describes as two echogenic lines under the ribs [9]. A hyperechoic and sliding line, moving forward and backward with respiration, notes 0.5 cm underneath the rib line, and mentions as the "pleural line". In M-mode, a "seashore sign" is existing, characterized by motionless parietal tissue over the pleural line and a homogenous granular pattern below it [12] ([Fig. 2](#)).



1. [Download: Download high-res image \(55KB\)](#)
2. [Download: Download full-size image](#)

Fig. 1. Normal US form of the chest. Reverberation artifacts (*) and vertical comet tail artifacts (+) are seen [9].



1. [Download: Download high-res image \(133KB\)](#)
2. [Download: Download full-size image](#)

Fig. 2. Normal [chest US](#) and specific seashore sign by M-mode [\[11\]](#).

Normal US pattern describes lung sliding associated with artifactual horizontal A lines (repetition lines parallel to the pleural line). Vertical B-lines (one or more mobile vertically oriented lines that originate at the pleural interface) can notice in dependant lung regions and are devoid of any pathological importance. B-lines move with the pleural line and efface A-lines [\[12\]](#).

The diaphragm is best examined through the lower [intercostal spaces](#) and looks as an echogenic line, 1 mm thick, on top of the liver and spleen. Normal downward movement of the diaphragm should detect during inspiration [\[9\]](#).

3. Pleural effusion

The standard look of pleural effusion is an anechoic fluid in between the both layers of [pleura](#) [\[9\]](#). Four different forms recognize at US are anechoic, complex but non septated, complex and septated and echogenic [\[12\]](#). The nature of pleural effusion (transudate or exsudate) can't be exactly evaluated by US exam only [\[13\]](#). Transudates are almost anechoic. However, exudates may appear anechoic, complex, or echogenic. Mobile strands of echogenic tissue and septations are often detected in inflammatory effusions. Malignant effusions are more commonly anechoic than echogenic. However, a definite reporting of malignant effusion must do with both FNAC and nodular [pleural thickening](#) together [\[9\]](#).

On bedside US, the dorsal spine can't normally be visualized above the diaphragm because the air-filled lungs scatter the US waves. In pleural effusion, there is a sustained appearance of the [vertebral bodies](#) from the abdomen into the [thoracic cavity](#). In cases of variable pleural fluid [echogenicity](#), the "thoracic spine sign" can help the bedside radiologists in imaging the pleural fluid [\[14\]](#).

Easy quantification of pleural fluid in seriously ill patients may help to settle on doing [thoracocentesis](#) in high risk patients. The amount of pleural fluid volume can be calculated by the so easy formula: $V(\text{ml}) = 20 \times \text{Sep} (\text{mm})$ where V is the volume of pleural fluid, and Sep is the maximal distance between parietal and visceral pleura in end expiration ([Fig. 3](#)) [\[15\]](#).



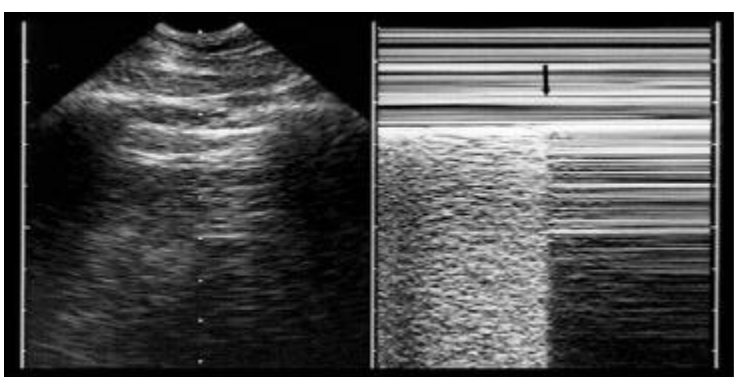
1. [Download: Download high-res image \(57KB\)](#)
2. [Download: Download full-size image](#)

Fig. 3. Sep measurement [15].

3.1. Pneumothorax

Pneumothorax describes by the existence of air between both layers of pleura [16]. The US diagnosis of pneumothorax is the most complicated part of training; long practice is a must to have excellent skills that rely on the facility to identify lung sliding and its abolition. Lung sliding is a normal find on healthy cases and identified during respiration easily. The use of higher emission frequencies (5–10 MHz) recognizes the lung sliding abolition. The identification of the partial pneumothorax is much complicated [12].

The sign of presence of air in the [pleural space](#) is the “Barcode sign” or “Stratosphere sign” on M-mode. The air will produce only the horizontal lines throughout the image. The patient should position accurately supine to allow locality of pleural gas effusion in non-dependant lung fields. To exactly detect the partial pneumothorax, examination should include the lateral regions of the chest wall to localize the point where the normal lung pattern (lung sliding) replaces the pneumothorax pattern (absent sliding and horizontal A-lines). This describes as the “Lung point” ([Fig. 4](#)) [17].



1. [Download: Download high-res image \(109KB\)](#)
2. [Download: Download full-size image](#)

Fig. 4. The lung point (the arrow) is an ideal sign of [pneumothorax](#) [17].

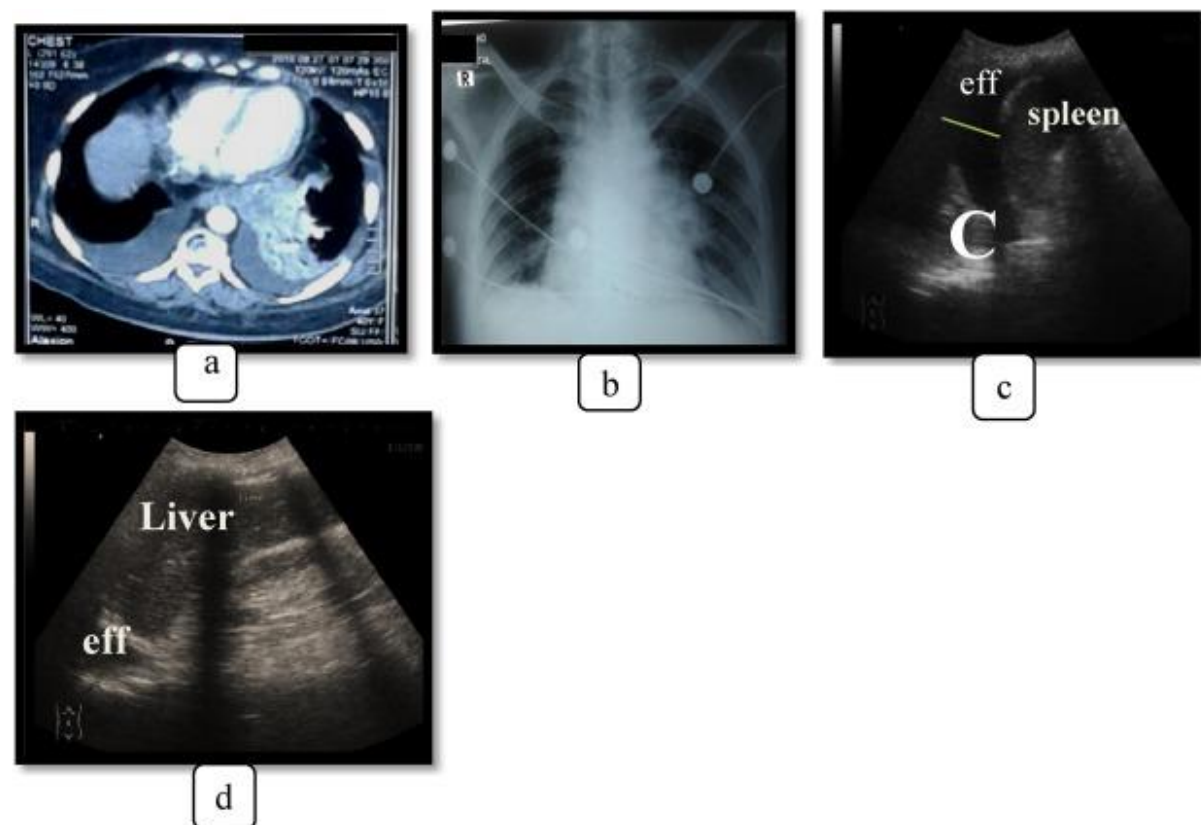
The propagation of cardiac systole on the pleural line calls “Lung pulse”. This lung pulse is lost in the pneumothorax, particularly on the left side [18]. Chest US detect pneumothorax within 2–4 min instead of twenty minutes to half an hour for CXR [12].

3.2. Result

Sixty ICU patients selected having CT positive for pleural effusion (48 patients) and pneumothorax (12 patients). [Patient characteristics](#) viewed in [Table 1](#). 120 hemithoraces (2 in each patient) diagnosed by three imaging tools ([Fig. 5](#), [Fig. 6](#), [Fig. 7](#)).

Table 1. [Patient characteristics](#).

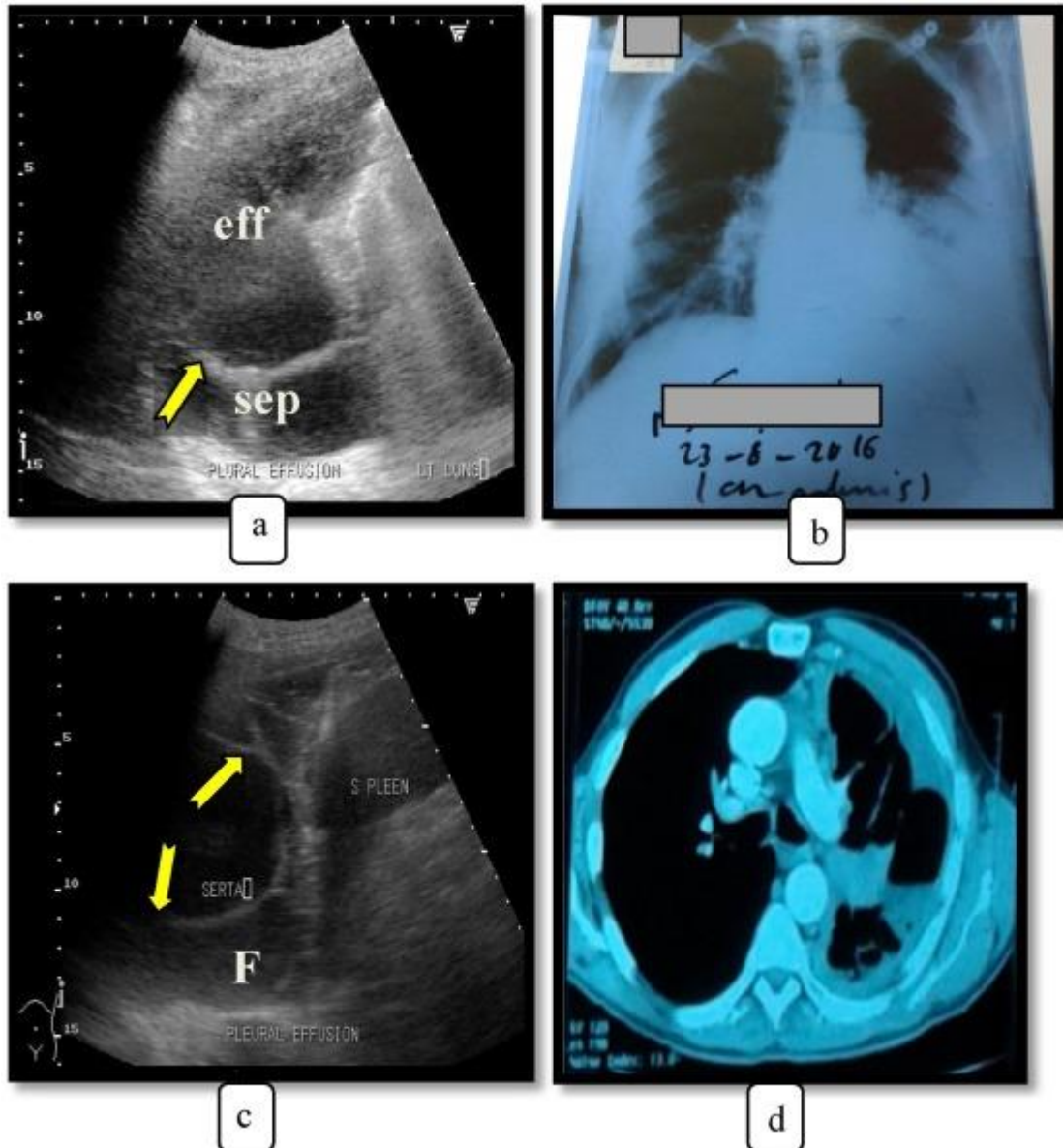
Age (Mean ± SD)	53.83 ± 14.63 years
Range	14–75 years
Sex male	38 (63.3%)
Female	22 (36.6%)



1. [Download: Download high-res image \(315KB\)](#)

2. [Download: Download full-size image](#)

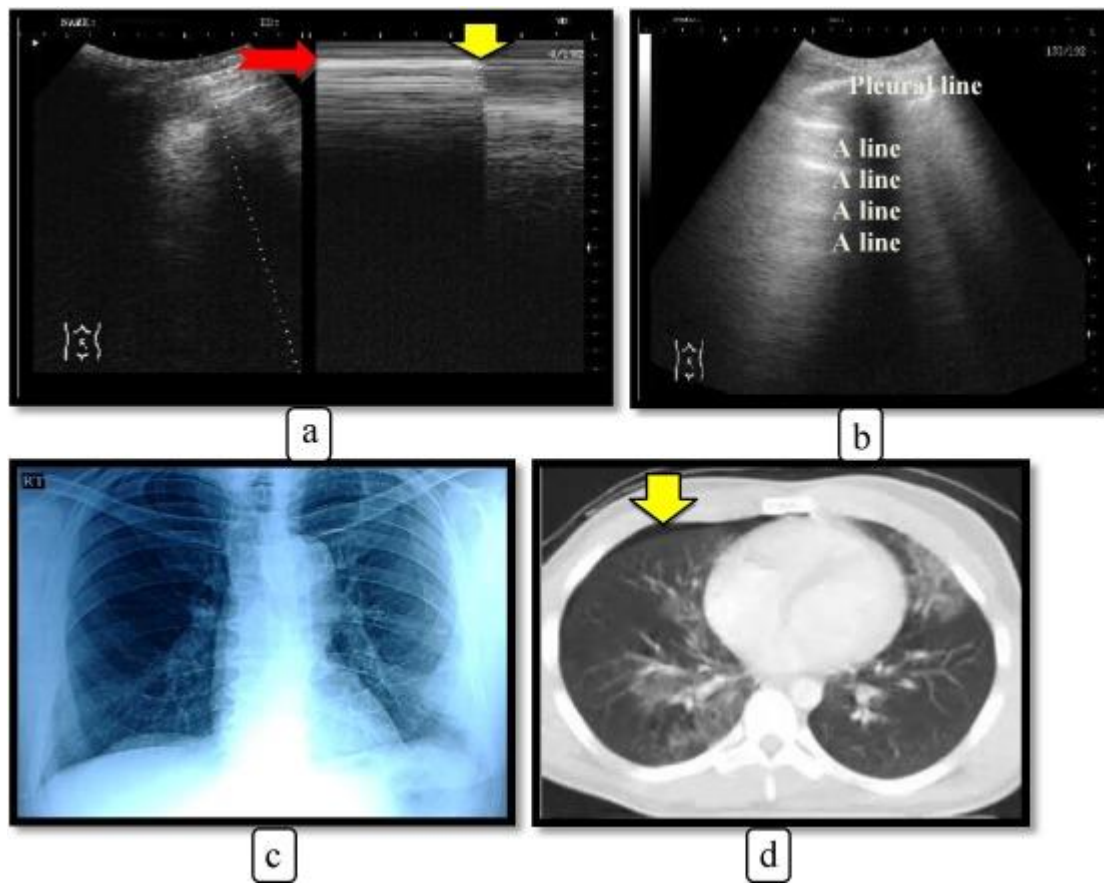
Fig. 5. ICU patient with CT reveals bilateral [pleural effusion](#) and LT. lower [lung collapse](#) (a). (b) [CXR](#) shows bilateral obliteration of costophrenic angles. (c) [Chest US](#) shows LT. effusion with Sep: 63 mm. Pleural fluid volume V (ml) = 20 × Sep (mm) V = 20 × 63 = 1260 ml. (d) Chest US shows RT. [pleural effusion](#).



1. [Download: Download high-res image \(546KB\)](#)

2. [Download: Download full-size image](#)

Fig. 6. ICU patient, chest US shows LT. multiloculated pleural effusion with multiple septations (arrows) and turbid fluid content (F) in (a & c). (b) CXR reveals obliteration of LT.costophrenic angle and heterogenous opacity rising to axilla. (d) Previously done CT positive for LT.pleural effusion.



1. [Download: Download high-res image \(450KB\)](#)

2. [Download: Download full-size image](#)

Fig. 7. (a) Lung US in seriously ill patient, M-mode, shows lung point (Yellow arrow) and pleural line (Red arrow). (b) Key sonographic signs in [pneumothorax](#): absent lung sliding, exaggerated A lines, loss of B lines, pleural line thickening. (c) CXR of the same patient in which both lung apices obscured (technical error) leading to miss the [pneumothorax](#). (d) Previous done CT shows small Rt.side pneumothorax (arrow). (For interpretation of the references to colour in this figure legend, the reader is referred to the web version of this article.)

[Table 2](#) showed the chest US full diagnostic criteria in pleural effusion. The pleural effusion's volume was moderate in 27 patients. Anechoic pleural effusion detected in 30 patients. FNAB had been done for all patients and [cytology](#) revealed exudate in 30 patients and [transudate](#) in 18 patients. Sensitivity, specificity, positive and negative predictive values and diagnostic accuracy of chest US and CXR for pneumothorax and pleural effusion exposed in [Table 3](#).

Table 2. Chest US findings in pleural effusion.

Pleural effusion	Empty Cell	Number (total 48)	Percent
Volume of pleural effusion	Mild (≤ 500 ml)	9	15%
	Moderate (500_1500 ml)	27	45%
	Massive (> 1500 ml)	12	20%

Pleural effusion	Empty Cell		Number (total 48)	Percent
Sonographic criteria of pleural effusion	Anechoic		30	50%
	Complex non septated		3	5%
	Complex septated		15	25%
Ultrasound guided aspiration (FNAB) (was done for all patients)	Type of aspirated fluid	Exudates: Malignant Inflammatory Transudates:	12 18 18	20% 30% 30%
	Its amount	10–20C.C	48	80%

Table 3. Sensitivity, specificity, positive, negative predictive values and diagnostic accuracy of chest US and CXR compared to CT scan (perfect standard) for each pathological entity.

Pathology	ChestUS/CXR	CT +	Sensitivity (%) ^a	Specificity (%) ^b	PPV (%) ^c	NPV (%) ^d	DA (%) ^e
Pneumothorax	ChestUS+	10	85.7%	97.9%	92.3%	96%	95.2%
	ChestUS-	2					
	CXR+	2	54.5%	96%	85.7%	82.8%	83.3%
	CXR-	10					
Pleural effusion	US+	48					
	US-	0	100%	100%	100%	100%	100%
	CXR+	33					
	CXR-	15	76.2%	70.6%	90.6%	44.4%	75%

TP true positive, TN true negative, FP false positive, FN [false negative](#).

a

Sensitivity = $[TP/(TP + FN)] \times 100$.

b

Specificity = $[TN / (TN + FP)] \times 100$.

c

+ve predictive value (PPV) = $[TP / (TP + FP)] \times 100$.

d

-ve predictive value (NPV) = $[TN / (TN + FN)] \times 100$.

e

Diagnostic accuracy (DA) = $[(TP + TN) / (TP + TN + FP + FN)] \times 100$.

In general, chest ultrasound was superior to bedside CXR, exhibiting significantly higher sensitivity, positive, negative predictive values and diagnostic accuracy.

There were twelve cases of pneumothorax and lung ultrasound identified ten of them, whereas one test was false positive. The two pneumothoraces can't be detected by chest ultrasound were small, apical location and did not need any interference. In the case of false positive result the pneumothorax detected small in size. Analysis of the false positive case revealed that occurred in subcutaneous emphysema as a result of traumatic chest insult.

3.3. Discussion

The final result of our work is the standard application of chest US for pleural assessment in the severely ill patients. This is allowing earlier detailed examination in addition to more perfect description of pleural disease than CXR [19].

4. Pleural effusion

Chest US has been done for identification of pleural effusions having sensitivity above 90% [20]. In our study, US revealed the existence of pleural effusion in 48 patients (80%), mild (≤ 500) in 9 patients, moderate (500 to 1500 ml) in 27 patients, massive (> 1500 ml) in 12 patients. We characterized pleural effusion according to its internal echoic pattern as 1.anechoic (30 cases, 50%), 2.complex non septated (3 cases, 5%) and 3.complex septated (15 cases, 25%). Our results were similar to Rizk et al. [21] study results which included 30 ICU patients and revealed pleural effusion in 66.6% of patients (anechoic in 50%, complex non septated in 6.66% and complex septated in 10%).

In our work, we did FNAB for all patients. Cytology results revealed exudative effusion in 30 cases (62.5%) and transudative effusion in 18 cases (37.5%), this agree with Kalkanis et al. [22] who showed that exudative effusion was 80% and transudative effusion was 20% in the patients with pleural effusion.

Agreement with Xirouchaki et al. [7] study results which included 42 ICU patients and stated that the sensitivity and specificity for lug US were 100% in diagnosis of pleural effusion, our results demonstrated that sensitivity, specificity and accuracy of chest US in the diagnosis of pleural effusion were 100%.

CXR performed very badly (sensitivity 76.2%, diagnostic accuracy 75%) representing the ineffectiveness assessment of pleural effusion.

5. Pneumothorax

The bedside assessment of pneumothorax is urgent in ICU patients. From our experience in this work, supine CXR is very poor in pneumothorax detection [23].

In our work bedside supine CXR can't detect ten of the twelve pneumothoraces. CXR was not capable of picking all partial pneumothoraces while chest US diagnosed them by imaging the lung point.

CXR had sensitivity and specificity of 54.5% and 96% respectively.

Chest US in our work identified ten out of the twelve cases. However, both pneumothoraces missed by US were tiny and none needed drainage, a result similar to Brook et al. [24] in the [emergency department](#). The only one case with false positive result detected in [subcutaneous emphysema](#) in traumatic chest insult patient. Our findings were in harmony with Zhang et al. [25] who revealed that US findings in pneumothorax were lung point sign, multiple horizontal artifacts (A lines), absent lung sliding.

In our current study, sensitivity of chest US was 85.7%, specificity was 97.9% and accuracy was 95.2%, this matching with Zhang et al. [25] results which demonstrated that lung US revealed sensitivity, specificity and diagnostic accuracy of 86.2%, 97.2% and 94% respectively. Also, our results typically matched with that of Soldati et al. [22].

However, lung US did not miss any clinically significant pneumothorax, our study stated that this examination is a consistent tool for bedside urgent assessment of this pleural pathology.

6. Restrictions of chest us

Our work has some limits. **Firstly**, a relatively little number of patients ($n = 60$) studied. However, the fact that the lung US was evaluated separately on each hemithorax, increased the cases (from 60 to 120), partly overcoming this limitation. **Secondly**, the only choice principle we used for including in our study was the previous positive CT chest scan with iodine [contrast material](#). Thus, the cases studied were pre-selected as having pleural effusion or pneumothorax. **Thirdly**, the subcutaneous emphysema hinders the transmission of US beams to the lung periphery. This cause of the only false positive result in pneumothorax cases by US examination.

7. Conclusion

Pleural effusion and pneumothorax are two chest urgent conditions especially in the ICU patients, as both requires US guided drainage. Chest US offers a noninvasive first diagnostic mean at the bedside for evaluation of ICU patients. It has many advantages, including examination in multiple planes, free of radiation hazard, less expensive, real-time and high sensitivity in chest lesion detection. Lung ultrasound has confirmed to be exclusive than the bedside CXR and equivalent to chest CT in evaluating pleural effusion and pneumothorax.

Methods

A secondary analysis of a pneumonia database was conducted to identify patients who received a CCT within 24 hours of presentation and also received AP or PA/Lat [chest radiographs](#) within 24 hours [of CCT](#). Sensitivity and specificity were then calculated by comparing the radiographic diagnosis of [PPEs](#) of both types of radiographs compared with CCT by using the existing attending radiologist interpretation. Clinical relevance of effusions was determined by CCT effusion measurement of >2.5 cm or presence of loculation.

Results

There was a statistically significant difference between the sensitivity of AP (67.3%) and PA/Lat (83.9%) chest radiography for the initial detection of CR-PPE. Of 16 CR-PPEs initially missed by AP radiography, 7 either required drainage initially or developed [empyema](#) within 30 days, whereas no complicated PPE or [empyema](#) was found in those missed by PA/Lat radiography.

Conclusions

PA/Lat chest radiography should be the initial imaging of choice in pneumonia patients for detection of PPEs because it appears to be statistically superior to AP chest radiography.

Introduction

Approximately 1 million patients each year are hospitalized with community-acquired pneumonia (CAP) [1]. Of these patients, 45% will develop a parapneumonic effusion (PPE), which confers an increased morbidity and mortality if it progresses to an empyema [2], [3], [4], [5]. This makes the timely identification of PPE paramount in the evaluation of patients with CAP.

Both anteroposterior (AP) and posteroanterior with lateral chest (PA/Lat) radiographs are used in emergency departments (EDs) to diagnose CAP. If PPE is detected by these studies, additional tests such as lateral decubitus radiography, chest computer tomography (CCT), or chest ultrasonography (US) are then used to determine the need for thoracentesis and analysis of the PPE. If no effusion is initially detected, then further radiographic studies are not routinely pursued. Anterior chest radiographs can detect effusion volumes between 175 and 200 mL but have poor sensitivity for smaller effusions [6], [7]. In contrast, the addition of lateral erect radiography allows detection of PPE <175 mL [6], [7]. Despite suspected superiority of PA/Lat over AP chest radiography due to its lateral view, a recent article suggested that when compared with a reference standard of CCT, both AP and PA/Lat radiographic studies missed a significant proportion of PPEs, and neither had clear superiority [8].

We have previously established that clinically relevant PPEs (CR-PPEs) requiring thoracentesis are those with either loculations or measurements ≥ 2.5 cm on CCT [9]. Although other studies have used CCT as a reference standard by which to evaluate the sensitivity of chest radiographs in the diagnosis of pleural effusions, whether CR-PPE or inconsequential PPE [7], [8], [10] our measurement system allows an accurate comparison of AP and PA/Lat radiography for detecting CR-PPEs. Our objective was to determine if, during the initial evaluation of CAP, PA/Lat chest radiography is superior to AP chest radiography for the detection of CR-PPE and thus to rapidly and efficiently guide further diagnostic testing such as US, CCT, or lateral decubitus radiography.

Study design

This was a secondary data analysis of pneumonia patients enrolled in the Community-Acquired Pneumonia Organization (CAPO) international cohort study from January 2003 through March 2009 at the Robley Rex Veterans Administration Medical Center (VAMC) of Louisville, KY. Only CAPO patients enrolled from our VAMC were reviewed because of limitations in film availability of the larger international database. The VAMC Institutional Review Board approved this study under CAPO 350.01.

Study definitions

CAP was defined as

Patient characteristics

Our database reported 859 study subjects with CAP with an average age of 69.9 ± 11.7 years, of which 98.3% were male. Radiographic characteristics and other admission demographics are presented in Table 1. Of these patients, 43.1% underwent a CCT during their hospitalization, and 28.8% received a CCT within 24 hours of presentation (Fig. 1). Of those, 160 also received interpretable AP chest radiography and 115 received interpretable PA/Lat chest radiography; 96.9% of initial AP chest

Discussion

Despite the theoretical superiority of PA/Lat chest radiography in allowing rapid diagnosis of even minute pleural effusions due to its lateral view, a recent article has suggested that AP and PA/Lat chest radiography may be equally efficacious in the ED evaluation of CAP to exclude PPE [8]. In our population, 96.9% of patients in this study received an initial ED AP radiograph, with 84.3% of PA/Lat chest radiography being ordered after admission. This suggests that determination of the initial

Aims

This study aims to compare the 'drainage time': the time required to drain the effusion, with a small-bore (12F) chest tube or a conventional large-bore (20–24F) chest tube in patients with a parapneumonic effusion.

Methods

Data from 54 patients with parapneumonic effusions who had chest tubes inserted were collected retrospectively and analysed in a tertiary UK hospital.

Results

The drainage time was significantly less ($p<0.01$) with a large-bore chest tube (3.87 days) compared with a small-bore chest tube (5.3 days). Analysis also showed that the large-bore group had more complex parapneumonic effusions than the small-bore group, with higher [lactate dehydrogenase](#) (LDH) levels (9,043 versus 1,968 IU/L respectively) and lower glucose levels (3.37 versus 5.13 mmol/L respectively) (Table 1). There was no significant difference in mortality ($p=0.54$) or surgical referral rate ($p=0.68$) between the two groups.

Table 1. Summary of the [patient characteristics](#) and outcomes between the groups with two different-sized chest tubes

Patient characteristic	Total	Small-bore tube	Large-bore tube
Number (%)	54	36 (66.7)	18 (33.3)
Median age (years)	67.0	69.0	63.5
Gender:			

Patient characteristic	Total	Small-bore tube	Large-bore tube
Men (%)	48 (88.9)	35 (97.2)	13 (72.2)
Women (%)	6 (11.1)	1 (2.8)	5 (27.8)
Location:			
Inpatient (%)	48	32 (88.9)	16 (88.9)
Outpatient (%)	6	4 (11.1)	2 (11.1)
Biochemistry profile:			
Average fluid LDH (IU/L)	N/A	1,963	9,048
Average fluid glucose (mmol/L)	N/A	5.13	3.37
Outcome:			
Did not require further intervention (%)	44	29 (80.6)	15 (83.3)
Drainage time (mean±SD, days)	N/A	5.3±0.22	3.8±0.40
Surgical referral (%)	7	4 (11.1)	3 (16.7)
Died (%)	3	3 (8.3)	0 (0)

LDH = lactate dehydrogenase; N/A = not applicable; SD = standard deviation

Conclusions

Drainage time with a large-bore chest tube was significantly less than with a small-bore chest tube, despite the large-bore group having patients with more complex parapneumonic effusions. We recommend the use of a large-bore chest tube as the initial choice of chest tube size for the management of a patient with parapneumonic effusion.

Background

Both elevated pleural elastance ($E-P_{EL}$) and radiographic evidence of incomplete lung expansion following [thoracentesis](#) have been used to exclude patients with a [malignant pleural effusion](#) (MPE) from undergoing [pleurodesis](#). This article reports on a cohort of patients with MPE in whom complete drainage was attempted with pleural [manometry](#) to determine the frequency of $E-P_{EL}$ and its relation with postthoracentesis radiographic findings.

Methods

Seventy consecutive patients with MPE who underwent therapeutic pleural drainage with pleural [manometry](#) were identified. The pressure/volume curves were constructed and analyzed to determine the frequency of E-P_{EL} and the relation of P_{EL} to the postthoracentesis chest radiographic findings.

Results

E-P_{EL} and incomplete lung expansion were identified in 36 of 70 (51.4%) and 38 of 70 (54%) patients, respectively. Patients with normal P_{EL} had an OR of 6.3 of having complete lung expansion compared with those with E-P_{EL} ($P = .0006$). However, 20 of 70 (29%) patients exhibited discordance between postprocedural chest radiographic findings and the pleural manometry results. Among patients who achieved complete lung expansion on the postdrainage [chest radiograph](#), 9 of 32 (28%) had an E-P_{EL}. In addition, P_{EL} was normal in 11 of 38 (34%) patients who had incomplete lung expansion as detected according to the postthoracentesis [chest radiograph](#).

Conclusions

E-P_{EL} and incomplete lung expansion postthoracentesis are frequently observed in patients with MPE. Nearly one-third of the cohort exhibited discordance between the postprocedural chest radiographic findings and pleural manometry results. These findings suggest that a prospective randomized trial should be performed to compare both modalities (chest radiograph and pleural manometry) in predicting [pleurodesis](#) outcome

Materials and Methods

We retrospectively reviewed consecutive patients with a diagnosis of MPE based on positive pleural cytology findings who underwent an attempt at complete pleural drainage and had concomitant pleural manometry. A postthoracentesis anteroposterior view CXR was obtained immediately following thoracentesis. Each postprocedural CXR was reviewed independently by a dedicated thoracic radiologist. Postprocedural CXRs were evaluated for: (1) complete lung expansion (CLE-CXR), which was defined as >

Results

Seventy consecutive patients who had undergone therapeutic thoracentesis and concomitant pleural manometry were identified. Table 1 presents the demographic and tumor characteristics of the study cohort. Fifty-seven of 70 (81.4%) patients had an adenocarcinoma. A non-lung primary tumor was detected in 51 of 70 (72.8%) patients. The 70 patients who had undergone therapeutic thoracentesis and concomitant pleural manometry constituted the cohort that was analyzed. Selection of patients undergoing

Discussion

In this analysis of 70 patients with MPE who underwent pleural drainage with pleural manometry, the postthoracentesis CXR findings and pleural manometry each identified a contraindication to pleurodesis in approximately 50% of the cohort.

The prevalence of ILE-CXR was 54% in this study cohort and was higher than reported in previous studies (range, 2%-30%).^{8, 9, 10} The degree of variability in ILE-CXR across various series may be due to heterogeneity in the accepted degree of pleural apposition

Conclusions

The present investigation suggests that 50% of patients with MPE have an abnormality in lung expansion as detected according to pleural manometry and CXRs. Incomplete lung expansion on postthoracentesis CXR and E-P_{EL} are both considered as a contraindication to pleurodesis. However, we found significant discordance between these two criteria. These results suggest that pleural manometry may have a role in addition to the postthoracentesis CXR in selecting patients for pleurodesis;